Substructure and Gas Clumping in the Outskirts of Abell 133

by

Gandhali Joshi

A thesis
presented to the University of Waterloo
in fulfillment of the
thesis requirement for the degree of
Master of Science
in
Physics

Waterloo, Ontario, Canada, 2013

I hereby declare that I am the sole author of this thesis. This is a true copy of the thesis, including any required final revisions, as accepted by my examiners.

I understand that my thesis may be made electronically available to the public.

Abstract

Galaxy clusters are powerful tools for studying various astrophysical principles. Gas accreting onto the cluster is heated to $10^7 - 10^8$ K through adiabatic compression and shocks, making clusters highly luminous in X-ray imaging. Measurements of the gas density and temperature profiles can be used to calculate the gas mass fraction f_{gas}, which is expected to closely match the cosmic baryon fraction Ω_b/Ω_m. Recent observations have found entropy profiles in cluster outskirts that are shallower than predicted and values of f_{gas} that are higher than the Universal baryon fraction inferred from the Cosmic Microwave Background (CMB). Abell 133 was an ideal candidate for studying this phenomenon, since it had recently been observed in a wide ($R \approx 30'$) Chandra mosaic with an exposure time of ~ 2 Ms. The X-ray imaging was combined with existing optical imaging from the *Canada-France-Hawaii Telescope* (CFHT) and spectroscopy obtained from the *Magellan* telescope, to search for any possible gas clumps and to study their properties.

The photometric analysis yielded over 3200 red sequence galaxies to a depth of r'= 22.5, which were used to create a Gaussian smoothed intensity map and a significance map of the cluster (compared to CFHT Legacy Survey data). About 6 significant overdensities were detected in the significance map, although these did not fully correspond to contours obtained from the X-ray image. Spectroscopy obtained on the cluster yielded ~ 700 secure redshifts, of which about 180 were cluster members. This included data from the NOAO Fundamental Plane Survey (NFPS) and the 6 Degree Field Galaxy Survey (6dFGS). We found a cluster redshift of $z = 0.0561 \pm 0.0002$ and a velocity dispersion of $\sigma = 743 \pm 43$ km/s. The dynamical analysis gave a virial radius of $r_v = 1.44 \pm 0.03$ Mpc and a virial mass of $M_v = (5.9 \pm 0.8) \times 10^{14} M_\odot$. We also found values of $R_{500} = 1.21 \pm 0.07$ Mpc and $M_{500} = (5.3 \pm 0.9) \times 10^{14} M_\odot$ for $\gamma = 1/3$ and $R_{500} = 0.99 \pm 0.05$ Mpc and $M_{500} = (2.9 \pm 0.5) \times 10^{14} M_\odot$ for $\gamma = 1/2$, where γ is a parameter related to the assumed density profile and the velocity anisotropy.

About 30 overdensities with a radius $R_c \geq 30$" were detected as gas clumps on the X-ray image. The galaxy distribution in these clumps was analyzed, both for the stacked signal as well as the individual clumps, in ten parallel colour-magnitude bands to find any significant red sequences associated with them. Most of these clumps appeared to be background systems, some consisting of 1-2 galaxies, others being small groups or clusters. Only 2-3 clumps appeared to be associated with the cluster itself. This suggests that the cluster density profile is actually quite smooth, which may not agree with recent numerical simulations. Further studies are required to determine if the cluster density distribution is consistent with what is predicted and the nature of the background systems.

Acknowledgements

Table of Contents

List of Tables

List of Figures

Chapter 1

Introduction

Galaxy clusters are some of the most powerful tools available to us for studying a wide variety of astrophysical phenomena. They are the most massive, collapsed, virialized objects and they represent the highest peaks of density fluctuations in the Universe. Clusters can have masses ranging from $10^{14} - 10^{15} M_\odot$ and this mass has three main components - cold dark matter (CDM) that makes up $\sim 80\%$ of the total mass of the cluster, stellar matter due to 10's-1000's of galaxies and the intra-cluster medium (ICM) which is the hot diffuse gas dispersed between the galaxies. The latter two make up the baryonic mass in the cluster, although the hot gas is the more dominant component, containing $\sim 80\%$ on average of the baryonic mass of the cluster [e.g. Ettori et al., 2004]. Recent work by Andreon [2010] did find that the stellar and gas fractions of the baryonic mass depend on the cluster mass itself - lower mass clusters tend to have a higher stellar mass fraction and a lower gas mass fraction. Also, some studies have shown that the intracluster light (ICL), coming from stars within the cluster not belonging to any specific galaxy, is an important component of clusters, more prominently in the outer regions and especially in lower mass systems [Gonzalez et al., 2005, 2007, Lin and Mohr, 2004].

One of the most important models for the density profile of dark matter halos surrounding clusters is the Navarro-Frenk-White (NFW) profile, which was found using high-resolution N-body simulations of dark matter halos [Navarro et al., 1997]. They found that the density profile was universal, irrespective of halo mass, initial density fluctuations and cosmological parameters. The density profile is described by

$$\rho(r) = \frac{\rho_s}{(r/r_s)\left[1 + r/r_s\right]^2} \tag{1.1}$$

Measurements of the density profiles however cannot usually directly probe the dark matter

distribution (except for those based on lensing); we rely instead on observations of the stellar matter or the ICM, and other indirect methods. Therefore, it is important to know if the stellar and gas profiles can be used to accurately measure the dark matter distribution. Comparisons between the distribution of the three components can also give information about galaxy formation. Numerical simulations of clusters can shed light on the properties of dark matter, ICM gas and galaxies in the cluster. Nagai and Kravtsov [2005] have carried out simulations of clusters and galaxy-sized subhalos and studied the NFW fits to the distribution of dark matter and galaxies. They found that the galaxy distribution is much more extended than that of the dark matter.

A key issue that is the subject of several studies is the cool core of clusters. The cores of some clusters are very luminous in X-ray radiation due to the high density, low entropy, ICM gas near the core. They can radiate away enough energy to cool 10s-1000s$M_\odot$ worth of X-ray emitting gas per year [Fabian et al., 1994]. This gas should then result in massive cooling flows as hotter gas from the outer regions moves towards the core. However, the amount of cooling rates predicted by the X-ray observations are much higher than the actual cooling rates observed through the strength of emission lines. This is known as the *classical cooling flow problem* [Fabian et al., 1991]. Ongoing studies are searching for solutions to the problem such as thermal conduction from the gas at outer radii, although this may not sufficiently account for the cooling flows [Parrish et al., 2009]. Currently, the most probably explanation is heating due to Active Galactic Nuclei (AGN) [e.g. McNamara and Nulsen, 2012].

Observations of clusters are useful for studying several, very different fields in astrophysics. Gas accreted onto clusters is heated to extremely high temperatures of $10^7 - 10^8$ K through adiabatic compression and shocks. This gas is therefore fully ionized, which can be useful in high energy physics research. Due to the scale of their masses, clusters are important for testing several fundamental principles of General Relativity or alternative theories of gravitation [e.g. Daniel et al., 2010, Rapetti et al., 2010]. Also, since their masses represent extremely deep potential wells, clusters retain virtually all the material they are formed with and hence, can trace different aspects of the evolution of the Universe. Clusters, by definition, contain large populations of galaxies which vary widely in mass, size, morphology, age and composition. Therefore, observations of clusters at different redshifts can give us information about the evolution of galaxies and the properties of the ICM. The clusters' own mass and density profiles can be used to test models of structure formation.

One major field where clusters are crucial is cosmology. Observations have shown that $\sim 70\%$ of the energy density of the Universe consists of dark energy [e.g. Perlmutter et al., 1998, Riess et al., 1998, Komatsu et al., 2011]. The simplest model for dark energy that is strongly supported by observations is the ΛCDM cosmology, which contains a cosmologi-

cal constant Λ described by an equation of state parameter $w = P/\rho c^2 = -1$. However, current data do not rule out other models such as a form of dark energy with $w \neq -1$ or one with w evolving with redshift. Galaxy clusters provide an important test of these dark energy models and are tools for constraining cosmological parameters [e.g. Vikhlinin et al., 2009b, Mantz et al., 2010a, Rozo et al., 2010, Sehgal et al., 2010, Vanderlinde et al., 2010]. The cluster mass function is sensitive to cosmology and the growth of large scale structure. Therefore, cluster abundances provide constraints on a combination of cosmological parameters different from those constrained by distance-redshift relation based tests [e.g. White et al., 1993, Eke et al., 1996, Wang and Steinhardt, 1998, Haiman et al., 2001, Holder et al., 2001, Battye and Weller, 2003, Wang et al., 2004]. Another cosmological test is measuring the fraction of the cluster mass that is baryonic, since the mass content in clusters is very similar to the Universal value [e.g. Kravtsov et al., 2005, Vikhlinin et al., 2006, Allen et al., 2008].

Most observations of clusters come from this baryonic mass and hence, various techniques have to be developed to estimate the total mass of these clusters from the observed properties. Clusters are observed using a variety of techniques, the most important of which are X-ray and optical imaging, detection through the Sunyaev-Zel'dovich (SZ) effect and gravitational lensing [Voit, 2005]. X-ray and SZ observations trace the thermal state of the cluster gas and can be used as indirect proxies for total mass through various scaling laws or through direct models based on the assumption of hydrostatic equilibrium. Gravitational lensing provides a direct measure of the total mass of the cluster, while optical imaging gives the properties of the stellar component and galaxy dynamics which can be used to obtain estimates for the dynamical mass.

Recent advances in X-ray imaging have enabled us to measure gas density and temperature profiles out to much larger radii than before. These have provided new estimates of the gas mass fraction in certain clusters that are larger than the universal value, as well as gas entropy profiles that are flatter than predicted [e.g. Simionescu et al., 2011, Urban et al., 2011, Walker et al., 2012a, Bonamente et al., 2013, Ichikawa et al., 2013]. A potential reason for this is gas clumping in the outskirts of the clusters, beyond their virial radius, resulting in higher gas density measurements in these regions. On the other hand, there are several results regarding the 'missing baryon' problem, where the gas mass fraction in galaxies and clusters is much lower than the baryon fraction measured from the CMB, although the effect is less severe in clusters and mostly solved by the inclusion of the stellar mass [e.g. Ettori, 2003, Afshordi et al., 2007, McGaugh et al., 2010, Shull et al., 2012].

This project studies the outskirts of the Abell 133 cluster, examining optical data and comparing it with X-ray imaging. The preliminary analysis is done using the cluster red sequence in two filters; the results are then used to target galaxies for further spectroscopy

3

and obtain redshifts for them. The clumps identified in the X-ray images were then characterized in terms of the significance of their galaxy counts and any dominant red sequences associated with them. It is found that several clumps did have associated red sequences and most of these appear to be background systems. Thus, it is likely that the actual density profile of Abell 133 is quite smooth, though this may be inconsistent with recent numerical simulations and other results.

1.1 Theory

1.1.1 FRW cosmology

The expansion of the Universe is evident from the redshift, $z = (\lambda_{observed} - \lambda_{emitted})/\lambda_{emitted}$, of the light coming from distant objects. The expansion for a spacetime described by the FRW metric is expressed as the evolution of a scale factor a by the Einstein Field Equations (EFE). For an ideal fluid, they produce the following two equations [Mo et al., 2010].

$$\frac{\ddot{a}}{a} = -\frac{4\pi G}{3}\left(\rho + 3\frac{P}{c^2}\right) \tag{1.2}$$

$$\left(\frac{\dot{a}}{a}\right)^2 = \frac{8\pi G}{3}\rho - \frac{Kc^2}{a^2} \tag{1.3}$$

Here, ρ is the fluid density and P its pressure. $K = -1, 0, 1$ for an open, flat and closed universe respectively. The scale factor is related to redshift as $a = a_0/(1 + z)$. The radial velocity of the object, $v \approx cz$ in the nearby Universe, is proportional to its distance D, i.e. $v = H_0 D$ where $H = \frac{\dot{a}}{a}$ is the Hubble parameter (H_0 is its value at the current time). The Hubble parameter describes the rate of expansion of the Universe and is determined by various cosmological parameters. To fully determine the time evolution of a, ρ and P, two more relations are required, the continuity equation,

$$\dot{\rho} = 3\frac{\dot{a}}{a}\left(\rho + \frac{P}{c^2}\right) \tag{1.4}$$

and an equation of state parameter $w = P/\rho c^2$. The ΛCDM universe is composed of matter (baryonic and dark matter), radiation, and a cosmological constant or vacuum energy; the standard ΛCDM cosmology refers to the additional condition of flatness. The energy density in each component evolves differently, based on the value of w, which is 0 for matter, 1/3 for radiation and -1 for Λ. Each component has a corresponding density

parameter Ω, as well as one to describe the curvature of spacetime, Ω_k. These parameters give the ratio of the density of each component to ρ_c, the critical density required for a flat universe, i.e

$$\Omega_i(z) = \frac{\rho_i(z)}{\rho_c(z)} \qquad \rho_c(z) = \frac{3H^2(z)}{8\pi G} \tag{1.5}$$

Distance-redshift relations

The Hubble parameter evolves as follows [Mo et al., 2010].

$$H^2(z) = H_0^2 \left[\Omega_{r,0} \left(1+z\right)^4 + \Omega_{m,0} \left(1+z\right)^3 + \Omega_{\Lambda,0} + \Omega_{k,0} \left(1+z\right)^2 \right] \tag{1.6}$$

Ω_m can be further subdivided into Ω_c and Ω_b for CDM and baryonic matter respectively. In clusters, the baryonic matter itself is dominated by the gas content of the cluster while the stellar matter in galaxies represents a small fraction. Constraints on these parameters can be obtained through calibrating distance-redshift relations, either based on luminosity distances D_L requiring standard candles such as SNe Ia, or angular diameter distances D_A requiring standard rulers such as strong and weak lensing observations, the scale of fluctuations in the CMB and the characteristic length scale of Baryonic Acoustic Oscillations (BAO).

$$D_A = \frac{1}{1+z} \int_0^z \frac{c}{H(z')} dz' \qquad D_L = (1+z) \int_0^z \frac{c}{H(z')} dz' \tag{1.7}$$

Large scale structure

Structure formation is the result of small density fluctuations in the background density $\delta = (\rho - \rho_b)/\rho_b$ of the primordial Universe that grow with its expansion. If these fluctuations are transformed into Fourier space with the amplitude of each mode δ_k sampled from a Gaussian distribution, they are described by a power spectrum $P(k) = \langle |\delta_k|^2 \rangle$ (note that the Gaussian distribution is an assumption made here). The scale of these fluctuations is measured in terms of the variance of this linearly evolving density field as follows [Mantz et al., 2010b].

$$\sigma^2(M, z) = \frac{1}{2\pi^2} \int_0^\infty k^2 P(k, z) |W_M(k)^2| dk \tag{1.8}$$

Here $W_M(z)$ is the Fourier transform of a filtering function, such as the spherical top-hat function [Mo et al., 2010]. Tests of cosmology usually constrain σ_8, the variance of the density of the Universe at a scale of $8h^{-1}$ Mpc. The other important parameter related

to the growth of density fluctuations is the shape of the primordial power spectrum. This is described as a power-law dependence, i.e. $P(k) \propto k^{n_s}$ where n_s is the scalar spectrum power law index. Both these parameters can be constrained by measuring the evolution of large scale structure.

1.1.2 Clusters as tests of cosmology

Most tests of cosmology based on either principle alone as discussed above can only provide constraints on a combination of various cosmological parameters. Hence, bringing together constraints from different methods and data samples is needed to break the degeneracy between the parameters. Galaxy clusters provide a different set of constraints from the distance-redshift relations, as they are representative of large scale structure formation and growth in the Universe. They provide two different methods for constraining cosmology.

Cluster mass function

The cluster mass function at a given z can be used to constrain the density fluctuation power spectrum at that redshift. The mass function, to a good approximation, can be expressed as follows [e.g. Mantz et al., 2010b].

$$\frac{\mathrm{d}n(M, z)}{\mathrm{d}M} = \frac{\overline{\rho}_m}{M} \frac{\mathrm{d}\sigma^{-1}}{\mathrm{d}M} f(\sigma) \tag{1.9}$$

where $\overline{\rho}_m$ is the mean comoving matter density such that $M = 4\pi\overline{\rho}_m r^3/3$ is the mass within a top-hat filter of comoving radius r, and σ^2 is the variance of the density field as defined in equation (1.8). $f(\sigma)$ determines the shape of the mass function and can be either an analytical or semi-analytical function, such as the Press-Schechter function, or can be calibrated using numerical simulations. Therefore, σ_8 can be constrained using accurate measurements of cluster masses.

Gas mass fraction

The mass content in clusters, specifically the baryon mass fraction, is expected to closely match the Universal value as clusters are the most massive and most recent gravitationally collapsed objects. Since the baryonic mass in clusters is dominated by the ICM gas mass, the baryon fraction is sometimes approximated as the gas mass fraction (while stellar mass is ignored here, it may be important in some cases as seen later), i.e. $f_{baryon} \approx f_{gas} =$

$M_{gas}/M_{cluster} \approx \Omega_b/\Omega_m$. Hence again, measurements of f_{gas} require accurate measurements of cluster mass as well as gas mass. Analysis of the angular power spectrum of temperature fluctuations in the CMB can provide an independent measure of Ω_b, so along with f_{gas}, it can be used to determine Ω_m for the Universe [Allen et al., 2008].

1.2   Detection and observations of galaxy clusters

As seen above, most tests of cosmology involving galaxy clusters rely on accurate determination of the cluster mass and redshift. Galaxy clusters have several unique signatures in different observation bands that can be used to detect them in surveys. Since this study is primarily an optical analysis of Abell 133 and some comparison with an X-ray study, these two techniques will be our main focus; two other significant methods based on the SZ effect and gravitational lensing are also briefly described here.

1.2.1   Optical

Cluster detection in the optical regime uses photometric observations of the cluster in multiple bands. Clusters were first detected as overdensities in the distribution of the projected galaxy number density. The cluster mass could be estimated using the total optical luminosity and richness, by assuming a mass-to-light ratio. However, catalogues produced using this technique were very susceptible to projection effects, where false positives would be obtained due to chance clustering of galaxies that are physically separated by large distances. Also, fewer clusters can be detected at higher redshifts as the galaxy contrast reduces. Besides, this method of cluster detection may be biased against optically dark clusters that do not have a significant number of galaxies, although there is little evidence of this. It may also be affected by galaxy evolution, i.e. the galaxy populations sampled may change with redshift [Voit, 2005, Varela et al., 2009].

Rich galaxy clusters possess a unique property in that they have a large population of old galaxies with uniformly similar spectral properties, so they lie on a tight locus on a colour-magnitude diagram in the optical or near infrared (NIR) bands. This feature is not seen in any random sample of field galaxies and hence, it can be used to detect clusters using various cluster detection algorithms, as shown by Gladders and Yee [2000]. This selection method is a powerful tool for cluster detection, since the red sequence is a tight relation on the colour-magnitude diagram with small scatter, especially for early-type galaxies. The detection only requires photometry in 2 filters, as long as the two contain the

4000Å break. Since the early-type galaxies are more luminous at higher redshifts, clusters can be detected out to high redshifts. Also, these ellipticals are expected to be the oldest and therefore reddest galaxy population at a given redshift; in fact, for filters containing the 4000Å break, the red sequence galaxies are as red or redder than other galaxies at the same redshift or lower. This means that there is little contamination by foreground galaxies, and of the background galaxies, it is mostly the "blue cloud" population that might be redshifted onto the red sequence. Hence, any projection effects are largely reduced using this method. The contamination by background galaxies can be further reduced by using colour-magnitude relations in several optical/NIR bands. Finally, the colour of the red sequence is a good indicator of redshift as well.

While photometric redshifts can be obtained from imaging in multiple optical bands, it is usually desirable to carry out spectroscopy on a subset of the cluster galaxies as spectroscopic redshifts are much more precise. Redshifts are necessary for velocity dispersion measurements, which provide another method for estimating the cluster mass using the virial theorem. One virial mass estimate is calculated as follows [Girardi et al., 1998].

$$M_{vir} = \frac{\langle v^2 \rangle}{G \langle r^{-1} F(r) \rangle} = \frac{3\pi}{2G} \sigma_{v,1D}^2 R_{vir} \tag{1.10}$$

where r is the distance of a galaxy from the cluster centre, the velocities v are in the cluster reference frame and $\sigma_{v,1D}$ is the radial velocity dispersion. $F(r)$ is the mass fraction within r and is dependent on the density profile of the cluster. The factor of $3\pi/2$ is due to the transformation from 3D to 2D radii and the assumption of velocity isotropy, i.e. $\sigma_v^2 = 3\sigma_{v,1D}^2$. The weighted projected virial radius is calculated as

$$\frac{1}{R_{vir}} = \left(\sum_i^{N-1} \sum_{j>i}^N w_i w_j \right)^{-1} \sum_i^{N-1} \sum_{j>i}^N \frac{w_i w_j}{R_{ij}} \tag{1.11}$$

where R_{ij} is the projected distance between a pair of cluster galaxies and w_i and w_j are weights assigned to the two galaxies based on completion, as explained later. Another mass estimate is based on a required mass overdensity relative to the critical density of the Universe,

$$M_\Delta = \Delta \frac{4\pi}{3} R_\Delta^3 \rho_c = \Delta \frac{1}{2G} R_\Delta^3 H^2 \tag{1.12}$$

along with the virial theorem [Mo et al., 2010].

$$\frac{GM_\Delta}{R_\Delta^2} = \frac{\sigma_{v,1D}^2}{\gamma R_\Delta} \tag{1.13}$$

Here, Δ is the required overdensity, commonly 200 or 500, and γ is a parameter that encompasses the mass distribution of the cluster and the velocity anisotropy. The major difference in the two methods is in the definition of the virial radius. Disadvantages to using both these methods are that they assume dynamical equilibrium, which may not be valid if the cluster is still virializing, and they require some assumptions about the velocity anisotropies in the cluster.

1.2.2 X-ray

The CDM paradigm of structure formation is a hierarchical process, whereby larger structures are formed through mergers and accretion of smaller structures. During the process of accretion, gas falling into the cluster potential well is shock heated to extremely high temperatures ranging from 10^7 to 10^8 K. The gas produces radiation due to bremsstrahlung and line emission, which makes clusters highly luminous in X-ray imaging as diffuse sources that cannot originate in single galaxies. The X-ray luminosity L_X is determined by the mass, temperature and distribution of the gas. Emission line strengths can be used for measuring element abundances. While the thermal bremsstrahlung emission is dominant for $kT \gtrsim 2$keV, line emission is important for $kT \lesssim 2$keV. X-ray observations also contain information regarding the temperature of the gas, which is determined by the cluster potential well [Voit, 2005].

The surface brightness profile is measured in terms of an emission measure EM $= \int n_e n_p \mathrm{d}V$, where n_e and n_p are the electron and proton number densities and are related to the gas density $\rho_g \propto \sqrt{n_e n_p}$. The 3D gas density distribution in clusters is well represented by a β model [Cavaliere and Fusco-Femiano, 1978].

$$n_e n_p = \frac{n_0^2}{\left(1 + r^2/r_c^2\right)^{3\beta}} \tag{1.14}$$

Further modifications are added to better describe the profiles typically seen in clusters such as a more cusp-like profile towards the centre instead of a core or a steeper profile than the β model at larger radii [e.g. Vikhlinin et al., 2006]. Spectral analysis of the X-ray data gives the temperature profile for the cluster, while the surface brightness can be used to measure the density profile of the gas under the assumption of hydrostatic equilibrium (H.E.) as well as the total gas mass M_{gas}. The entropy K is represented by a parameter S [McCarthy et al., 2004],

$$S = \frac{k_b T}{n_e^{2/3}} = K \left(\frac{n}{n_e}\right)^{2/3} (\mu m_H)^{5/3} \tag{1.15}$$

9

which is obtained from the temperature and density profiles. The total cluster mass can be estimated in several ways - using scaling laws between L_X and total mass, using the M_{gas} as a proxy for the total mass, or directly from the temperature and gas density profiles [e.g. Vikhlinin et al., 2006].

$$M(r) \propto T(r)r \left[\frac{\mathrm{d}\ln\rho_g}{\mathrm{d}\ln r} + \frac{\mathrm{d}\ln T}{\mathrm{d}\ln r} \right] \qquad (1.16)$$

The X-ray luminosity L_X correlates well with the cluster mass, with a low scatter and regardless of the dynamical state of the cluster [e.g. Kravtsov et al., 2006, Benson et al., 2013], although some studies based on numerical simulations show that the intrinsic scatter in the luminosity-mass relation is dependent on the initial entropy injection level as well as the cooling core status of the cluster McCarthy et al. [2004]. The emissivity of the gas is dependent on the square of the ion density in the ICM gas n_e^2. It is therefore not strongly affected by chance projections from structures along the line of sight. This also means that the cluster cores where the density is highest are highly luminous making them readily detectable in X-ray imaging [Zhang et al., 2010]. However, X-ray observations do involve certain biases and selection effects that must be accounted for. One key issue here is that most observables from X-ray imaging rely on the assumption of hydrostatic equilibrium i.e. gas acceleration is neglected. These assumptions may not be valid in clusters with disturbed morphologies or in the outer regions of the clusters [Hao et al., 2010]. Also, the gas luminosity is sensitive to the complex physics near the cluster core and various processes such as radiative gas cooling or merging, which introduce some amount of scatter into the luminosity scaling relations [e.g. Fabian et al., 1994, Lima and Hu, 2005]. For X-ray emission, the ICM gas has to be heated to very high temperatures, which requires a deep potential well. Hence, this technique tends to select high-mass clusters. The selections could also potentially be biased against gas-poor clusters or clusters with very compact gas distributions.

1.2.3   Sunyaev Zel'dovich effect

While X-ray imaging is a powerful cluster detection technique, it is dependent on redshift i.e. cluster detection becomes difficult at high redshifts. The SZ effect method does not suffer from the same problem. First predicted by Sunyaev and Zeldovich [1972], this effect is seen as a distortion in the CMB due to CMB photons undergoing inverse Compton scattering from the hot ICM gas. The effect is small and therefore, has only recently been used for cluster observations with the availability of large detector arrays on high resolution

telescopes. However, since this is a scattering effect, it is not redshift-dependent i.e. the surface brightness of the SZ effect does not depend on redshift. It only depends on the density and temperature of the ICM gas, and thus, traces its thermal pressure. The SZ effect method is also not very sensitive to projection effects, but it tends to find higher mass systems as the signal is more pronounced for more massive clusters [Hao et al., 2010].

1.2.4 Gravitational lensing

Gravitational lensing is also an important technique for structure finding. Light from background sources is bent due to massive structures, resulting in either multiple images of the source (strong lensing) or in distortions in its image (weak lensing). Clusters can be detected through their weak lensing signal. The advantage of this technique is that it is entirely independent of the dynamical state of the cluster and it does directly trace its total mass; however, it is prone to projection effects as the incident light may be affected by multiple systems along the way; studies have found that the noise due to projection effects of uncorrelated large scale structure in lensing cluster mass estimates is not negligible [e.g. Becker and Kravtsov, 2011, Hoekstra et al., 2011].

1.3 Motivation for present work

As mentioned above, due to the n_e^2 dependence of the X-ray luminosity, the surface brightness profile of the gas drops rapidly at large radii. Hence, the outskirts of galaxies were not observed until recently, when suitable X-ray imaging became available due to telescopes such as the *Suzaku*, which has a low background that makes it easier to detect fainter structures. This has made it possible to extend cluster f_{gas} measurements out to the virial radius and beyond. Observations within smaller radii and those extended to beyond the virial radius have produced two important results - possible gas clumping in the cluster outskirts and missing baryons within the inner regions of the cluster.

1.3.1 Outskirts of clusters

Several recent observations of the outskirts of clusters near and beyond the virial radius, usually taken to be r_{200}, have found that the entropy profiles in these regions are shallower than the $r^{1.1}$ dependence predicted by simulations [e.g Voit et al., 2005]. Most studies attribute this to a breakdown of hydrostatic equilibrium, which is expected at and beyond

the virial radius where the cluster is accreting mass. They also find values of f_{gas} that are higher than the cosmic baryon fraction Ω_b/Ω_m obtained from CMB data. One possible explanation for this is that the distribution of gas in these regions is fairly clumpy, resulting in density concentrations. As the surface brightness traces n_e^2 instead of just the gas density n_e, the clumpiness would lead to a much higher surface brightness and an overestimation of gas density in those regions. It should be noted that most of these studies do not directly observe this clumpiness, it is inferred from the entropy profile. These flattened entropy profiles were found in studies of several clusters such as Perseus, Virgo, PKS 0745-191 and Abell 1385, described in further detail here, as well as those of Abell 2029 [Walker et al., 2012b], Abell 1795 [Bautz et al., 2009], Abell 1413 [Hoshino et al., 2010] and Hydra A [Sato et al., 2012] amongst others.

Simionescu et al. [2011] studied the Perseus cluster, which is a relaxed system, using *Suzaku* observations along two strips starting at the cluster centre. They found that the f_{gas} value agreed with the cosmic baryon fraction at $\sim 0.5r_{200}$ i.e. they do not see any baryon deficit observed in other studies. Beyond $\sim 2/3r_{200}$, they found that f_{gas} exceeded the cosmic value. They suggest that this is due to gas clumping, which has been predicted by numerical simulations [Roncarelli et al., 2006], although the effect is highly sensitive to the input physics governing the gas. The Simionescu et al. [2011] results are shown in Figure 1.1. Similar results were obtained by Urban et al. [2011] who studied the Virgo cluster using XMM-Newton data. Most clusters that have been investigated for gas clumping are massive, relaxed systems. By contrast, Virgo is the nearest and brightest cluster at a distance of 16Mpc, moderately-sized and dynamically young. They found temperature and surface brightness profiles that were shallower than predicted by numerical simulations. A temperature drop of $\sim 60\%$ is seen between $(0.3 - 1)r_{vir}$. Beyond a radius of $r \sim 450$ kpc, the temperature and metallicity is seen to drop abruptly and the entropy profile deviates from the $r^{1.1}$ power law. The most likely explanation for these results is suggested to be gas clumping.

This topic is currently still unresolved and some studies do suggest either that the scenario is not consistent with observations or that is not sufficient to fully account for the high f_{gas} measured. Walker et al. [2012a] found similar entropy profile and f_{gas} results for PKS 0745-191, which suggest that the ICM is not in hydrostatic equilibrium and the gas is possibly clumpy. After correcting for this clumping factor, the entropy profile agreed better with the $r^{1.1}$ profile out to $\sim r_{200}$, but beyond this radius, the profile was still flattened, suggesting that there is some other process causing the high f_{gas} and flattened entropy. Ichikawa et al. [2013] examined Abell 1385 out to its virial radius and found that temperature decreases gradually out to r_{vir}, while the density profile continuously steepens. Within r_{500}, the entropy profile agrees with $r^{1.1}$; at larger radii, they find that lensing mass
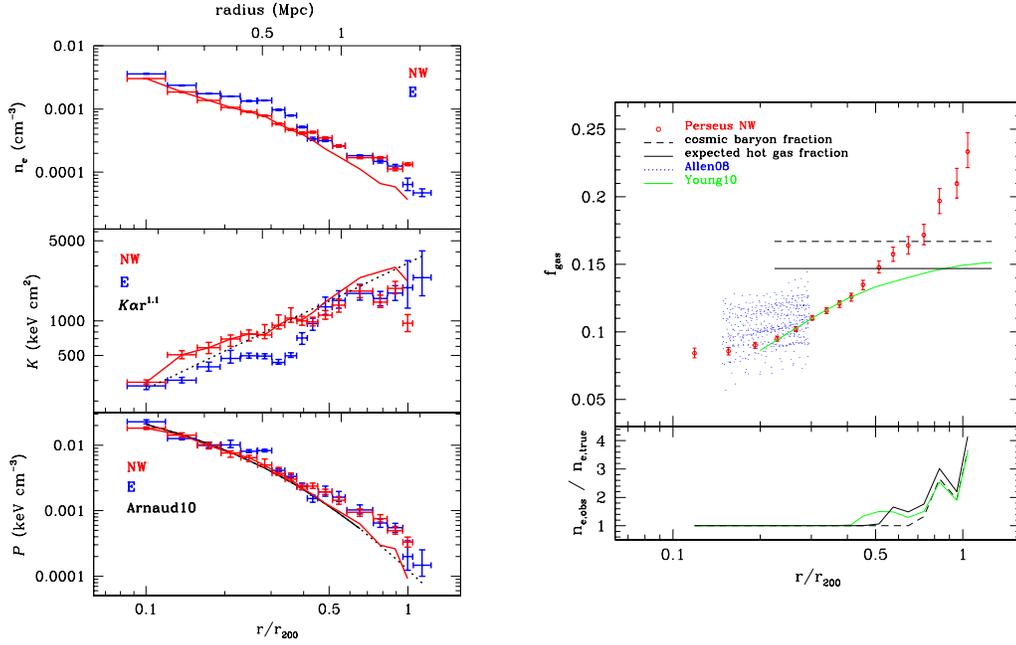
Figure 1.1: Results from Simionescu et al. [2011] for *Suzaku* observations of the Perseus cluster in two strips in the NW and E directions. *Left:* Deprojected electron density, entropy and pressure profiles. The red line shows the NW results, corrected for clumping. The entropy profile is flatter than the predicted $r^{1.1}$ profile beyond $2/3r_{200}$. *Right:* Gas mass fraction profile for the NW strip (red dots). The dashed line denotes the cosmic baryon fraction from WMAP7 [Komatsu et al., 2011]; the solid black line shows the expected hot gas fraction by accounting for the 12% of baryons in stars [Lin and Mohr, 2004, Gonzalez et al., 2007]. Earlier results from a sample of relaxed clusters from Chandra [Allen et al., 2008] are shown by the blue dots and predictions from simulations [Young et al., 2010] by the green line. *Bottom:* Comparison between electron density with and without clumping correction.
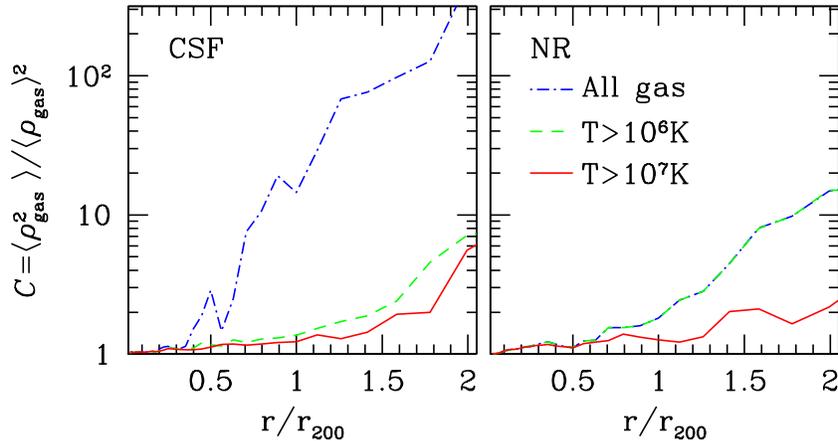
Figure 1.2: Results from Nagai and Lau [2011] from hydrodynamic simulations of clusters using two different models - cooling and star formation (CSF) and non-radiative (NR). The plots are the clumping median clumping profiles for the two models carried out for gas of two different temperatures, as well as for all gas in the cluster.

estimates were higher than the mass derived assuming hydrostatic equilibrium, while the f_{gas} continuously increases. They conclude that these results are due to a breakdown of hydrostatic equilibrium as opposed to gas clumping.

Recently, Nagai and Lau [2011] studied this gas clumping using 16 simulated clusters, using two different models - one with gas cooling and star formation (CSF) and one without, referred to as the non-radiative model (NR). Clusters form through mergers and accretion of smaller systems and simulations predict that accretion would cause internal motions in the gas and inhomogeneities in the gas distribution, resulting in clumpiness. They defined a clumping factor for the X-ray emitting gas ($T > 10^6$ K).

$$C = \frac{\langle \rho_{gas}^2 \rangle}{\langle \rho_{gas} \rangle^2} \tag{1.17}$$

Their results are shown in Figure 1.2. They found large variations in the clumping profile from cluster-to-cluster. For the median profile, the clumping factor $C \sim 1$ within $r < 0.5r_{200}$; it rises gradually to $C \sim 1.3$ and 2 around $r = r_{200}$ for the CSF and NR runs respectively. Beyond r_{200}, the clumping factor rises rapidly to $C \sim 5$ and 10 by $r = 2r_{200}$ for the CSF and NR runs. They found that it was generally higher in unrelaxed systems.

When considering the hotter gas with $T > 10^7$ K, the clumping profile dropped slightly for the CSF runs, but for the NR runs, the profile dropped significantly. When considering gas of all temperatures, the results are heavily influenced by cluster physics i.e. cooling and star formation. Hence, the profile rises considerably for the CSF model, but not for the NR runs. They also found that the clumping was generally higher in higher mass systems and that there was very mild evolution with redshift. However, the physical scale of this clumping was not stated and requires further study. Considering the influence of this clumping on X-ray observations, they found that it would cause density to be overestimated in the CSF models by 15% at r_{200} and 120% by $r = 2r_{200}$.

1.3.2   Missing baryon problem

The missing baryon problem is the observation that the gas mass fraction in galaxies and clusters, which are lower redshift systems, is found to be much lower than the cosmic baryon fraction inferred from CMB data, which is the baryon content at much higher redshift. (The cluster measurements were in the inner regions, within $\sim r_{500}$). The expectation is that baryons at high redshift should have undergone gravitational collapse into stars and eventually galaxies and clusters, so that the baryon fraction in these systems should not be too different from the CMB values. The effect is less severe in clusters where the gas mass dominates the baryon mass, especially in massive, relaxed systems. The addition of the stellar mass from the cluster galaxy luminosities appears to bring the baryon fraction close to the CMB value. This would indicate that the effect is correlated with the gravitational potential well depth of the object. Due to the importance of f_{gas} measurements in cosmology, several studies are currently being conducted to understand the origin of this missing baryon problem and the transition mass scale. Dai et al. [2010] found indications that the baryon loss mechanism seemed to be universal and mainly related to potential well depth. One possible mechanism put forth is the pre-heating of baryons as they are accreted onto the cluster, so that they never fall into galaxies or groups and remain on the outskirts of the cluster. Another scenario is that the gas did fall into the potential well, but was later ejected due to various processes such as supernovae or feedback from Active Galactic Nuclei (AGN). However, there are some challenges to this theory, since similar baryon fractions were measured in clusters with similar potential well depths, but varying stellar-to-gas ratios, which would affect the rate of supernovae in the cluster. Another key issue is understanding how clusters can have higher baryon fractions than galaxies in a hierarchical growth model, such as the ΛCDM cosmology, where clusters are formed through mergers and accretions of galaxies and smaller groups.

1.3.3   Abell 133

The objective of the present analysis was to determine if any possible clumping in the gas distribution of a cluster is correlated with stellar substructure; this required high-quality, spatially-resolved, X-ray imaging extended out to beyond the virial radius, along with optical imaging and spectroscopy for studying the stellar properties of the cluster. Abell 133 made a very good candidate for this analysis; new deep and wide *Chandra* imaging had been recently obtained for the cluster, with an exposure time of $\sim$ 2Ms, covering a large area beyond its virial radius and imaged in all directions. This is one of the deepest X-ray images obtained for a cluster and it allows the analysis of the entire outskirts of the cluster, which has not been possible before. There were also existing optical images from the Canada-France-Hawaii Telescope (CFHT) Megapipe, covering a large 1 sq. deg. area, in the g' and r' bands. This allowed for a preliminary analysis and better understanding of the cluster before carrying out further observations for obtaining redshifts. Following this, spectroscopy was obtained for $\sim$ 1870 galaxies, which yielded about 700 secure redshifts. Combining the photometric and spectroscopic data, we were able to examine the X-ray overdensities in the cluster and determine if they were associated with the cluster. All distance calculations in the analysis are based on a standard ΛCDM cosmology with $\Omega_m = 0.3$, $\Omega_\Lambda = 0.7$ and $H_0 = 70$ (km/s)/Mpc.

Chapter 2

Photometric Study

Abell 133 is a rich galaxy cluster at a redshift of $z = 0.0569$ with an average temperature of $kT = 4.01$ keV and an X-ray luminosity of $L_X = 9.60 \times 10^{43}$ ergs/s in the (0.5-2 keV band) as determined by the *Chandra* Cluster Cosmology Project [Vikhlinin et al., 2009a]. Using various scaling relations between X-ray observables and cluster mass, they found an estimated total mass within R_{500} in the range of $M_{500} = 2.37 - 2.91 \times 10^{14} M_\odot$. Zhang et al. [2011] found a velocity dispersion of 725 km/s using 137 cluster galaxies from the HIghest X-ray FLUx Galaxy Cluster Sample (HIFLUGCS) [Reiprich and Böhringer, 2002]. They report an X-ray bolometric luminosity of 1.54×10^{44} ergs/s. They also find a gas mass within R_{500} of $2.31 \times 10^{13} M_\odot$. For comparison, Valentinuzzi et al. [2011] find a velocity dispersion of 810 km/s. Figure 2.1 is a *Chandra* X-ray map of the cluster.

2.1 Data

2.1.1 Optical imaging of Abell 133

Data for the photometric analysis were obtained from the CFHT Megapipe [Gwyn, 2008] which provides stacked images and catalogues built using the Sextractor software [Bertin and Arnouts, 1996]. Two images for Abell 133 were used, one each in the g'- and r'- band. Each of these images has dimensions of about 20000×20000 pixels, covers a ~ 1 sq. deg. area of the sky, has a total exposure time of 1320s and consists of 11 input images. The g'-band image has a 5σ limiting magnitude of 26.5 and an overall image quality of 0.87", while the r'-band image has a limiting magnitude of 25.7 and an image quality of 0.92". The two
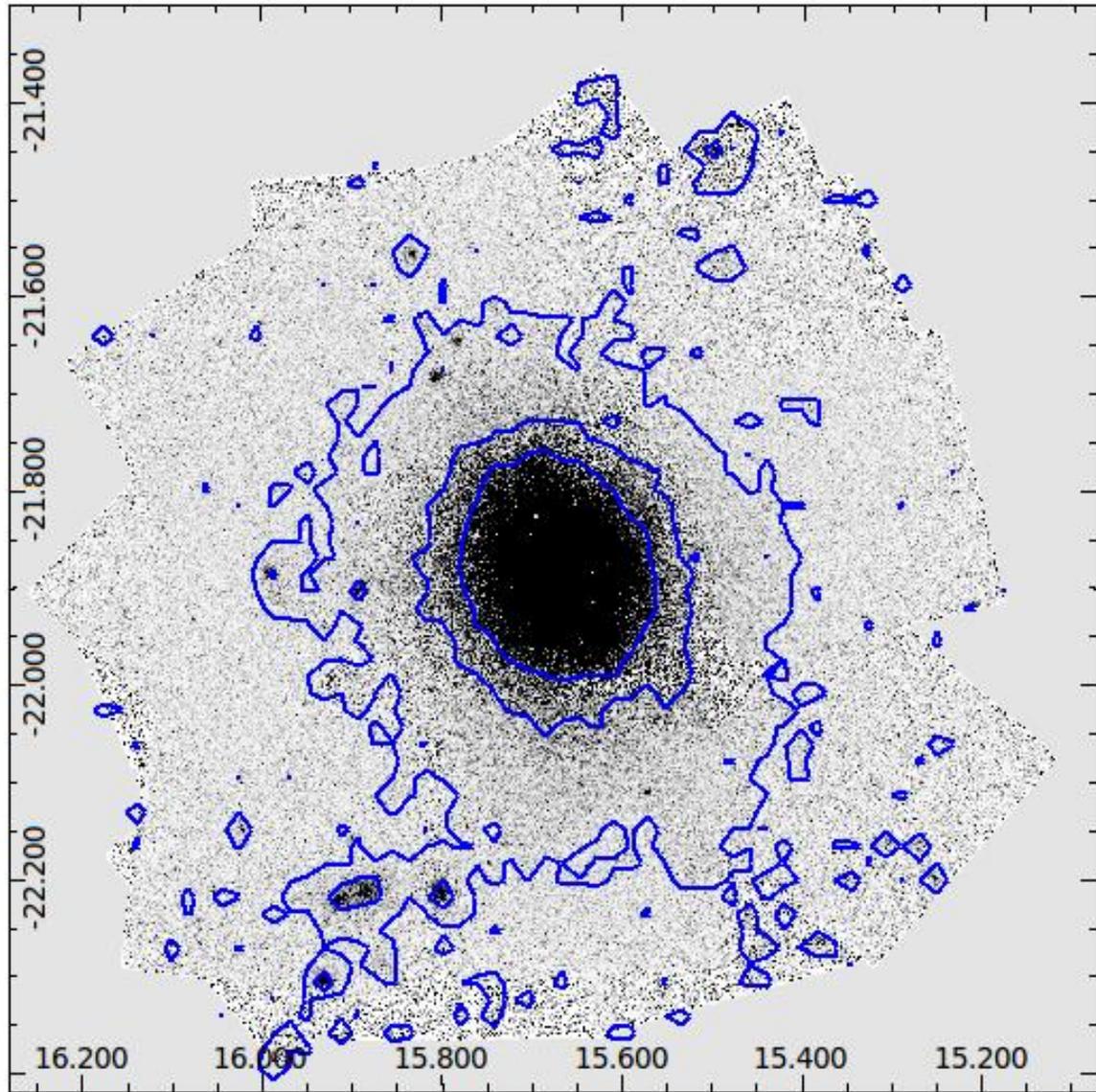
Figure 2.1: *Chandra* X-ray image of Abell 133 showing X-ray logarithmic contours.

catalogues were combined by selecting g'-band objects within a $0.0008° \times 0.0008°$ window in α and δ around each r'-band object and then finding the closest match. Distances were calculated as follows.

$$\Delta\theta = \sqrt{\left[\delta_2 - \delta_1\right]^2 + \left[(\alpha_2 - \alpha_1)\cos\left(\frac{\delta_1 + \delta_2}{2}\right)\right]^2} \qquad (2.1)$$

Any objects from the r' catalogue for whom no match was found, as well as any objects from the g' catalogue not matched to anything in the r' catalogue were discarded. The *mag_auto* value was used for the r' magnitude (*mag_auto* is an automatic Kron-like elliptical aperture magnitude), while the *mag_aper* values were used to calculate the colour (g'-r') (*mag_aper* is a fixed aperture magnitude). The radius listed for the objects in the catalogue is the half-light radius in pixels. All objects with an Sextractor flag ≥ 5 were removed, except for those close to the centre (an area covering $\sim 4.5' \times 6'$), where objects with a flag ≥ 30 were removed; this was done because the former criterion excluded some of the bright galaxies in the centre and the specific flags did not pose a problem for those objects.

2.1.2   CFHTLS data

In order to determine the significance of any potential substructure found in Abell 133, data were obtained from the CFHT Legacy Survey Wide 1 (CFHTLS-W1) field [Gwyn, 2012]. The Wide 1 field consists of 72 individual images, each covering a ~ 1 sq. deg. area of the sky in a 9×8 grid, with some overlap between adjacent pointings. The images have total exposure times between $2180 - 6360$s in the r'-band and between $2000 - 8000$s in the g'-band; the limiting magnitudes for each (these are the point-source 50% completeness limits) are between $25.5 - 26.2$ in the r'-band and between $26.1 - 26.9$ in the r'-band. Galaxies within a $\sim 7° \times 7°$ area between ($31° < \alpha < 38°$) and ($-11° < \delta < -4°$) were selected for the analysis. Again, the *mag_auto* value is used for the r' magnitude and the *mag_aper* values for colour.

2.1.3   SDSS data

In order to determine how good the red-sequence cluster member selection is, spectroscopic data for galaxies from the Sloan Digital Sky Survey (SDSS) were also obtained for a random sample of field galaxies within ($120° < \alpha < 150°$) and ($15° < \delta < 45°$). The data consist of photometry in the u', g', r' and i' bands, along with a spectroscopic redshift.
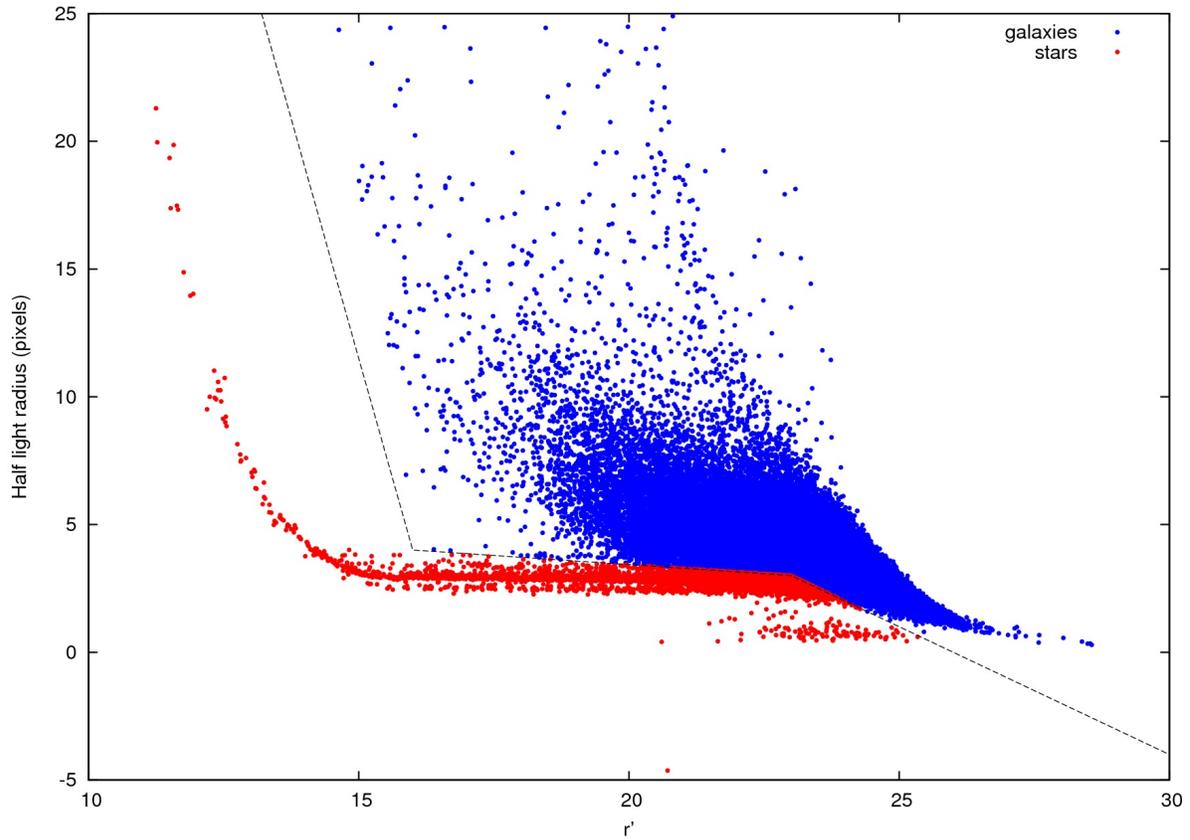
Figure 2.2: Plot of half-light radius vs. magnitude in the r'-band catalogue showing the locus of stars and the conditions used to differentiate between stars (red) and galaxies (blue).

2.2 Identifying cluster members

2.2.1 Removal of stars from catalogue

Before determining which galaxies belong to the cluster, the first step was to remove the stars from the combined catalogue. This was done using the locus of the stars on a magnitude-radius plot. Figure 2.2 is the plot of radius vs. r'-magnitude, showing those objects selected as galaxies and those removed as stars. Also, any objects with $-10 < $ (g'-r') < 10 were removed, as these were usually the result of one or both magnitudes being set to -99 when no value was measured for it by Sextractor. This resulted in 81214 objects selected as galaxies. However, as can be seen from Figure 2.2, there appears to be
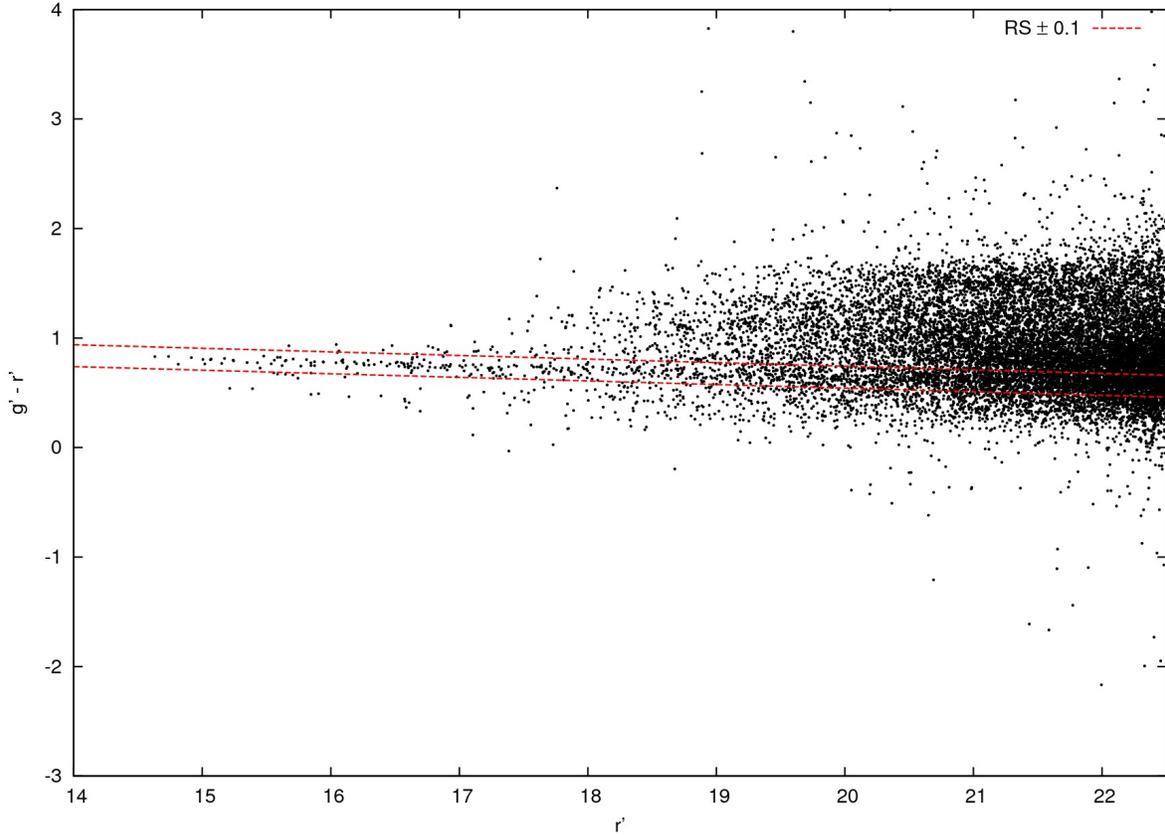
Figure 2.3: Colour-magnitude diagram for all galaxies, showing the band around the final red sequence fit used to select probable cluster members within the red sequence.

a surface brightness limit around r'= 22.5; at magnitudes fainter than this, the analysis was also likely to be swamped by background galaxies. Hence, the rest of the analysis is limited to $r' < 22.5$, giving 14907 galaxies in total.

2.2.2 Red sequence analysis

Figure 2.3 shows the colour-magnitude diagram of the galaxies in the image. There is a prominent red sequence seen on the plot, corresponding to the cluster members. The parameters for a linear red sequence were calculated using a linear least squares fit (unweighted) to the data by solving the following system of linear equations. Only galaxies within a $\sim 0.4° \times 0.4°$ area around the cluster centre were used for the red sequence fitting,

since the outer regions would have more noise resulting from galaxies not associated with the cluster.

$$a_1 \sum_{i=1}^{N} (r'_i)^2 + a_2 \sum_{i=1}^{N} r'_i = \sum_{i=1}^{N} (g' - r')_i (r'_i) \tag{2.2}$$

$$a_1 \sum_{i=1}^{N} (r'_i) + N a_2 = \sum_{i=1}^{N} (g' - r')_i \tag{2.3}$$

Here, a_1 is the slope and a_2 is the $(g' - r')_i$ offset. The fit was initially based on bright galaxies within a broad colour slice between $0.5 < (g'\text{-}r') < 1$ and with r' < 20. Two more iterations of the fit were then carried out, each by first rejecting galaxies beyond $\pm 1\sigma_{RS}$ of the red sequence from the previous fit, where σ_{RS} is the RMS scatter about the red sequence; galaxies with $(g' - r')$ within ± 0.1 of the colour predicted at their magnitude by this red sequence were then selected as probable cluster members. The final fit gave $a_1 = -0.0328$ and $a_2 = 1.2982$; this resulted in 3244 red-sequence galaxies up to r'< 22.5. The final fit is also shown in Figure 2.3. These selection criteria, specifically the width of the red sequence and the limiting magnitude used, affect any optical structure identified later. Therefore, we did examine the intensity maps described later using different red sequence widths and magnitude cut-offs. The criteria used here were a good compromise between including more cluster members and reducing the noise in the data.

2.3 Cluster intensity profile

The cluster-centric intensity profile was determined using the red sequence galaxies obtained in the previous section, within a radius of $0.4°$ from the cluster centre as this is the largest region that entirely falls on the image (the Brightest Cluster Galaxy (BCG) is used as the cluster centre in all further calculations.) Both linear and logarithmic binning was used to measure the profile. The flux and intensity in each bin, f_b and I_b respectively, was measured as follows

$$f_b = \sum_{R_{b,in} \leq R_i < R_{b,out}} 10^{23 - 0.4(48.6 + m_i)} \quad [\text{Jy}] \tag{2.4}$$

$$I_b = \frac{f_b}{\pi \left(R_{b,out}^2 - R_{b,in}^2 \right)} \quad [\text{Jy/deg.}^2] \tag{2.5}$$

where $R_{b,in}$ and $R_{b,outer}$ are the inner and outer projected radial limits of the bin in [deg.] and m_i is the r' magnitude for the galaxy. (Note: the BCG was not included in the

logarithmic intensity profile, since all the radii are measured relative to it and the BCG itself cannot be represented). The uncertainty in each of these measurements was determined using the Jackknife method. The intensity in each bin is a result of N_b galaxies. Therefore, N_b new measurements of I_b are made, each by skipping one of the galaxies at a time, giving

$$\hat{I}_{b,(i)} = \frac{N_b}{N_b - 1} \sum_{j \neq i}^{N_b} f_{b,j} \tag{2.6}$$

The rescaling is done since the value measured is a total intensity, which would depend on the number of galaxies contributing to it. Then the uncertainty in the intensity measurements is given by

$$\sigma_b^2 = \frac{N_b - 1}{N_b} \sum_{i=1}^{N_b} \left[\hat{I}_{b,(i)} - \frac{1}{N_b} \sum_{j=1}^{N_b} \hat{I}_{b,(j)} \right]^2 \tag{2.7}$$

For any bin where $N_b = 1$, the uncertainty was taken to be Poisson noise i.e., $\sigma_b = I_b$.

The intensity profile was examined in comparison to a family of double-power-law models parametrized by the power η, as described by Tremaine et al. [1994]. The density of the models is described as

$$\rho(r) = \frac{\eta}{4\pi} \frac{\rho_s}{r^{3-\eta} (1+r)^{1+\eta}} \qquad 0 < \eta \leq 3 \tag{2.8}$$

where ρ_s is the normalization density and the 3-dimensional radius r is in units of a characteristic length scale r_s. The projected intensity profile as a function of the 2-dimensional projected radius R can be obtained by integrating equation 2.8 along the line of sight and assuming a constant mass-to-light ratio Υ.

$$I(R) = \frac{2}{\Upsilon} \int_R^\infty \frac{\rho(r) r \mathrm{d}r}{\sqrt{r^2 - R^2}}$$
$$= \frac{\eta \rho_s}{2\pi \Upsilon} \int_0^{\pi/2} \frac{r^{\eta-2} \mathrm{d}r}{(1+r)^{1+\eta} \sqrt{r^2 - R^2}} \tag{2.9}$$

Analytical solutions exist for these models for $\eta = 1, 2, 3$, the first two of which correspond to the Jaffe profile [Jaffe, 1983] and the Hernquist profile [Hernquist, 1990] respectively.

The projected intensity models for these three cases are as follows

$$I(R) = b_1 \left[\frac{\pi}{2X} + \frac{1 - (2 - X^2) Y}{1 - X^2} \right] \qquad \eta = 1 \qquad (2.10)$$

$$I(R) = b_1 \left[\frac{(2 + X^2) Y - 3}{(1 - X^2)^2} \right] \qquad \eta = 2 \qquad (2.11)$$

$$I(R) = b_1 \left[\frac{2 + 13X^2 - 3X^2 (4 + X^2) Y}{2 (1 - X^2)^3} \right] \qquad \eta = 3 \qquad (2.12)$$

where

$$X = \frac{R}{b_2} \qquad (2.13)$$

and

$$Y = \begin{cases} \frac{1}{\sqrt{1-X^2}} \cosh^{-1} \frac{1}{X}, & X < 1 \\ \frac{1}{\sqrt{X^2-1}} \cos^{-1} \frac{1}{X}, & X \geq 1 \end{cases} \qquad (2.14)$$

These three models were fit to the intensity profiles with both types of binning using a weighted χ^2 fit. The χ^2 fit minimized the logarithmic errors, i.e.

$$\chi^2 = \sum_b \left[\frac{\log I(R_b) - \log I_b}{\sigma (\log I_b)} \right]^2 = \sum_b \left[\frac{\log I(R_b) - \log I_b}{\left(\frac{1}{I_b \ln(10)} \right) \sigma_b} \right]^2 \qquad (2.15)$$

In addition to these models, the NFW model [Navarro et al., 1997] - another double-power-law model and one of the most important models for dark matter halos - was also considered. The density and the projected intensity profile for the NFW model is described as follows [e.g. Golse and Kneib, 2002].

$$\rho(r) = \frac{\rho_s}{r(1+r)^2} \qquad (2.16)$$

$$I(R) = \begin{cases} \frac{1}{X^2-1} \left(1 - \frac{1}{\sqrt{1-X^2}} \cosh^{-1} \frac{1}{X} \right), & X < 1 \\ \frac{1}{3} & X = 1 \\ \frac{1}{X^2-1} \left(1 - \frac{1}{\sqrt{X^2-1}} \cos^{-1} \frac{1}{X} \right), & X \geq 1 \end{cases} \qquad (2.17)$$

with X as defined above.

The intensity profile as well as the results of the model fitting are all shown in Figure 2.4 and the best fit parameters are given in Table 2.1. In both cases, the data is best fit by
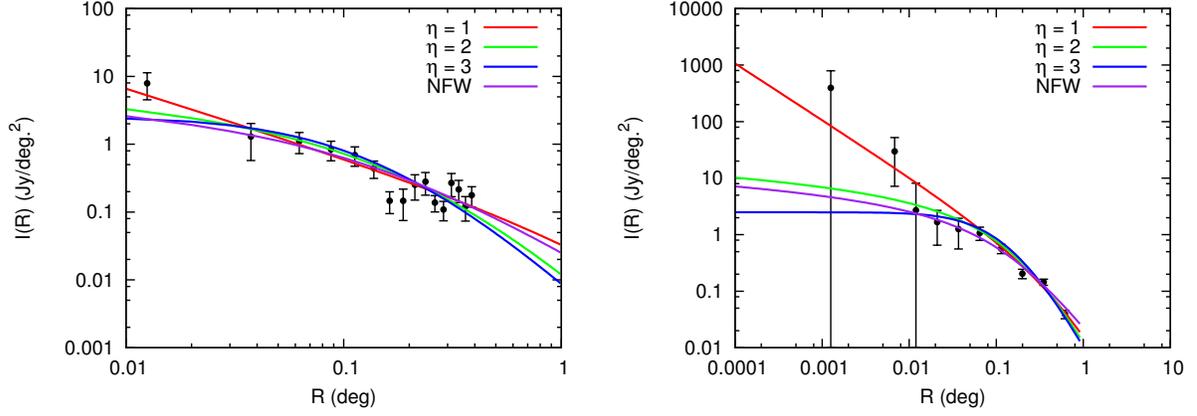
Figure 2.4: Cluster intensity profile with linear radial binning (left) and logarithmic radial binning (right), along with best fit models. For the linear profile, binning is $0.025°$ in a range of $0° \leq R < 0.4°$; for the logarithmic profile, binning is 0.2 dex within a range of $-4.0 \leq \log(R) < -0.4$.

Table 2.1: Model parameters for the four density models fitted using a χ^2 minimization, to the cluster intensity profile, b_1 is the combined normalization constant in $\left[\text{Jy/deg.}^2\right]$ and b_2 is the length scale in [deg.]. For the linear profile, binning is $0.025°$ in a range of $0° \leq R < 0.4°$; for the logarithmic profile, binning is 0.2 dex within a range of $-4.0 \leq \log(R) < -0.4$.

Model	Linear			Logarithmic		
	b_1	b_2	χ^2	b_1	b_2	χ^2
$\eta = 1$	0.01	4.28	19.1	0.07	0.97	14.2
$\eta = 2$	0.65	0.28	28.4	0.72	0.27	32.6
$\eta = 3$	2.55	0.13	35.7	2.49	0.14	49.2
NFW	0.01	0.18	27.9	0.01	0.17	32.6

25

the Jaffe model, followed by the Hernquist and NFW models which are both comparable, and finally the $\eta = 3$ model. However, while the Jaffe model appears to be a better fit at lower radii, the other three models agree better with the data at larger radii. The linear profile is not smooth at larger radii, which might be because the distribution of the cluster galaxies is not fully azimuthally symmetric.

2.4   Intensity mapping

In order to look for substructure in the cluster, a spatial map of the intensity was needed. This was obtained by measuring the r'-band flux from each red sequence galaxy and applying a Gaussian smoothing to it. The field was divided into a grid of 110×103 pixels, each having $\Delta\alpha = \Delta\delta = 0.01°$, and the Gaussian smoothed flux from each galaxy was added to the surrounding pixels within a radius of $0.15°$ from the galaxy. The intensity for each pixel is given by:

$$\mathrm{I}_{i,j} = \sum_{\substack{k=1 \\ R_k < 3\sigma_G}}^{N_{RS}} \mathrm{f}_{galaxy} \left[\frac{1}{2\pi\sigma_G^2} \exp\left(\frac{R_k^2}{2\sigma_G^2} \right) \right] \tag{2.18}$$

$\sigma_G = 0.05°$ is the scale length used for the Gaussian smoothing (corresponding to ~ 200 kpc) and R_k is the distance of the galaxy from the centre of the pixel. The resulting flux distribution map is shown in Figure 2.5, along with the X-ray image contours overlaid on it. The intensity in the outermost pixels at the edges is underestimated, since the Gaussian smoothing of the flux from galaxies outside the image area would have extended onto the edges of the image, adding to the intensity there. The figure shows firstly that the flux distribution is not azimuthally symmetric, with a prominent axis in the south-west to north-east direction. The map also shows that there is evidence of substructure in the outskirts of the cluster with about 4-6 possible clumps present. However, comparing with the X-ray contours, not all clumps in the optical image seem to coincide with all the overdensities in the X-ray map. Finally, because the distribution has some asymmetry, two prominent underdense regions are seen to the north-west and north-east of the cluster centre. This analysis was also carried out with different red sequence widths and limiting magnitudes, which produced very similar results.
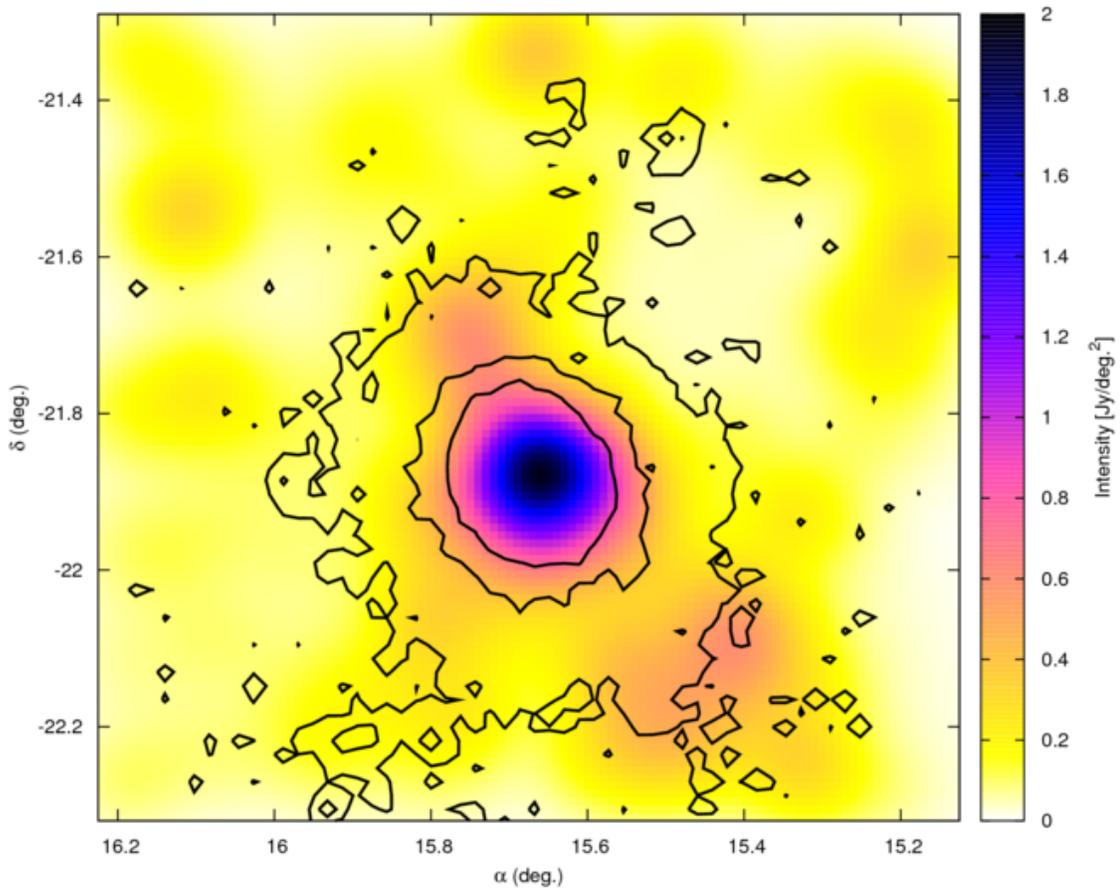
Figure 2.5: Spatial map of Gaussian smoothed intensity in a 110×103 grid with each grid element of size $\Delta\alpha = \Delta\delta = 0.01°$. The scale length of the Gaussian blur is $\sigma_G = 0.05°$ (corresponding to ~ 200 kpc) and flux from each galaxy is distributed to pixels within $3\sigma_G$ around it. Contours from the X-ray image (with logarithmic binning) are also overlaid.
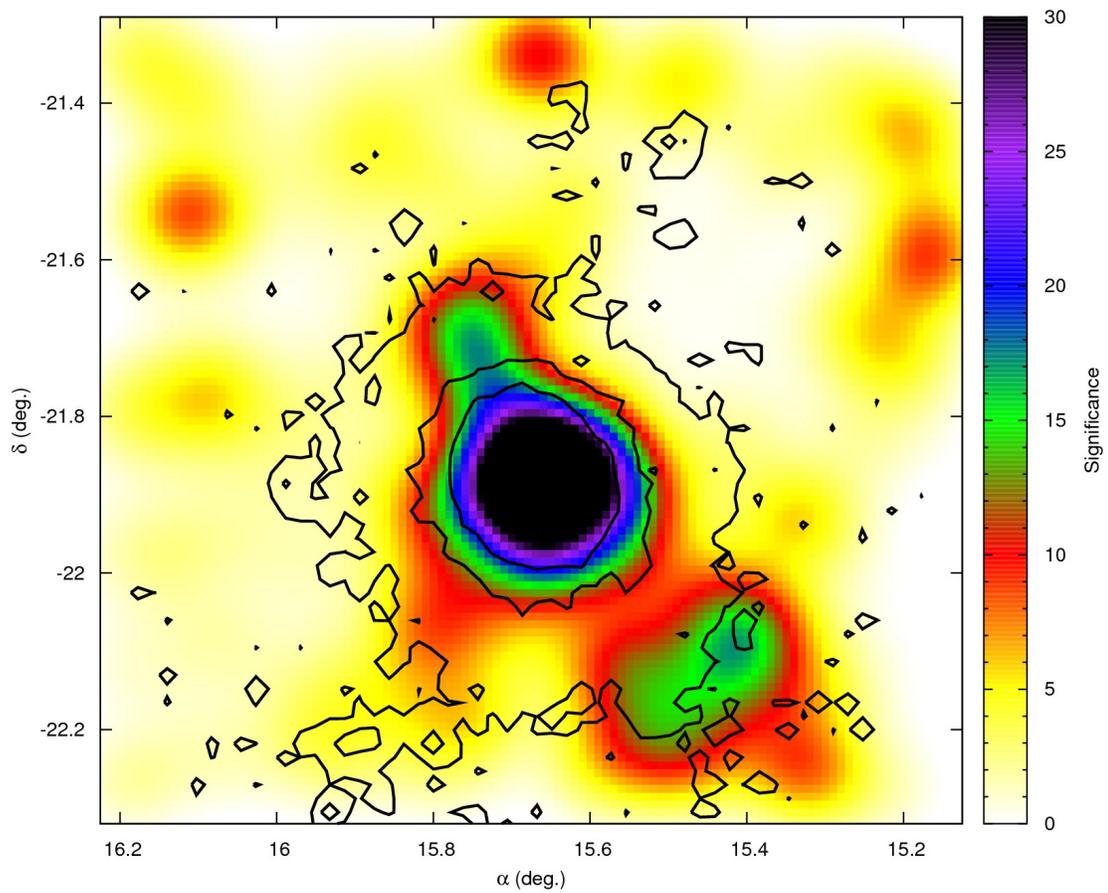
Figure 2.6: Map of significance of intensity as compared to the intensity map of the CFHTLS-W1 field. The central region has a much higher significance of about 60σ; however the image has been scaled in order to see the details in the outer regions better.

2.4.1 Measuring significance

Since some substructure was seen in Figure 2.5, the next step was to determine the significance of these results. Therefore, a similar intensity map was created of a larger random field using the CFHTLS data. Galaxies were selected from the CFHTLS-W1 field with $14 < r' < 22.5$ (to match the magnitude range of the cluster images, since the CFHTLS-W1 data have a different depth than those of the cluster) and within ± 0.1 of the cluster red sequence, using the same technique as before to remove stars from the catalogue. A similar intensity map was created with the same $\sigma_G = 0.05°$ and each element of size $\Delta\alpha = \Delta\delta = 0.01°$. (Note: The intensity map was extended to include the entire CFHTLS-W1 field and then limited to $(31° < \alpha < 38°)$ and $(-11° < \delta < -4°)$, so that the final map would not underestimate the intensity at its edges). The mean intensity $\overline{I}$ and standard deviation σ_I for a pixel was then measured, using every 50th column pixel in every 50th row, in order to ensure that even with the Gaussian smoothing, the values used are independent of each other. A significance $S_{i,j}$ is then assigned to each pixel from Figure 2.5 as

$$S_{i,j} = \frac{I_{i,j} - \overline{I}}{\sigma_I} \tag{2.19}$$

This does assume a uniform noise throughout both the Abell 133 image and the entire CFHTLS-W1 field; therefore, the significance here represents overdensities with respect to a uniform field. The significance map is shown in Figure 2.6. The central region has a significance of $\sim 60\sigma$; the map in Figure 2.6 has been scaled to a maximum significance of 30 to see the details of the map better. There are about 6 major clumps visible, along with 3-4 minor ones:

- 3 clumps in the outskirts of the cluster in the north-west, north and north-east regions with a significance of about 10σ

- 1 clump to the north-east, much closer to the cluster centre, of about 18σ significance

- 1 large clump to the south-west with a significance of $(15 - 18)\sigma$; this could consist of 2 or 3 subclumps

- 1 possible extended clump with a $(5 - 10)\sigma$ significance towards the south-east

- 3-4 possible smaller clumps around the outskirts with $< 10\sigma$ significance
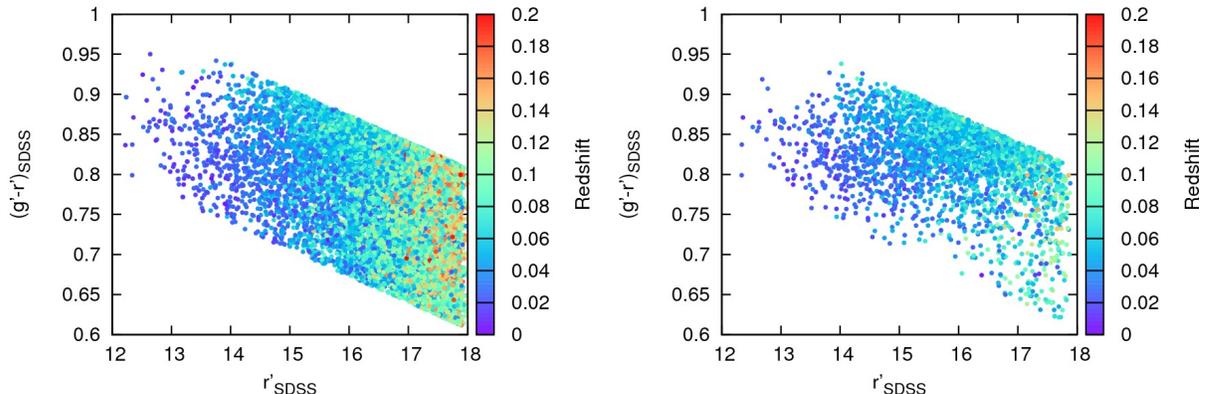
Figure 2.7: Improvement of redshift selection by incorporating additional colour information. *Left*: Galaxies selected from the SDSS field sample within $RS \pm 0.1$ of the Abell 133 red sequence. *Right*: Additional broad colour cuts of $[1.7 \leq (\text{u'-g'}) \geq 2.0]$ and $[0.3 \leq (\text{r'-i'}) \geq 0.45]$ applied to the selection on the left; a large fraction of background galaxies are removed by the additional colour cuts.

2.5   Discussion

The photometric analysis showed that there was indeed some substructure in the outskirts of the cluster in the form of about 6 major clumps in the spatial distribution of intensity. However, the clumps thus found did not seem to line up with all the overdensities seen on the X-ray image. Therefore, more analysis was needed to understand the nature of the X-ray overdensities, as well as to characterize the clumps found in the optical image. However, the red-sequence selection of cluster members was not accurate enough in redshift for further analysis and hence, better redshifts were needed, either spectroscopic or photometric. While spectroscopic redshifts are more precise, fewer galaxies can be targeted for it. Photometric redshifts using imaging in more filters would be able to cover many more galaxies, though the redshifts thus obtained have higher uncertainties.

If imaging in other filters was available for photometric redshifts, the possible improvement in redshift accuracy is demonstrated by the colour-magnitude diagrams in Figure 2.7. The plot on the left consists of galaxies selected from a random sample of field galaxies, using the SDSS data, within ± 0.1 of the red sequence of Abell 133. (As the sample consists of field galaxies, there is no red sequence seen here). The plot on the right consists of the same set of galaxies to which further colour cuts were applied: $[1.7 \leq (\text{u'-g'}) \geq 2.0]$ and $[0.3 \leq (\text{r'-i'}) \geq 0.45]$. These criteria were based on the distribution of the colour within a redshift

range of ±0.005 around the cluster redshift of 0.0569. The first figure shows that a single red sequence selection picks up galaxies with a wide range of redshifts at all magnitudes. The second figure then shows how the application of the additional colour cuts can remove a large number of the background galaxies. Even with these simple, broad colour cuts, the fraction all the selected galaxies that were at the correct redshift (i.e.0.0569 ± 0.005) improved from 0.077 to 0.151. Imaging in other filters would have provided more colour-magnitude relations for much tighter criteria, which would have significantly improved the redshift accuracy.

CFHT proposal   Since there could be considerable improvement in the cluster member selection using imaging in other filters, a proposal was submitted for more telescope time on the CFHT in the u*, i' band filters on MegaCam and the K filter on WirCam. Besides being useful in removing background galaxies, the u* band data (along with existing NUV and FUV data from GALEX) would have been used to determine star formation rates, while the K band data was required for galaxy mass measurements for further analysis of the cluster. The proposal was for a total of 18.4 h. Unfortunately, the CFHT proposal was not accepted at the time. However, at the same time, a separate proposal had been submitted to the *Magellan* telescope by Dr. Vikhlinin and Dr. Mulchaey, for 2 nights of observing time, to obtain IMACS spectroscopy on the cluster and was accepted. Hence, we were able to obtain spectroscopic redshifts on a large sample of galaxies. The observations and analysis are described in the next two sections.

Chapter 3

Spectroscopic Study

The next stage of the analysis was to obtain spectroscopic observations on a large sample of galaxies at the *Magellan* Baade telescope, using the Inamori-Magellan Areal Camera and Spectrograph (IMACS). The observations and data reductions and the spectroscopic analysis of Abell 133 are detailed here. The first of the two observation runs was carried out by myself with the help of Dr. Mulchaey. All the mask generation, data reduction and obtaining redshifts was also done by myself.

3.1   Observations and data reduction

3.1.1   Optical data

The optical catalogue developed for the photometric analysis was used to target galaxies for further spectroscopy. In order to design the masks, galaxies were chosen from the r'-band catalogue with a magnitude of r'$\leq$ 22.5, resulting in $\sim$ 15000 possible targets (hereafter referred to as "catalogue" galaxies). Priorities were assigned to each of the targets as shown in Table 3.1, based on their magnitude and colour. Specifically, the targets were divided into two categories based on whether they were bluer or redder than (RS+0.1), where RS is the colour predicted at that magnitude by the red sequence fit to the optical data.

Table 3.1: Criteria for assigning priorities to the spectroscopy targets (lowest number corresponds to highest priority). For the last two categories, priorities were proportional to the difference between their colour and the RS, such that galaxies closer to the red sequence were assigned higher priorities, while still keeping these at lower priority than the other four categories.

Priority	Criteria
-1	r'< 16
0	$16 \leq$r'< 18
2	$18 \leq$r'< 20 and (g'-r')$\leq (RS + 0.1)$
3	$20 \leq$r'< 22.5 and (g'-r')$\leq (RS + 0.1)$
> 3	$18 \leq$r'< 20 and (g'-r')$> (RS + 0.1)$
> 5	$20 \leq$r'< 22.5 and (g'-r')$> (RS + 0.1)$

3.1.2 Mask design

For obtaining spectroscopy for the cluster, masks were designed using *maskgen*, the mask making software for IMACS. The masks, each with a radius of 13.5', were created at 11 positions covering most of the 1 sq. deg. field, with 2 masks at most positions. Figure 3.1 shows the locations of the masks. Of the masks designed, spectroscopy was obtained for 1 mask at each position and 1 additional mask at two positions in the south and south east as seen in the figure. Each mask had ∼120-175 slits; the individual details are given in Table 3.3.

3.1.3 Observations

Observations were obtained for 13 masks in total, of which 5 were done in the first observing run in September 2012 and 8 in the second observing run in October 2012. The conditions and exposure times for each of the masks are given in Table 3.2.

3.1.4 Data reduction

Data reduction on each of the masks was done using the COSMOS software package from the Carnegie Observatories Software Repository for IMACS, along with additional Python scripts in the CosmosPipeline. The first stage of the reduction produces separate 2-D spectra for each exposure of a mask. The second stage uses these preliminary 2-D spectra to create new "observation" files such as the ones produced by the *maskgen* programme,
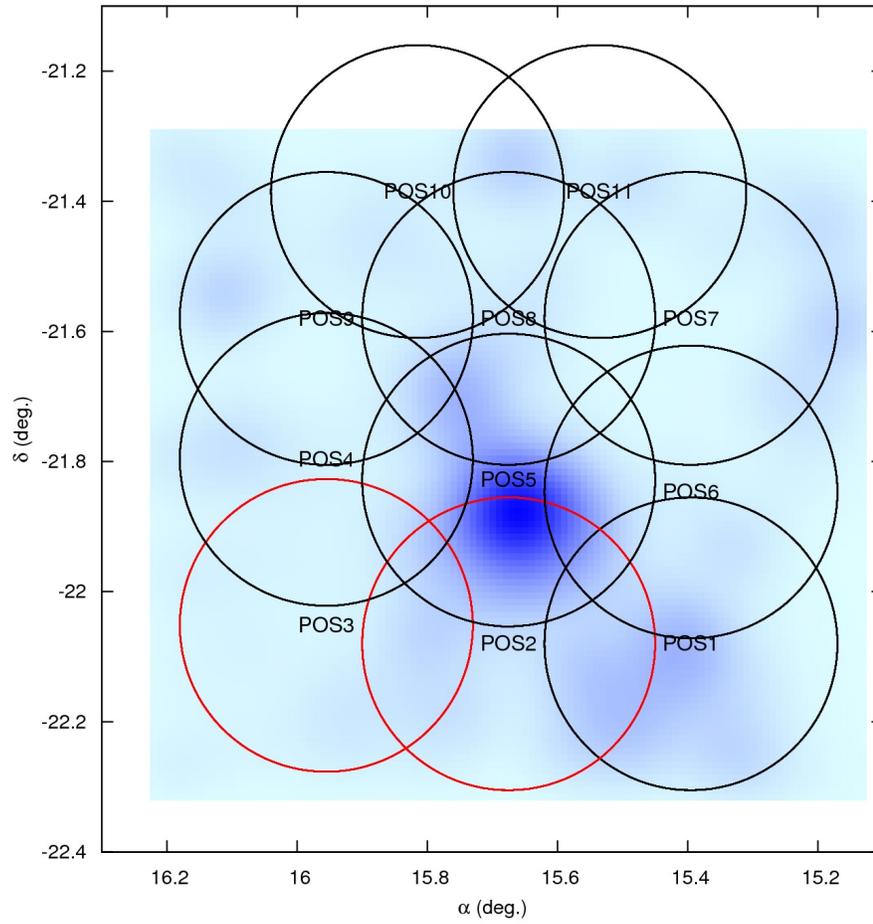
Figure 3.1: Locations of masks designed for spectroscopy, overlaid on the Gaussian smoothed intensity map. Observations were done on 1 mask at each position in black and 2 masks at each position in red.

Table 3.2: Summary of observations and conditions for each mask. The seeing was recorded at the start of every exposure for a mask, hence the final column shows the range of seeing observed across the different exposures. (* Conditions got cloudy towards the end of the observation)

Mask	UT Date	Exp. time	Seeing
POS1M1	17 Oct	2×1200s	-
POS2M1	17 Sep	2×900s	0.9"-1.1"
POS3M1	17 Sep	3×900s	0.8"-1.2"*
POS4M1	17 Oct	2×1200s	-
POS5M1	17 Sep	2×900s	1.2"-1.3"
POS6M1	17 Oct	3×1200s	1.2"-1.7"
POS7M1	18 Oct	2×1200s	0.7"-1.2"
POS8M1	17 Sep	2×1800s	2.2"
POS9M1	17 Sep	2×900s	1.3"-1.4"
POS10M1	18 Oct	2×1200s	0.8"
POS11M1	19 Oct	2×900s	0.9"
POS2M2	20 Oct	2×900s	0.8"
POS3M2	20 Oct	3×1200s	1.0"-1.2"

with better positions for each slit. The second stage then runs COSMOS again using these new positions for each exposure, to produce final, summed, 1-D and 2-D spectra using all exposures for a mask. A basic outline of the reduction procedure is as follows:

- Stage 1

  Align-mask Produces dewar offsets for finding apertures by using ~3 arc lines

  Map-spectra Predicts a mapping of wavelength and slit position onto the CCD plane

  Adjust-map Adjusts map by comparing predicted map and actual arc images

  Sflats Creates a spectroscopic flat field

  Biasflat Science images are bias and flat-field corrected

  Subsky Sky subtraction

  Extract-2dspec Extracts separate 2-D spectra for each exposure

- Stage 2

  2pass Produces new .SMF files for each exposure containing new positions for each slit using some of the brightest spectra from the results of Stage 1

COSMOS Each step of Stage 1 is run again separately on each exposure

Final extraction 1-D and 2-D spectra are extracted for each mask by summing all exposures

These reduced images were then flux calibrated using one of the reference stars by fitting a blackbody profile to it and applying corrections to all the spectra based on it. Two sets of redshifts were then calculated for each slit. First, the spectra were cross-correlated with 6 different galaxy template spectra in 5 different redshift ranges. The second set of redshifts were obtained by applying the additional step of searching for major emission lines. Then, 2 redshifts were selected for each spectrum; one corresponding to the best χ^2 cross-correlation fit, and the second corresponding to the best combination of important emission lines (i.e. Hα, Hβ, OII, OIII triplet, NII doublet and SII doublet) observed. The final redshift was then selected from the two by visual confirmation. The quality of the fit was assigned as follows:

Category 1 Very low noise, multiple absorption line matches (Ca H+K, G band, Mg, Na) for absorption spectra or multiple emission lines for emission spectra

Category 2 Low-to-medium noise, at least 2 absorption or emission lines

Category 3 Noisy spectra, roughly visible shape for absorption spectra or single emission line for emission spectra

Category 4 Very noisy spectra, difficult to confirm either type of redshift

Finally, heliocentric redshifts were obtained using the *rvcorrect* routine in IRAF. For the rest of the analysis, 'secure redshifts' refers to only Category 1 and 2 spectra. The details for each mask, i.e. the number of slits N_{slit} on the mask, the number of spectra obtained N_{spec} and the number of secure redshifts obtained N_{red} for each mask are given in Table 3.3. (Note: $N_{slit} > N_{spec}$ since some spectra fell on chip boundaries, or a valid mapping solution was not obtained for them). The table also gives a redshift success rate, which is defined as

$$f_z = \frac{N_{red}}{N_{spec}} \tag{3.1}$$

where N_{spec} is the number of spectra (of any quality) obtained and N_{red} is the number of secure redshifts.

Table 3.3: Summary of results for each mask. N_{slit} is the total number of slits on the mask, N_{spec} is the number of spectra (of any quality) obtained, N_{red} is the number of secure redshifts and f_z is the redshift success rate. Columns 2-5 include all galaxies while columns 6-9 are the same quantities when considering only galaxies with r'$\leq$ 19.5. (The results for POS3M1 and POS8M1 are lower than the others due to weather issues, the first due to cloudy conditions towards the end of the final exposure, and the second due to bad seeing.)

Mask	N_{slit}	N_{spec}	N_{red}	f_z	N'_{slit}	N'_{spec}	N'_{red}	f'_z
POS1M1	123	118	57	0.48	47	43	40	0.93
POS2M1	132	128	47	0.37	44	40	34	0.85
POS3M1	149	143	13	0.09	27	25	10	0.40
POS4M1	129	124	70	0.56	44	42	41	0.98
POS5M1	121	117	52	0.44	46	44	40	0.91
POS6M1	153	149	59	0.40	34	33	31	0.94
POS7M1	152	145	61	0.42	29	28	27	0.96
POS8M1	145	139	30	0.22	31	31	18	0.58
POS9M1	173	166	57	0.34	25	23	22	0.96
POS10M1	151	145	75	0.52	26	25	23	0.92
POS11M1	174	167	56	0.34	19	17	15	0.88
POS2M2	172	167	46	0.28	12	10	8	0.80
POS3M2	175	169	53	0.31	17	15	14	0.93

3.1.5   External data

Additional redshifts were obtained from the NOAO Fundamental Plane Survey (NFPS) associated with the Abell 133 cluster [Smith et al., 2004] and the 6 Degree Field Galaxy Survey (6dFGS) within 40 arcmin of the cluster centre [Jones et al., 2009], which together gave 74 galaxies with redshifts. 26 of these were galaxies we did not have secure redshifts for and hence, these were included in the set of secure redshifts. Figure 3.2 shows a comparison between the other 48 overlapping redshifts in terms of heliocentric velocities. It shows a mean Δv of 92 km/s and standard deviation of 104 km/s. If only the NFPS data are considered, the mean Δv is 75 km/s and the standard deviation is 35 km/s. All the secure velocities from spectroscopy were adjusted by 92 km/s in order to include the external data sets in the dynamical analysis. These corrected velocities and the corresponding redshifts are used in further calculations.

3.2   Analysis

3.2.1   Completeness analysis

Figures 3.3 and 3.5 show the completeness of the data in terms of magnitude and spatial distribution respectively and Figure 3.4 shows the redshift success rate as a function of magnitude. Completeness has been quantified using three different values.

Total sampling completeness

$$f_{tot} = \frac{N_{spec}}{N_{tot}} \tag{3.2}$$

Candidate sampling completeness

$$f_{candidate} = \frac{N_{spec}}{N_{candidate}} \tag{3.3}$$

Redshift success rate

$$f_z = \frac{N_{red}}{N_{spec}} \tag{3.4}$$

Here, N_{tot} is the total number of galaxies from the r'-catalogue, N_{spec} is the number of galaxies with observed spectra of any quality and N_{red} is the number of galaxies with
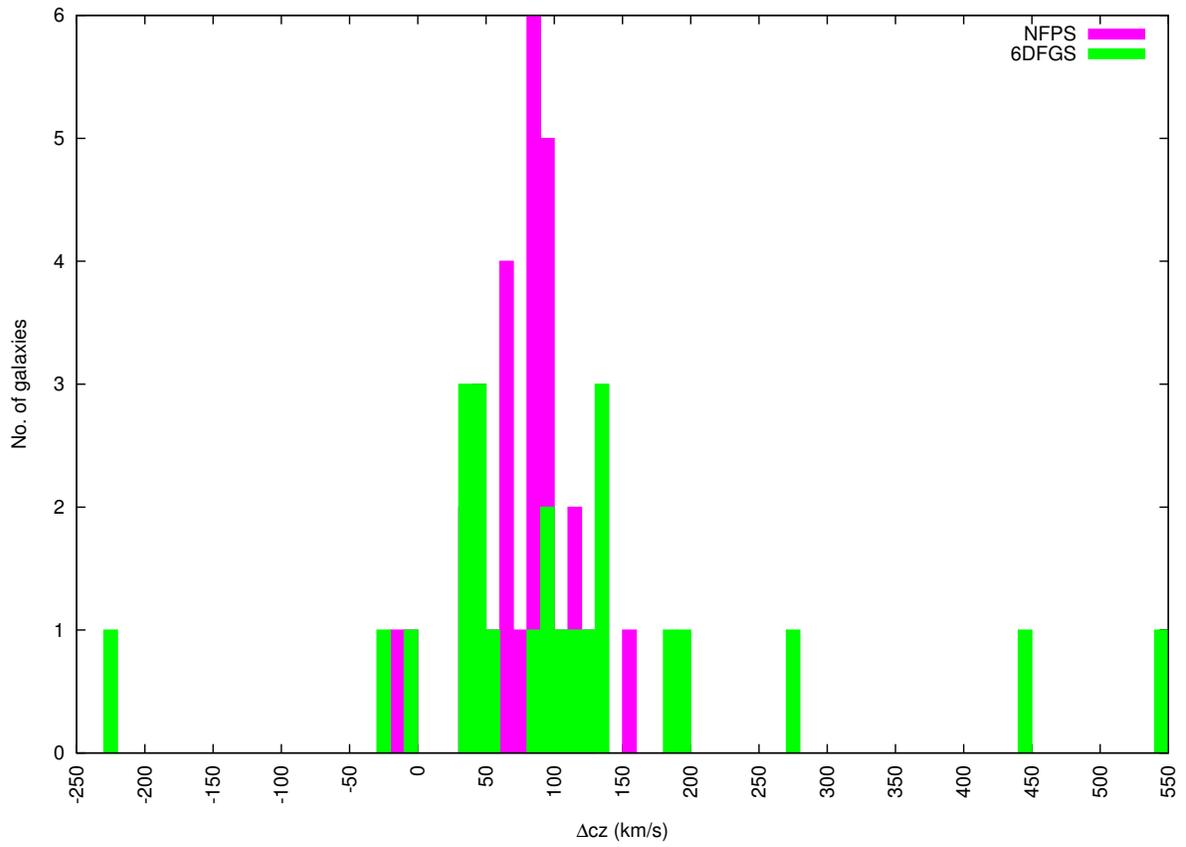
Figure 3.2: Comparison between heliocentric velocities from spectroscopy and from the external data sets, NFPS and 6dFGS.
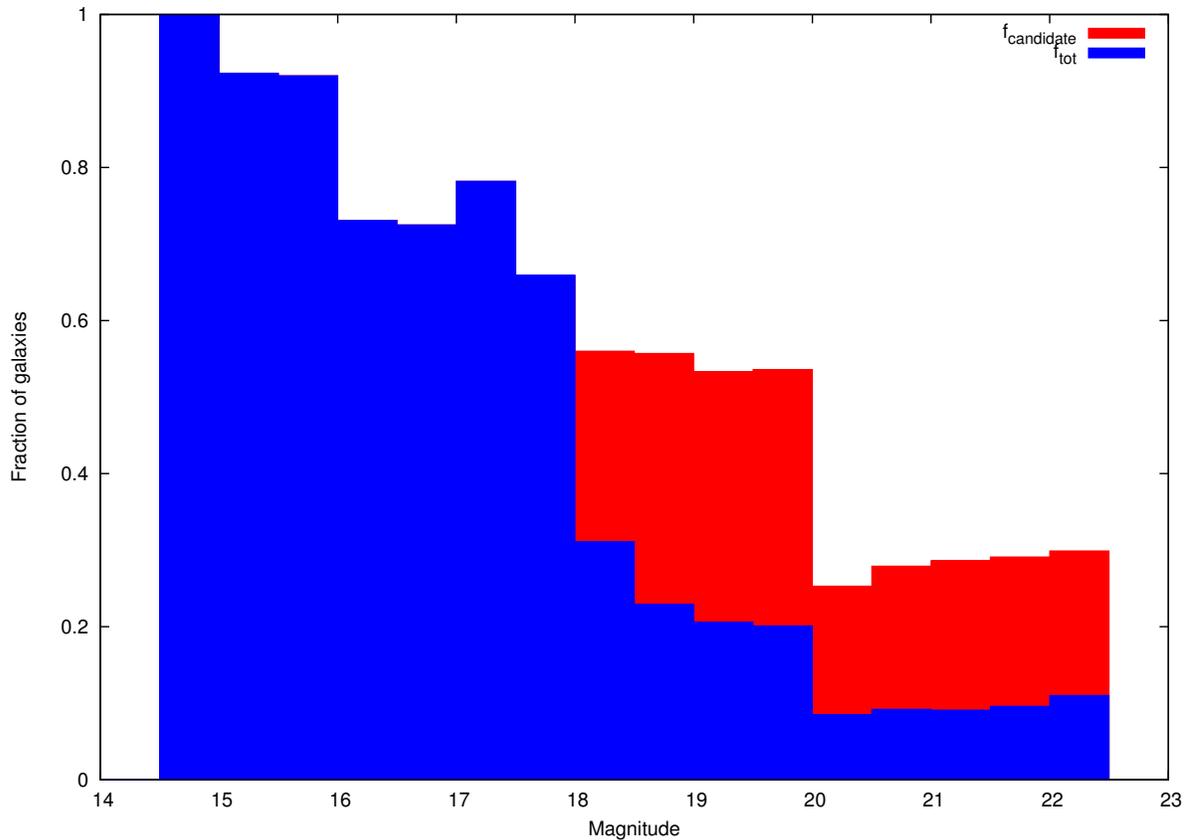
Figure 3.3: Completeness in magnitude showing fraction of catalogue galaxies that have spectra (blue) and fraction of candidate cluster members that have spectra (red).

secure redshifts. $N_{candidate}$ is the number of candidate cluster members, which are defined as all galaxies with r'$\leq$ 18 and all galaxies bluer than $(RS + 0.1)$ with 18 <r'$\leq$ 22.5. For the spatial completeness plots, an additional criterion of r'$\leq$ 19.5 was applied for all four counts.

The magnitude completeness shows that for r'$\leq$ 18, spectra were obtained for >60% of the catalogue galaxies and >80% of those spectra yielded secure redshifts. For 18 <r'$\leq$ 19.5, these numbers reduce to >20% and >70% respectively, although the completeness is >50% if only candidate cluster members are considered.
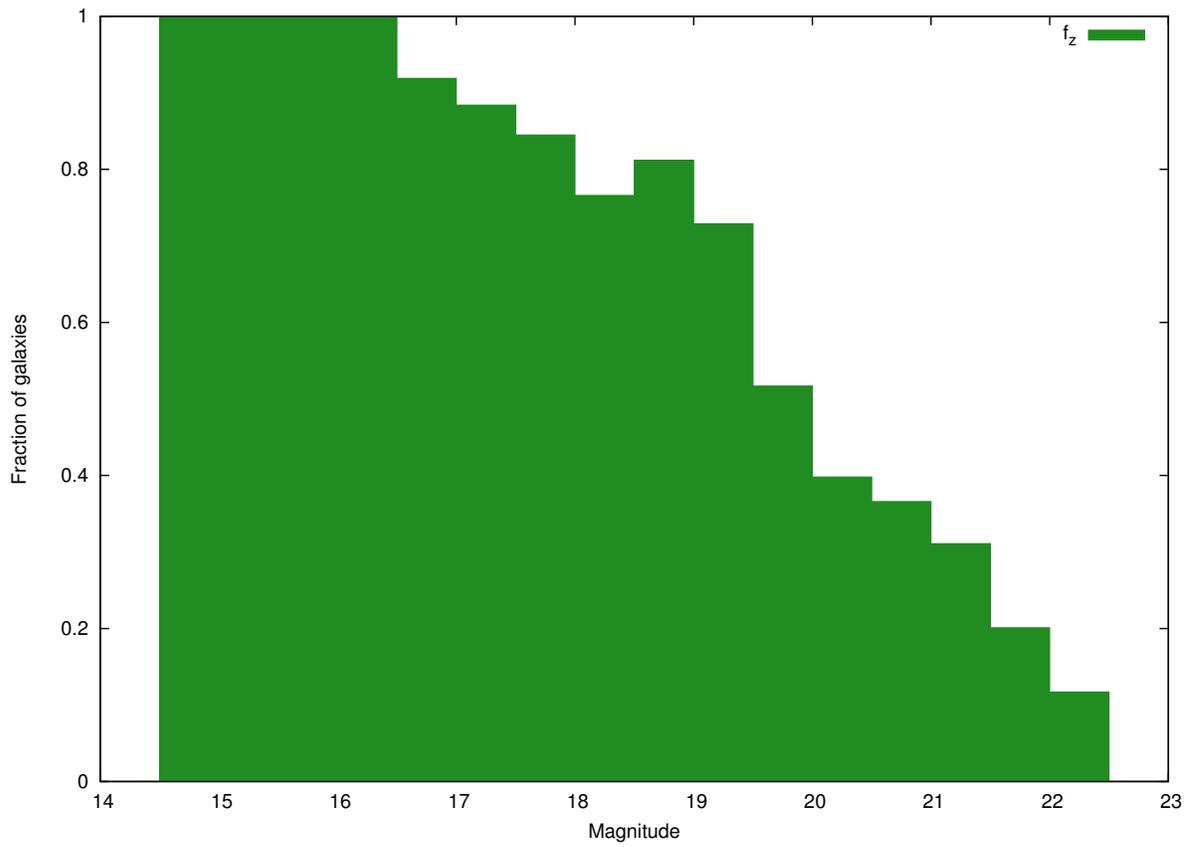
Figure 3.4: Fraction of spectra that yielded secure redshifts.
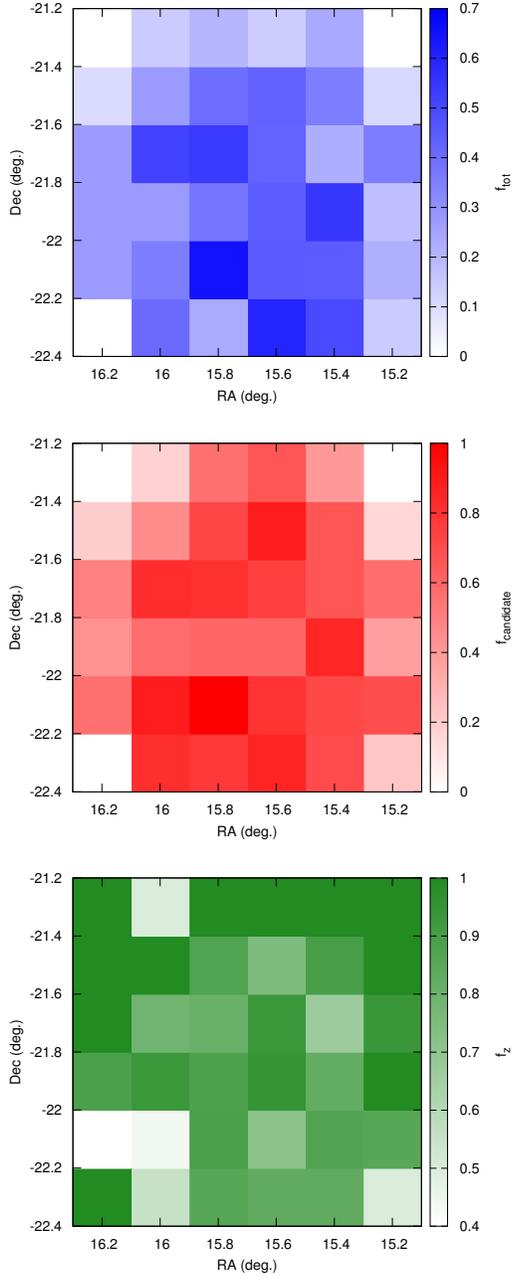
Figure 3.5: Spatial completeness of galaxies showing fraction of catalogue galaxies that have spectra (blue), fraction of candidate cluster members that have spectra (red) and fraction of spectra that yielded secure redshifts (green). Only galaxies with r'≤ 19.5 are considered here.

3.2.2 Cluster member selection

Figure 3.6 shows the redshift distribution and the distribution of velocities in the cluster frame. The weighted velocity dispersion was calculated using secure redshifts, with r'-magnitudes r'$\leq$ 19.5. The velocity dispersion was calculated as follows

$$\sigma^2 = \left(\sum_i w_i\right)^{-1} \sum_i w_i \Delta v_i^2 \tag{3.5}$$

with

$$\Delta v_i = \frac{c(z_i - \bar{z})}{(1 + \bar{z})} \tag{3.6}$$

where $\bar{z}$ is the weighted mean redshift, and the weights were calculated within 0.5 magnitude bins as

$$w_i = \left(\frac{N_{candidate}}{N_{red}}\right)_i = \left(\frac{1}{f_z f_{candidate}}\right)_i \tag{3.7}$$

This gave a velocity dispersion of 793 ± 43 km/s around a mean redshift of $\bar{z} = 0.0561 \pm 0.0002$ (the uncertainties were calculated using the Jackknife method as described earlier). The weighted and unweighted results were similar. Cluster objects were then selected if their velocity in the cluster frame was within $\pm 3\sigma$ around the mean velocity. Figure 3.7 also shows the positions of the secure galaxies in the field, giving the spatial distribution of the data.

The velocity-position plot in the reference frame of the cluster is shown in figure 3.8, where Δv is defined as in equation 3.6, and Δr is the radius relative to the BCG in Mpc. The figure also shows the velocity dispersion within 0.5 Mpc radial bins. The expected "trumpet-like" profile for a cluster is not clear from this plot due to the available sampling.

The weighted luminosity function for the cluster is shown in Figure 3.9. The luminosity for each galaxy was calculated as follows:

$$L_i = 10^{-0.4(M_i - M_{Sun})} \tag{3.8}$$

where M_i is the absolute magnitude of the galaxy and $M_{Sun} = 4.651$, that of the Sun in the r' band.

3.2.3 Red sequence analysis

The cluster red sequence was calculated using cluster galaxies within a range of $0.55 \leq$ (g'-r') ≤ 1.0 and with magnitudes r'$\leq$ 19.5 using a weighted least-squares fit. Galaxies
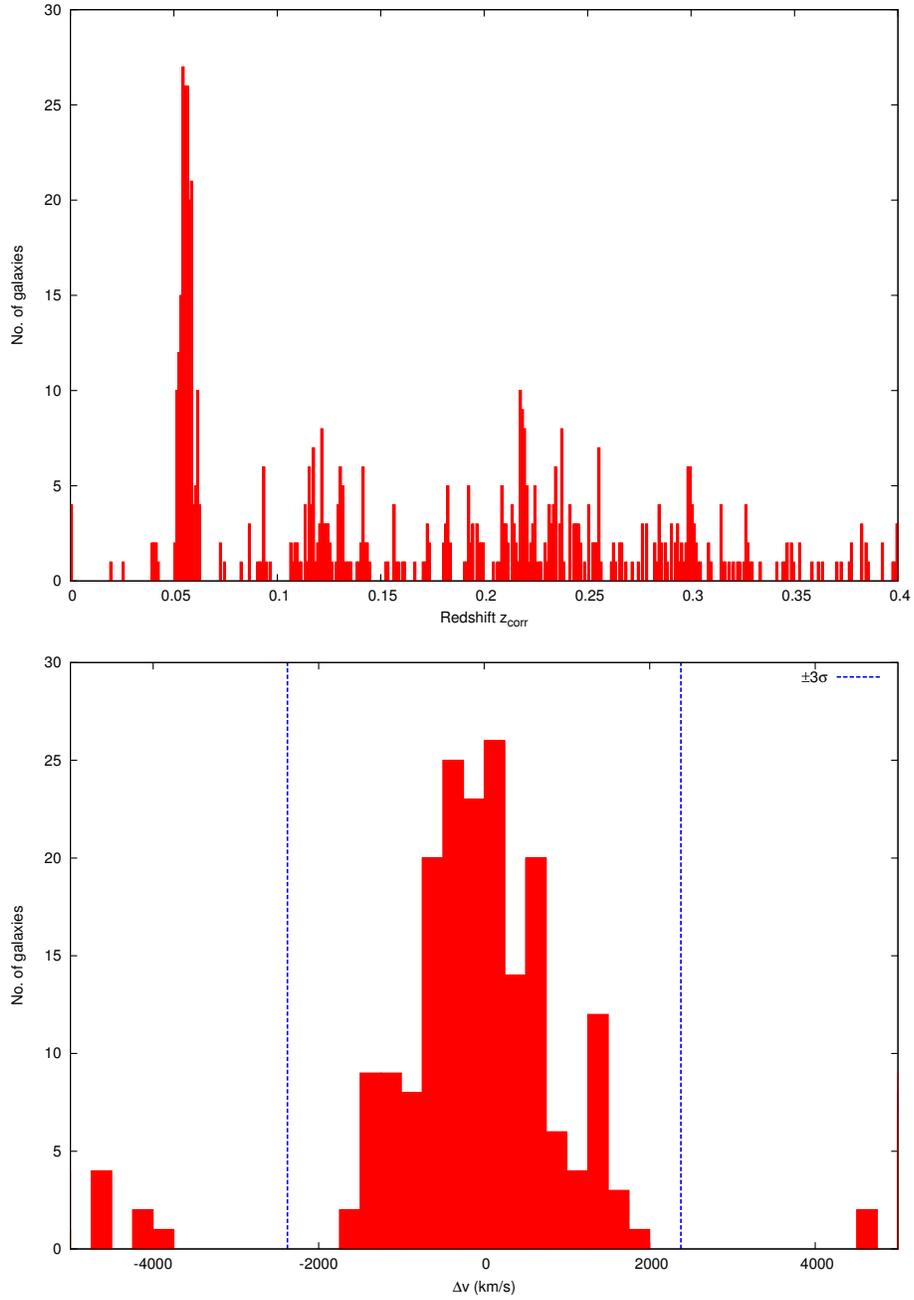
Figure 3.6: Redshift distribution of galaxies with secure spectra in 0.001 z bins (top) and velocity distribution in the cluster frame in 250 km/s bins (bottom). The dashed lines in the bottom plot show the 3σ limits from the velocity dispersion calculation.
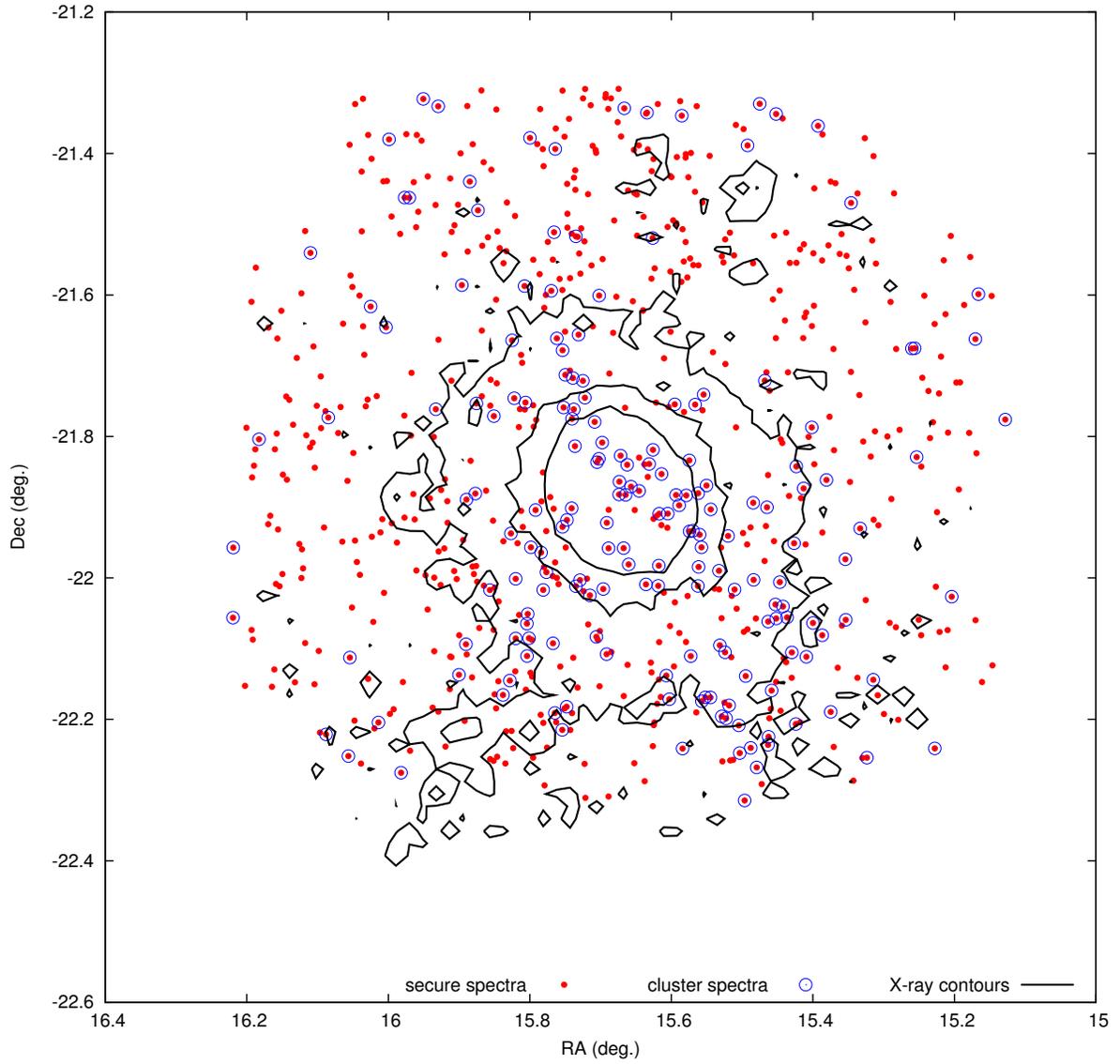
Figure 3.7: Positions of galaxies with secure spectra in the image (red), with cluster galaxies highlighted in blue. The overlaid black lines are logarithmic X-ray contours.
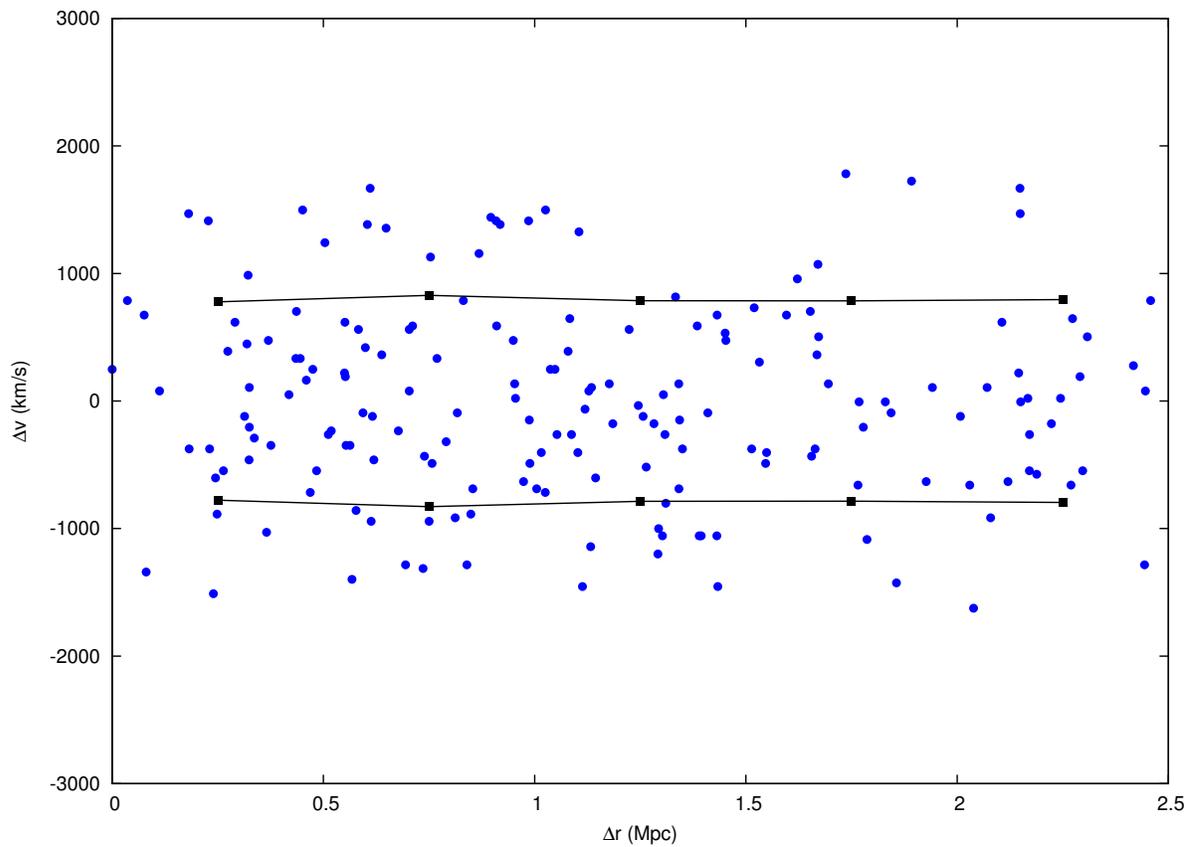
Figure 3.8: Plot of velocity vs. position in the reference frame of the cluster. Δr is w.r.t to the BCG. The range of the plot has been set to show galaxies most likely associated with the cluster. Solid lines show the velocity dispersion of these galaxies in 0.5 Mpc radial bins.
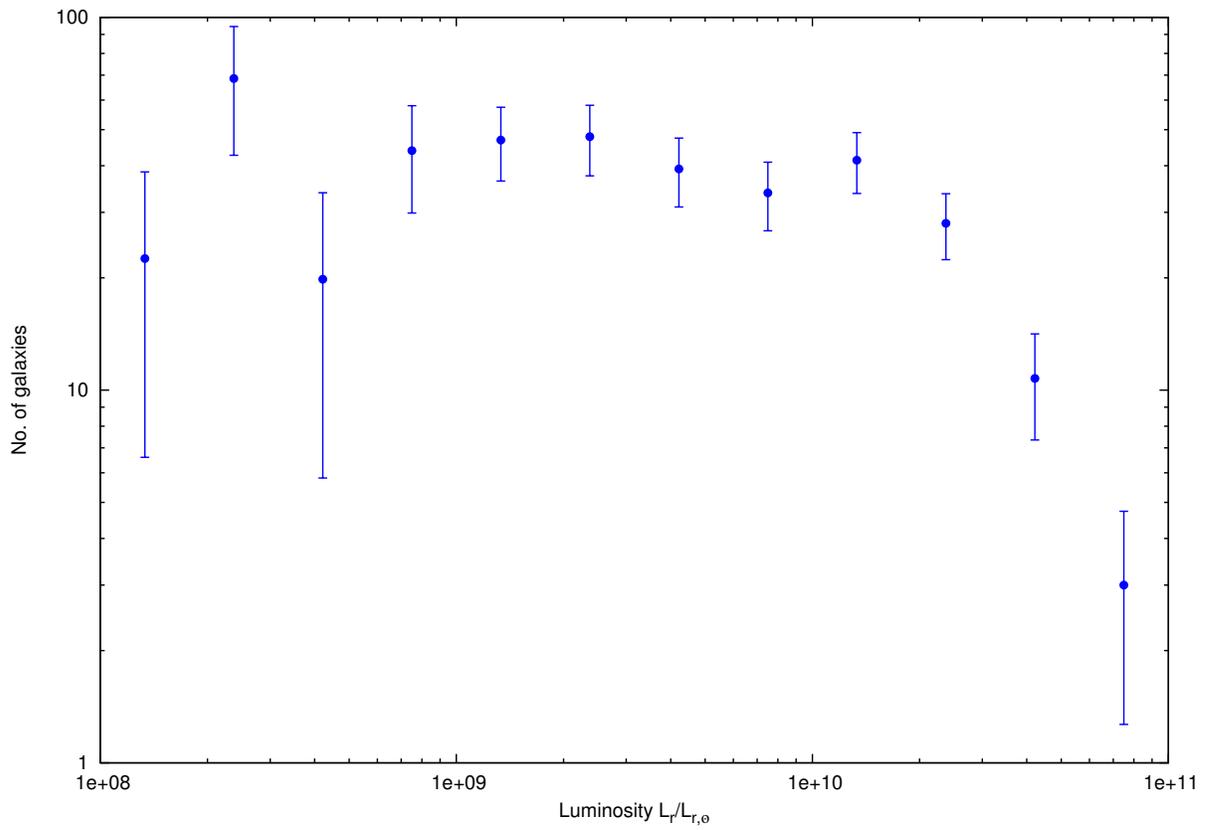
Figure 3.9: Weighted luminosity function for the cluster in the r'-band in 0.25 dex luminosity bins. Errors bars are Poisson errors.

were then selected to be part of the red sequence either if they were known cluster members from their redshifts, or if they were within 2σ of the red sequence and did not have a secure redshift, as shown in Figure 3.11. The known cluster members that are thus excluded are part of the blue cloud population of the cluster. This does not affect later results since further analysis in this chapter only uses known cluster members. Here, σ was defined as

$$\sigma^2_{RS} = \sum_i \left[(g' - r')_i - (mr'_i + b) \right]^2 \tag{3.9}$$

The red sequence fit is shown in Figure 3.10. Here the value of $\sigma_{RS} \simeq 0.036$ was calculated during the red-sequence fit; currently this is not done iteratively, since the galaxies used for the analysis are confirmed cluster members.

3.2.4 Dynamical analysis

The virial radius for the cluster was estimated using the projected two-point harmonic separation as follows, using the technique of Girardi et al. [1998].

$$\frac{1}{R_H} = \left(\sum_i^{N-1} \sum_{j>i}^{N} w_i w_j \right)^{-1} \sum_i^{N-1} \sum_{j>i}^{N} \frac{w_i w_j}{|\vec{R}_i - \vec{R}_j|} \tag{3.10}$$

The weights w_i and w_j for every pair of galaxies are the same as defined in equation 3.7, since this analysis only uses known cluster members (both red sequence and blue cloud populations), not the red sequence candidates. The 3-D virial radius and virial mass is given by

$$r_v = \frac{\pi R_H}{2} \tag{3.11}$$

$$M_v = \frac{3\pi}{2G} \sigma^2 R_H \tag{3.12}$$

This gave a value of $R_H = 0.92 \pm 0.02$ Mpc, $r_v = 1.44 \pm 0.03$ Mpc and $M_v = (5.9 \pm 0.8) \times 10^{14} M_\odot$.

To compare with earlier mass estimates, the M_{500} was also calculated as follows, using the virial theorem (assuming the velocity dispersion is roughly constant with radius).

$$M_{500} = 500 \rho_c \frac{4\pi R^3}{3} = \frac{500 H^2}{2G} R^3 \tag{3.13}$$

$$\gamma \frac{G M_{500}}{R_{500}} = \sigma^2 \tag{3.14}$$
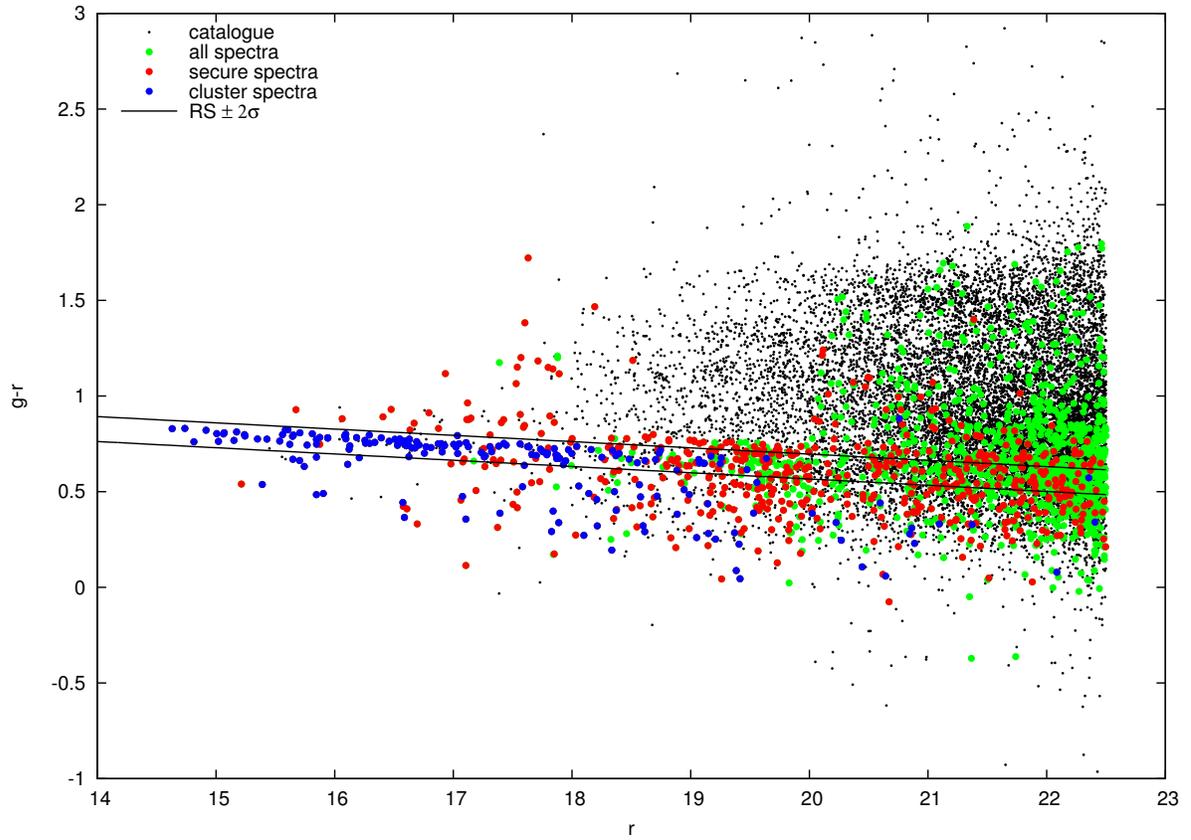
Figure 3.10: Colour magnitude diagram showing all catalogue galaxies (black), galaxies with spectra (green), those with secure spectra (red) and those identified to be cluster members (blue). The lines show 2σ limits of the red sequence.
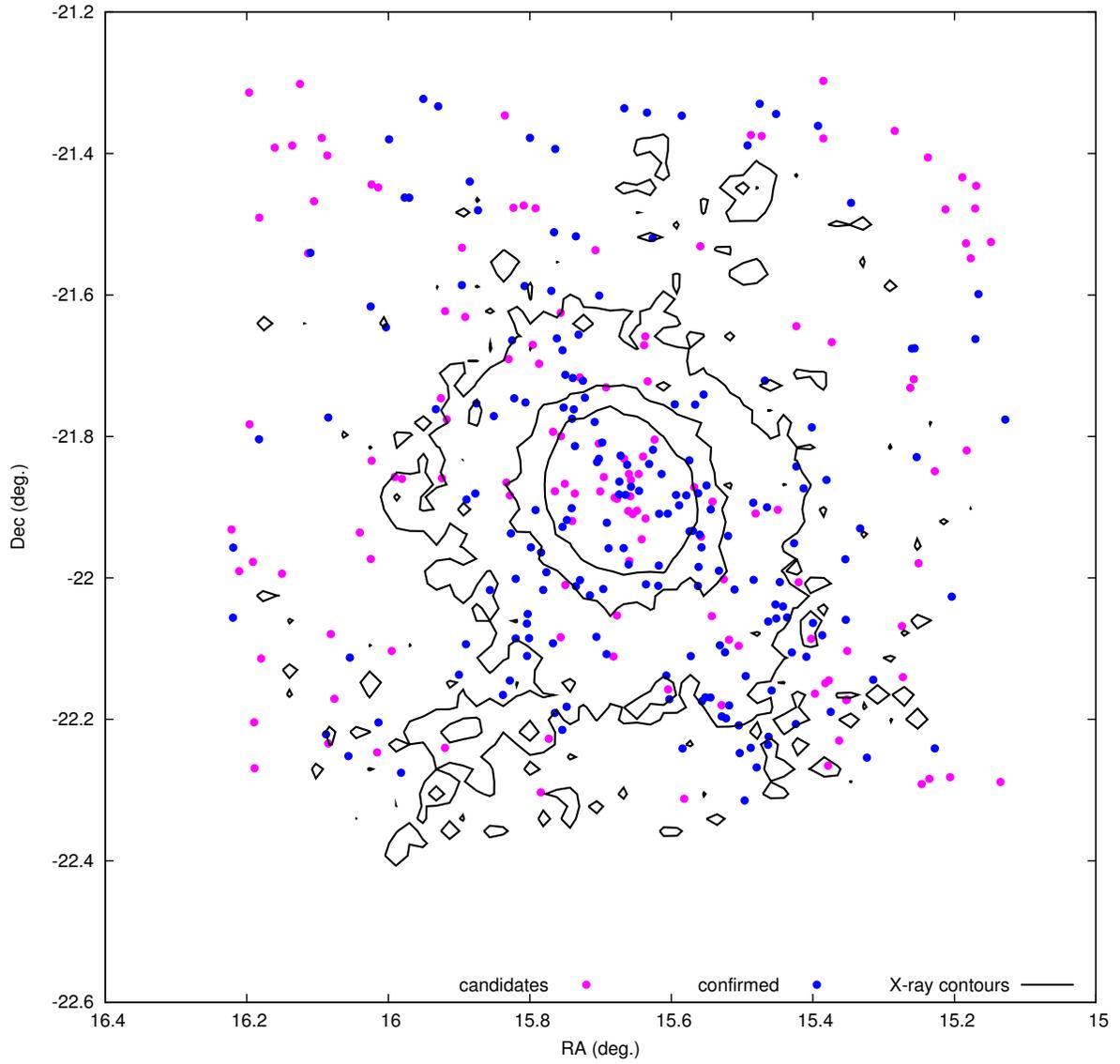
Figure 3.11: Positions of confirmed cluster members and red-sequence candidates in the field. The overlaid black lines are logarithmic X-ray contours.

This gives

$$R_{500} = \sqrt{\frac{2}{500\gamma H^2}}\sigma \tag{3.15}$$

$$M_{500} = \frac{1}{\gamma G}\sqrt{\frac{2}{500\gamma H^2}}\sigma^3 \tag{3.16}$$

The values calculated were $R_{500} = 1.21 \pm 0.07$ Mpc and $M_{500} = (5.3 \pm 0.9) \times 10^{14} M_\odot$ when using $\gamma = 1/3$ and $R_{500} = 0.99 \pm 0.05$ Mpc and $M_{500} = (2.9 \pm 0.5) \times 10^{14} M_\odot$ when using $\gamma = 1/2$.

Most studies use the $\gamma = 1/3$ value [e.g. Smith et al., 2004, Valentinuzzi et al., 2011]; however, this leads to a factor of ~ 2 difference between the mass calculated here and the mass quoted earlier, which were all derived from X-ray observations. The value of $\gamma = 1/2$, which yields results more consistent with the X-ray masses, is motivated by Lokas and Mamon [2001], who showed that for an NFW profile and assuming an isotropic velocity distribution, $\gamma = 0.56$ for $c = 5$ and $\gamma = 0.51$ for $c = 10$, where c is a concentration parameter. (For the galaxies in clusters, $c \sim 2 - 3$, whereas for the DM, $c \sim 10$ [Nagai and Kravtsov, 2005]). It should be noted that earlier studies such as Wu and Fang [1997], Richard et al. [2010] and Shan et al. [2010] have investigated this effect both numerically and observationally, comparing cluster mass estimates from lensing and X-ray data. They find that the X-ray estimate is lower than the lensing estimate by a factor of $\sim 1.5 - 3$, while the lensing estimate appears to agree with estimates of dynamical mass from galaxy velocity dispersion measurements. Therefore, the current results may be due to a similar effect and indicate that $\gamma = 1/3$ is the value to be used, although this needs to be further investigated.

Chapter 4

Comparison with X-ray overdensities

The final part of the analysis was to compare the clumps found in the optical analysis with the overdensities found in the X-ray image. A wavelet analysis of the X-ray image, performed by Dr. Vikhlinin, yielded over 80 substructures of varying sizes; several of these however were too small to contain more than a few galaxies and therefore, would be difficult to analyze. The X-ray detected substructures were in the form of ellipses; for the analysis of the optical image, these were converted to circular regions having the same area as the corresponding ellipse as follows:

$$R_c = \sqrt{A_c B_c} \tag{4.1}$$

where R_c is the radius, and A_c and B_c are the semi-major axes of the clumps, all in [deg.]. Only clumps with $R_c \geq 30$" were considered. Figure 4.1 shows the clumps that were thus selected. In order to determine if any of the clumps were associated with the cluster, galaxies were selected within R_c, $\sqrt{2}R_c$ and $2R_c$ of the clump centre, corresponding to regions with $1\times$, $2\times$ and $4\times$ the area of the X-ray emission. Figure 4.2 shows the extent of these regions on the optical image.

In Fig. 4.1, several of the clumps appear to be very compact, which may indicate the presence of point sources. However, comparing the image with Fig. 4.2, the location of the compact X-ray emission does not seem to align with a single galaxy which could be a point source. Therefore, it is likely that the X-ray emission in most of these clumps is due to extended structure. Also, in the previous chapter, several secure redshifts were obtained for galaxies in the background. However, as will be seen later, for most clumps we had redshifts for a very small number of galaxies, as the target of the spectroscopy had been galaxies bluer than the cluster red sequence. Hence, it was necessary to include the entire catalogue here in order to have a sufficient sample for this part of the analysis.
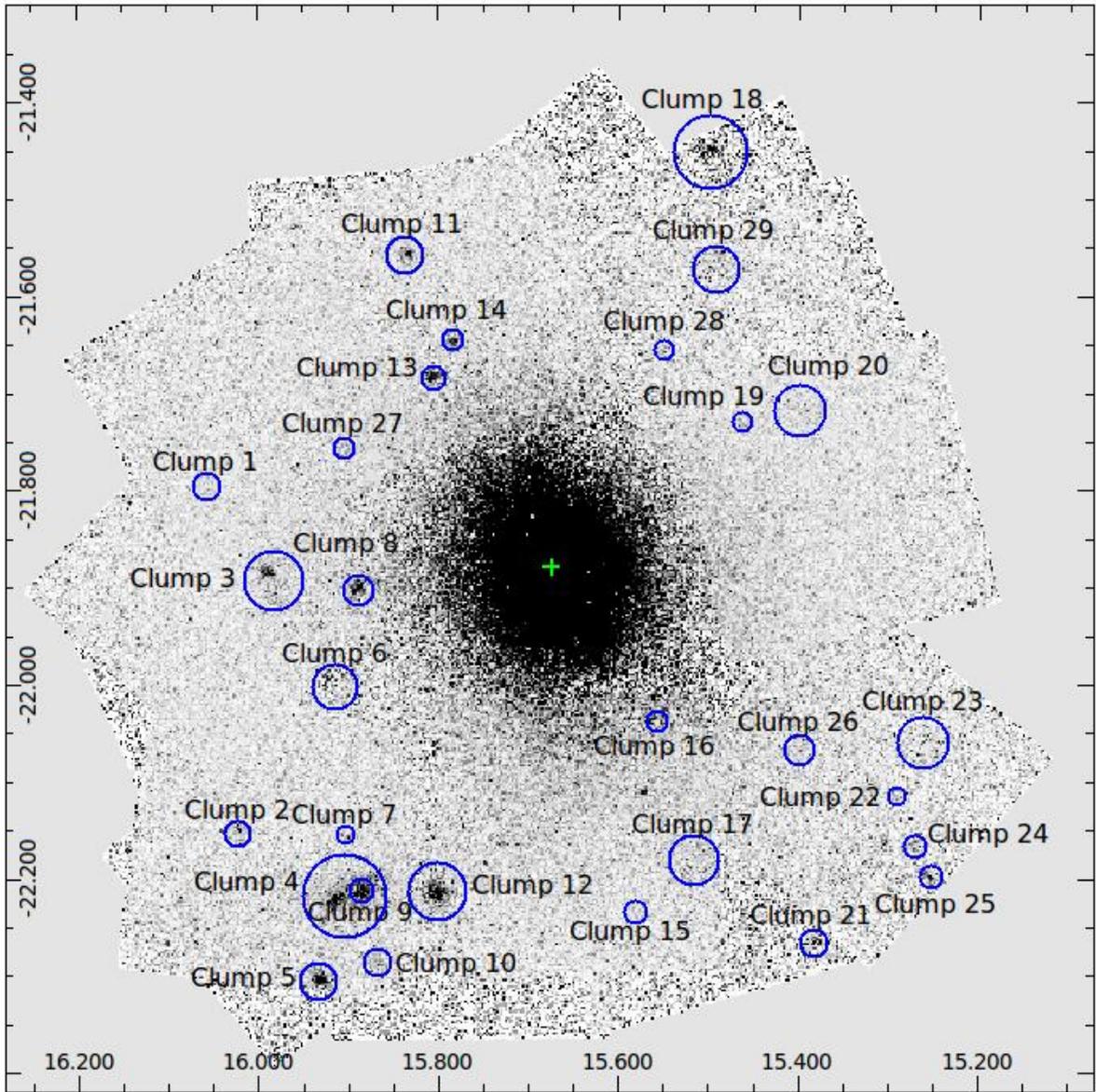
Figure 4.1: X-ray image of Abell 133 showing overdensities selected for gas clumping analysis as well as the X-ray centroid, shown in green.
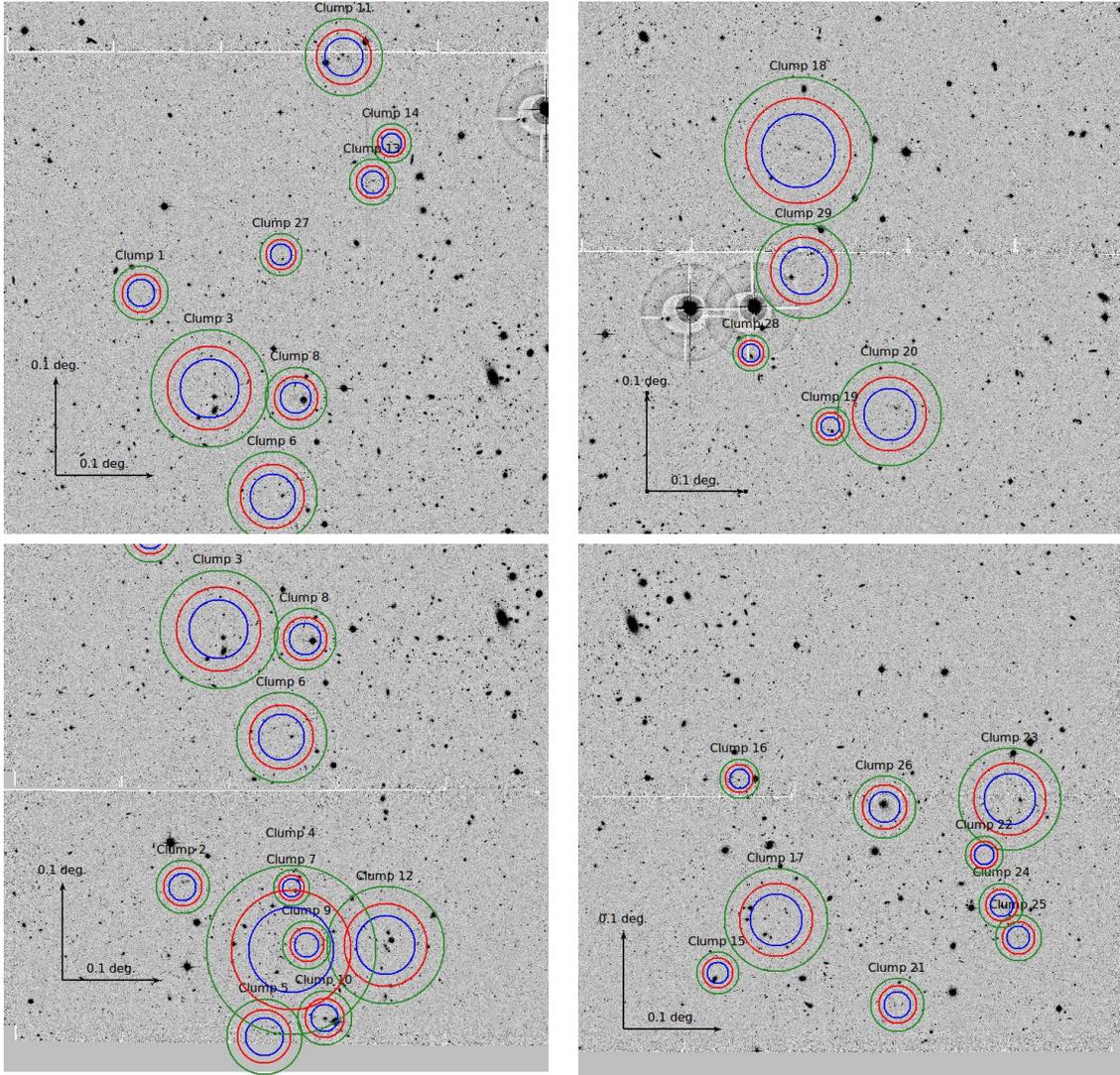
Figure 4.2: Optical images of the clumps showing the associated regions; the blue, red and green circles enclose 1×, 2× and 4× the area of the clump respectively, as determined from the X-ray image wavelet analysis.

4.1 Stacked clump statistics

Individually, not many of the clumps had possible red sequences immediately visible that could be used to determine whether they were associated with the cluster or not, as will be seen a little later. Therefore, before examining them individually, the data from all the clumps was stacked together to enhance the signal of any common red sequences. All galaxies within $2R_c$ were included. In cases where a galaxy was selected for more than one clump, it was taken to be associated with the clump that it was closest to. Figure 4.3 shows the stacked colour magnitude diagrams; the colours in the two figures represent absolute distance from the clump centre (top) in [deg.], and distance relative to the clump radius (bottom) that the galaxy is associated with, respectively. In both plots, 2 or 3 colour-magnitude relations may be seen (including the cluster itself), and this is more prominent in the bottom figure when focusing on galaxies closer to the clump centre. In order to isolate these possible colour-magnitude relations, galaxy counts and concentration profiles were measured in parallel colour-magnitude bands. For the rest of this analysis, only galaxies with r'$\leq$ 22 are considered, since the data for the fainter galaxies has too much scatter which would dominate any statistic to be calculated.

4.1.1 Significance of galaxy counts

To detect the presence of background red sequences, the galaxy counts were measured in colour-magnitude relation (CMR) bands parallel to the cluster red sequence. The data were separated into 10 bins of width 0.2 in colour, parallel to the cluster red sequence as follows:

$$\text{CMR bin} = floor \left[\frac{(\text{g}' - \text{r}') - (\text{RS} - 0.5)}{0.2} \right] \tag{4.2}$$

The band centred around the cluster red sequence is denoted as RS_0. All other bands are referred to by their median offset from the cluster red sequence. The values measured were the total number of galaxies in the stacked signal N_{all}, the number of galaxies in the cluster red sequence N_{RS}, the ratio of the two values $f_{RS} = N_{RS}/N_{all}$ and the number of galaxies in each bin N_i. Cluster red sequence galaxies were defined as those within 2σ of the cluster red sequence, where σ is the standard deviation measured during the red-sequence fitting (Note: this is the same as the RS_0, but with a smaller width). In order to determine the significance of these counts, the distribution of each of the values was measured by generating a random circular region for each of the clumps, at the same cluster-centric radius and with the same area, and carrying out the same measurements. The clumps were not excluded when generating these random regions and we ensured that every region
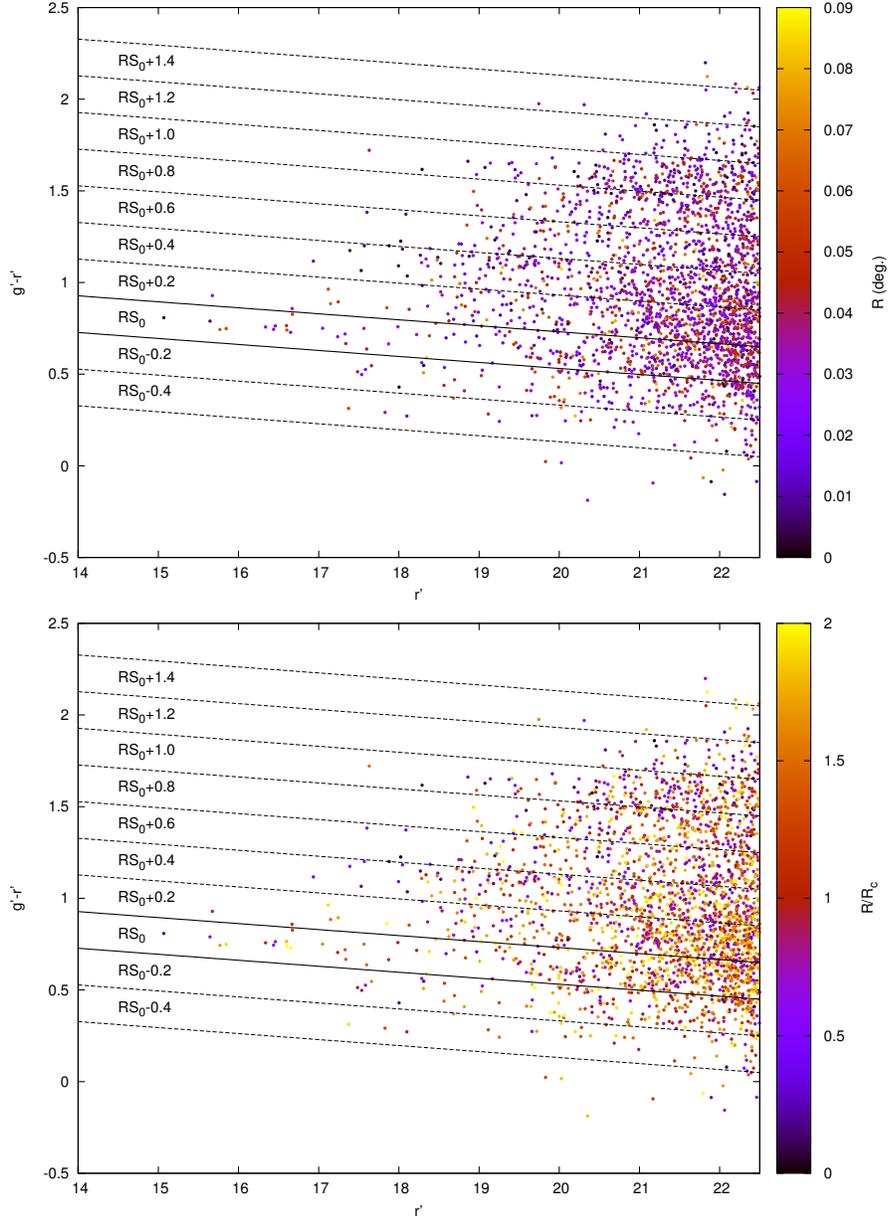
Figure 4.3: Stacked colour-magnitude plot of all the clumps. Top: colours represent the absolute distance of the galaxy from the clump centre in [deg.]. Bottom: colours represent the relative distance of the galaxy from the clump centre, scaled to the clumps radius. The plot also shows the colour-magnitude relation bands for the galaxy count and concentration analysis - solid lines contain the Abell 133 red sequence.

Table 4.1: Results of probability distribution analysis of the total galaxy count, cluster red sequence galaxy count, cluster red sequence fraction and galaxy counts in the CMR bins. N or f is the actual value measured for the clumps, $\overline{N}$ or $\overline{f}$ is the average value measured over 1000 iterations with randomly generated regions, σ is the standard deviation over the 1000 iterations and S is the significance of the actual measurement

Category	N or f	$\overline{N}$ or $\overline{f}$	σ	S
All galaxies	1636	1248	100.4	*3.9*
A133 RS galaxies	196	182	17.0	*0.8*
A133 RS fraction	0.12	0.15	0.01	*-2.3*
$RS_0 - 0.4$	27	32	5.9	*-0.9*
$RS_0 - 0.2$	132	120	10.9	*1.1*
RS_0	286	257	21.4	*1.3*
$RS_0 + 0.2$	309	252	24.1	*2.4*
$RS_0 + 0.4$	304	211	25.0	*3.7*
$RS_0 + 0.6$	174	138	18.3	*2.0*
$RS_0 + 0.8$	191	116	17.9	*4.2*
$RS_0 + 1.0$	160	92	16.5	*4.1*
$RS_0 + 1.2$	36	17	5.3	*3.7*
$RS_0 + 1.4$	4	2	1.2	*1.8*

generated fell entirely within the edges of the cluster images. This process was reiterated 1000 times to obtain a probability distribution for each count, along with a mean value and an RMS standard deviation.

The results are given in Table 4.1. The first three quantities indicate that while there is a significant excess of galaxies detected in the clumps, showing that there is clustering seen in at least some of the clumps, the number of cluster red sequence galaxies is consistent with the field, resulting in the red sequence fraction being significantly lower than in the field. This means that very few of the clumps are associated with the cluster. The statistics of the individual CMR bands show that while the galaxy counts are in excess of the field in most bands, the effect is more significant in bands much redder than the cluster red sequence.

4.1.2 Concentration

The above statistics were carried out on all galaxies within regions of four times the area of the clump, which did not show whether any excess galaxies are centrally concentrated. Hence, a similar analysis was carried out in four radial bins, considering both absolute and relative distances. However, the analysis based on absolute distances cannot provide much useful information since the distribution is affected by the intrinsic distribution of the clump sizes. Therefore, only the relative distances are considered here.

For each CMR bin, the projected density was measured in 4 radial bins of $r_i = R_i/R_c = [(0, 0.5), (0.5, 1), (1, 1.5), (1.5, 2)]$ as a galaxy count per unit area

$$\rho_{i,j} = \frac{N_{i,j}}{\pi \left(r_{j,out}^2 - r_{j,in}^2 \right)} \qquad i \equiv \text{CMR bin}, \qquad j \equiv \text{Radial bin} \qquad (4.3)$$

where $N_{i,j}$ is the galaxy count in the CMR and radial bin. The spatial distribution of the stacked clump galaxies in each CMR bin is shown in Figure 4.4 and the results of the probability distribution calculations are given in Table 4.2.

The figure shows that the galaxy distribution does seem to be centrally concentrated in the $(RS_0 + 0.4) - (RS_0 + 1.2)$ bands; this is also evident when comparing the concentration parameters $\rho_{i,j}$ across a single CMR band. Table 4.2 shows that the galaxy counts in the two outer radial bins are consistent with the expected value from the field. In the two inner bins, the galaxy counts in almost all bands are in excess of the field, especially in the innermost bin where they are $> 5\sigma$ detections in the $RS_0 + (0.4 - 1.2)$ bands. These results indicate that there is definitely some clustering seen in these 5 bands. The fact that these
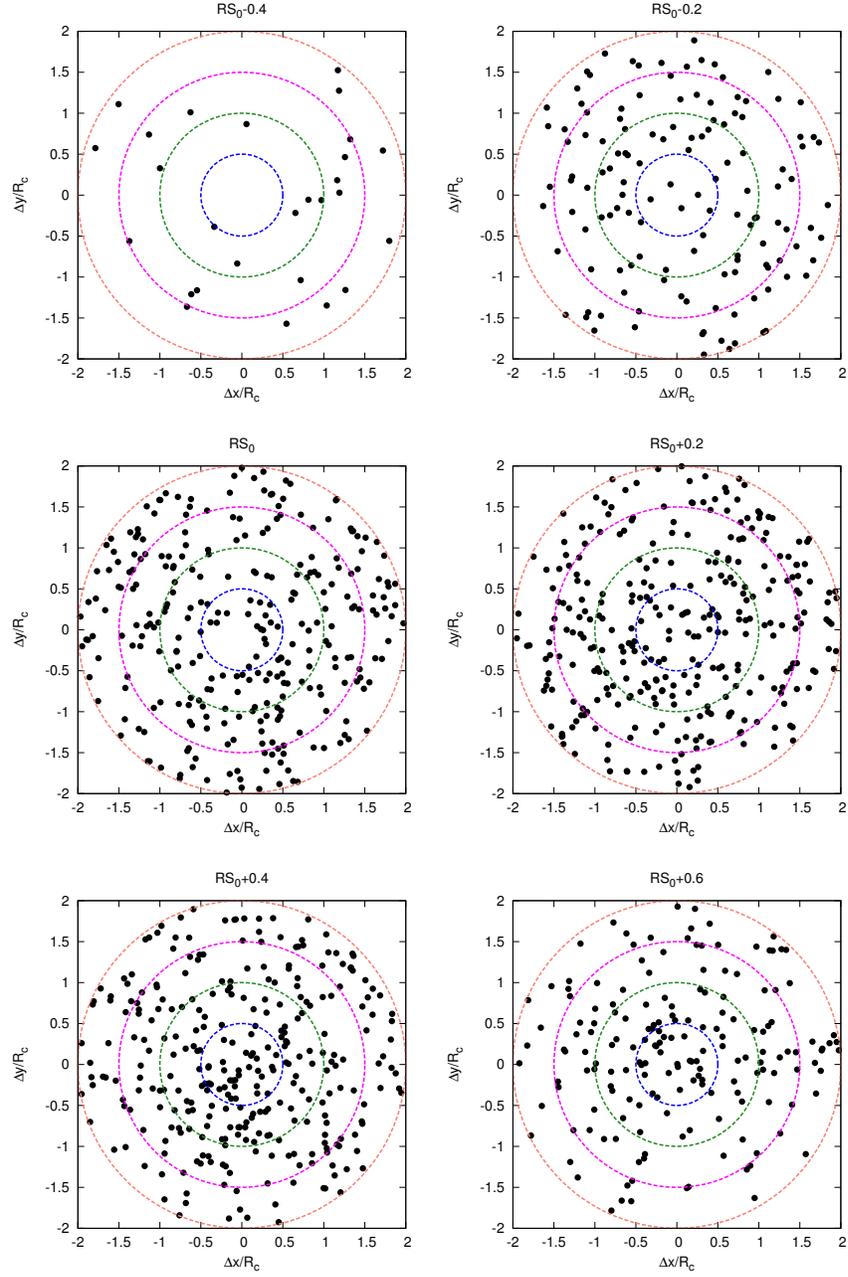
Figure 4.4: Spatial distribution of stacked clump galaxies in various CMR bins and four radial bins of $\rho = R/R_c = (0-0.5), (0.5-1), (1-1.5), (1.5-2)$
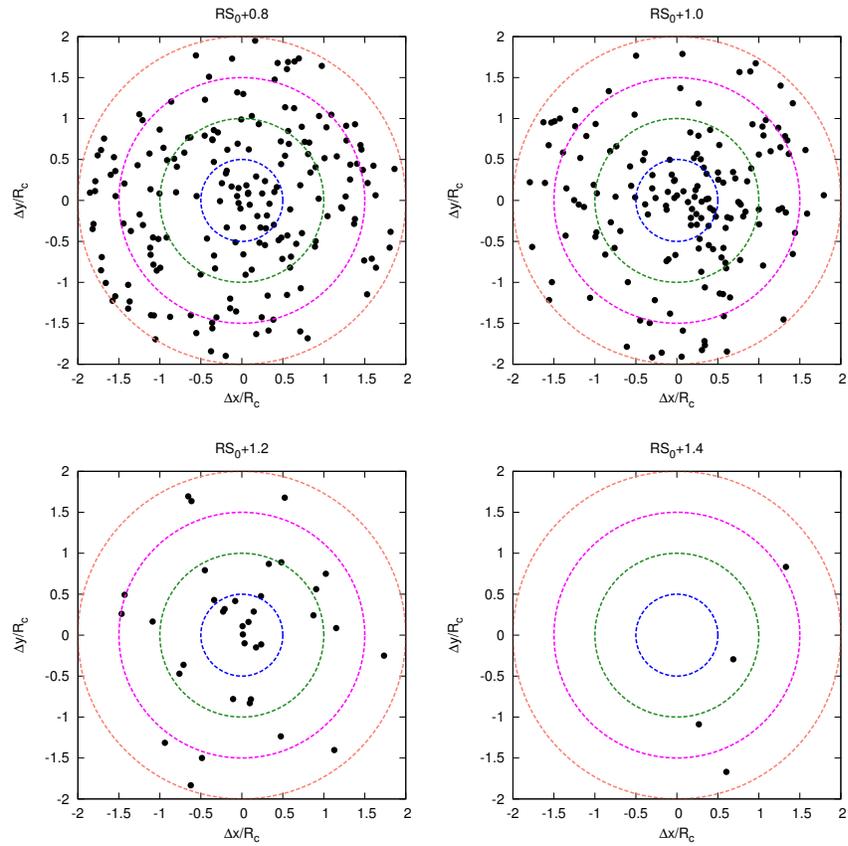
Figure 4.4: Spatial distribution of stacked clump galaxies in various CMR bins and four radial bins of $\rho = R/R_c = (0 - 0.5), (0.5 - 1), (1 - 1.5), (1.5 - 2)$

Table 4.2: Results of concentration analysis: $\rho_{i,j}$ is the galaxy count per unit area in the CMR band, $\overline{\rho_{i,j}}$ is the average galaxy count per unit area over a 1000 iterations, $\sigma_{i,j}$ is the standard deviation over the 1000 iterations and $S_{i,j}$ is the significance of the actual measurement

Band	$\rho_{i,1}$	$\overline{\rho_{i,1}}$	$\sigma_{i,1}$	$S_{i,1}$	$\rho_{i,2}$	$\overline{\rho_{i,2}}$	$\sigma_{i,2}$	$S_{i,2}$
$RS_0 - 0.4$	0.0	2.8	1.5	*-1.9*	2.5	2.6	2.6	*-0.0*
$RS_0 - 0.2$	6.4	10.3	2.8	*-1.4*	13.2	10.0	5.1	*0.6*
RS_0	22.9	21.9	4.3	*0.2*	24.2	21.1	7.6	*0.4*
$RS_0 + 0.2$	28.0	22.4	4.5	*1.2*	31.0	20.8	8.1	*1.3*
$RS_0 + 0.4$	44.6	18.8	4.5	*5.7*	33.1	17.8	7.9	*1.9*
$RS_0 + 0.6$	35.7	11.1	3.3	*7.4*	18.2	11.2	6.0	*1.2*
$RS_0 + 0.8$	33.1	9.9	3.2	*7.3*	18.2	9.6	6.4	*1.3*
$RS_0 + 1.0$	39.5	8.1	3.4	*9.3*	19.9	7.8	5.9	*2.0*
$RS_0 + 1.2$	12.7	1.5	1.3	*8.8*	4.2	1.5	2.2	*1.3*
$RS_0 + 1.4$	0.0	0.2	0.4	*-0.5*	0.4	0.1	0.5	*0.5*
Band	$\rho_{i,3}$	$\overline{\rho_{i,3}}$	$\sigma_{i,3}$	$S_{i,3}$	$\rho_{i,4}$	$\overline{\rho_{i,4}}$	$\sigma_{i,4}$	$S_{i,4}$
$RS_0 - 0.4$	2.8	2.6	3.3	*0.1*	1.8	2.4	3.8	*-0.2*
$RS_0 - 0.2$	11.7	9.6	6.3	*0.3*	9.1	9.2	7.4	*-0.0*
RS_0	22.2	20.5	10.4	*0.2*	22.6	20.0	12.2	*0.2*
$RS_0 + 0.2$	23.4	20.0	10.8	*0.3*	22.2	19.4	13.2	*0.2*
$RS_0 + 0.4$	21.6	16.9	10.6	*0.5*	19.3	16.1	12.9	*0.2*
$RS_0 + 0.6$	12.7	11.1	8.1	*0.2*	9.6	10.8	10.3	*-0.1*
$RS_0 + 0.8$	14.8	9.1	7.9	*0.7*	11.6	9.0	8.8	*0.3*
$RS_0 + 1.0$	10.2	7.3	7.2	*0.4*	7.6	7.0	8.2	*0.1*
$RS_0 + 1.2$	1.8	1.3	2.5	*0.2*	1.6	1.3	3.1	*0.1*
$RS_0 + 1.4$	0.3	0.2	0.7	*0.1*	0.4	0.1	0.9	*0.3*

results vary over the CMR bands indicates that there are a few different red-sequences in the stacked colour-magnitude plot. Crucially, there is no significant excess in the RS_0 band. Since the $(RS_0 + 0.4) - (RS_0 + 1.2)$ bands are redder than the cluster red sequence, the excess signal is mostly due to background systems.

4.2 Analysis of individual clumps

4.2.1 Dominant CMR band for individual clumps

To determine if it displays a prominent colour-magnitude relation, each of the clumps was analyzed in the same manner as the stacked signal, with one additional constraint added, which is the radius of the clump considered. While the statistics for the stacked set were calculated for galaxies within $2R_c$, for the individual clumps, two such sets of statistics were calculated, one within $1R_c$ and one within $2R_c$. This was to determine if the galaxies associated with the clumps were truly clustered and if any significant overdensity was due to galaxies close to the clump centre. Several clumps have a dominant CMR band in which their significance $S_i \geq 2$ in both cases, but especially so in the $1R_c$ case. The dominant CMR band for each clump is given in Tables 4.4 and 4.3 for the two cases, along with the galaxy count, average count, standard deviation, significance and the excess number of galaxies in the band. It should be noted that some clumps had different maximum significance bands in the two cases. Hence, the tables for the $1R_c$ and $2R_c$ cases also give the corresponding significance of the dominant band measured in the $2R_c$ and $1R_c$ case respectively. Several clumps have peaks in their significance profiles, which implies that the galaxies associated with them occupy a small redshift range. Figure 4.5 shows the trends in these significances for the $1R_c$ case only, since the significance trends are more pronounced here - in almost all cases, the value of the maximum significance increased when the radius was reduced.

There are three broad groups of clumps - those whose maximum significance CMR band remained the same in both cases, those whose bands did change but to an adjacent band, and those that had had very different dominant CMR bands in both cases. The three are discussed separately.

Category 1: For these clumps the maximum significance CMR band remained the same.

- For clumps 2, 3, 5, 7, 14, 20 and 24, the galaxy counts in their dominant bands were $> 2\sigma$ detections in both the $1R_c$ and $2R_c$ cases, and the significance
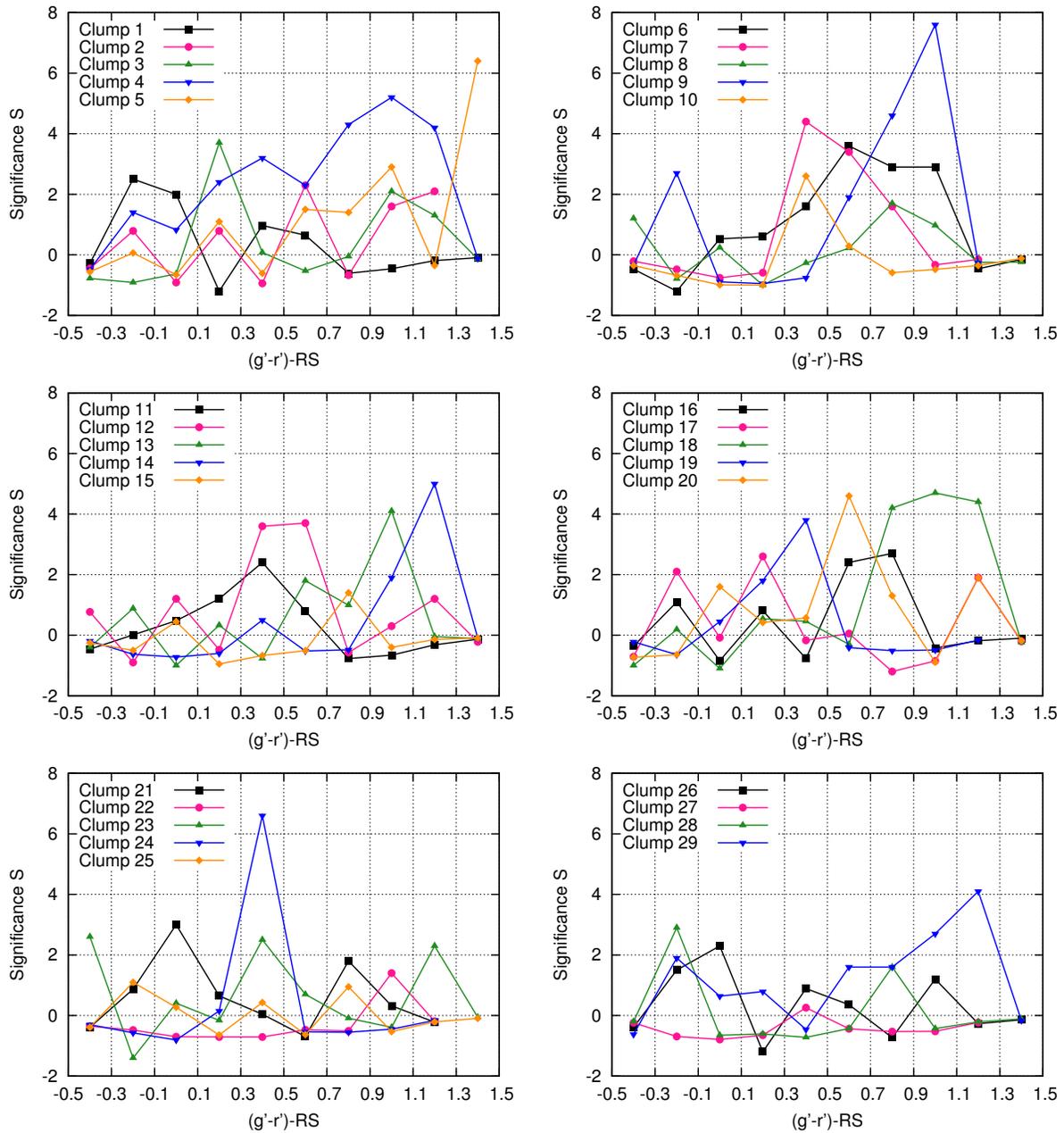
Figure 4.5: Significance of galaxy counts in each CMR bin for each individual clump, showing any prominent CMR bands.

Table 4.3: Properties for each clump in its maximum significance band Band_{max}, calculated within $2R_c$. N_{max}, $\overline{N}_{max}$ and σ_{max} are the galaxy count, average galaxy count and standard deviation in the band, S_{max} is the maximum significance and $N_{excess} = N_{max} - \overline{N}_{max}$ is the excess number of galaxies in the band. Significances greater than 2 are in bold. S_1 is the significance in the maximum significance CMR band within $1R_c$. The final column shows the significance S^* in the RS_0 band within $14.07 \leq \text{r'} \leq 18.07$.

Clump	Band_{max}	N_{max}	$\overline{N}_{max}$	σ_{max}	S_{max}	N_{excess}	S_1	S^*
1	$\text{RS}_0 + 0.0$	9	4.53	2.5	1.8	4	2.0	-0.5
2	$\text{RS}_0 + 0.6$	5	2.27	1.3	**2.1**	3	2.3	-0.6
3	$\text{RS}_0 + 0.2$	38	20.40	7.3	**2.4**	18	3.7	-0.3
4	$\text{RS}_0 + 0.4$	81	36.45	13.1	**3.4**	45	3.2	1.9
5	$\text{RS}_0 + 1.4$	1	0.04	0.2	**5.0**	1	6.4	-0.6
6	$\text{RS}_0 + 0.4$	22	10.94	4.1	**2.7**	11	1.6	-0.0
7	$\text{RS}_0 + 0.4$	6	1.79	1.9	**2.2**	4	4.4	-0.3
8	$\text{RS}_0 + 1.2$	2	0.45	0.8	1.9	2	-0.3	0.8
9	$\text{RS}_0 + 0.8$	12	1.84	1.9	**5.5**	10	4.6	-0.6
10	$\text{RS}_0 + 0.4$	9	4.01	2.5	2.0	5	2.6	-0.5
11	$\text{RS}_0 + 0.4$	10	7.78	4.6	0.5	2	2.4	-0.7
12	$\text{RS}_0 + 0.4$	45	17.95	9.1	**3.0**	27	3.6	2.3
13	$\text{RS}_0 + 0.8$	3	1.37	1.4	1.2	2	1.0	-0.5
14	$\text{RS}_0 + 1.2$	1	0.16	0.4	**2.2**	1	5.0	-0.4
15	$\text{RS}_0 + 0.8$	4	1.12	1.4	**2.1**	3	1.4	2.9
16	$\text{RS}_0 + 1.4$	1	0.06	0.2	**4.1**	1	-0.1	-0.5
17	$\text{RS}_0 + 0.2$	24	15.85	5.6	1.5	8	2.6	3.5
18	$\text{RS}_0 + 0.8$	45	17.96	9.0	**3.0**	27	4.2	-0.4
19	$\text{RS}_0 + 0.2$	6	1.82	1.6	**2.6**	4	1.8	-0.4
20	$\text{RS}_0 + 0.6$	23	8.69	4.1	**3.5**	14	4.6	-0.8
21	$\text{RS}_0 + 0.8$	7	2.37	2.1	**2.3**	5	1.8	-0.4
22	$\text{RS}_0 + 1.2$	1	0.24	0.6	1.2	1	-0.2	-0.4
23	$\text{RS}_0 - 0.4$	6	2.57	1.8	1.9	3	2.6	-1.1
24	$\text{RS}_0 + 0.4$	13	2.75	2.2	**4.6**	10	6.6	-0.3
25	$\text{RS}_0 - 0.2$	2	1.38	1.2	0.5	1	1.1	-0.4
26	$\text{RS}_0 + 1.2$	2	0.27	0.5	**3.5**	2	-0.3	1.1
27	$\text{RS}_0 + 1.4$	0	0.05	0.2	-0.2	-0	-	-0.5
28	$\text{RS}_0 + 1.2$	1	0.13	0.3	**2.5**	1	-0.2	-0.4
29	$\text{RS}_0 + 1.4$	2	0.13	0.4	**4.7**	2	-0.2	-0.7

Table 4.4: Properties for each clump in its maximum significance band Band_{max}, calculated within $1R_c$. S_2 is the significance in the maximum significance CMR band within $2R_c$. All other values are defined in the same was as Table 4.3 above.

Clump	Band_{max}	N_{max}	$\overline{N}_{max}$	σ_{max}	S_{max}	N_{excess}	S_2	S^*
1	$\text{RS}_0 - 0.2$	2	0.43	0.6	**2.5**	2	1.4	-0.2
2	$\text{RS}_0 + 0.6$	2	0.47	0.7	**2.3**	2	2.1	-0.2
3	$\text{RS}_0 + 0.2$	17	5.34	3.2	**3.7**	12	2.4	-0.6
4	$\text{RS}_0 + 1.0$	29	4.52	4.7	**5.2**	24	2.9	0.4
5	$\text{RS}_0 + 1.4$	1	0.02	0.2	**6.4**	1	5.0	-0.2
6	$\text{RS}_0 + 0.6$	8	1.87	1.7	**3.6**	6	1.5	-0.5
7	$\text{RS}_0 + 0.4$	4	0.46	0.8	**4.4**	4	2.2	-0.2
8	$\text{RS}_0 + 0.8$	2	0.56	0.8	1.7	1	0.7	-0.3
9	$\text{RS}_0 + 1.0$	5	0.28	0.6	**7.6**	5	5.4	-0.3
10	$\text{RS}_0 + 0.4$	4	1.02	1.1	**2.6**	3	2.0	-0.1
11	$\text{RS}_0 + 0.4$	7	2.08	2.1	**2.4**	5	0.5	-0.3
12	$\text{RS}_0 + 0.6$	10	2.54	2.0	**3.7**	7	1.8	-0.5
13	$\text{RS}_0 + 1.0$	3	0.40	0.6	**4.1**	3	1.0	-0.2
14	$\text{RS}_0 + 1.2$	1	0.04	0.2	**5.0**	1	2.2	-0.2
15	$\text{RS}_0 + 0.8$	1	0.24	0.6	1.4	1	2.1	5.5
16	$\text{RS}_0 + 0.8$	2	0.35	0.6	**2.7**	2	0.6	-0.2
17	$\text{RS}_0 + 0.2$	10	3.90	2.3	**2.6**	6	1.5	1.4
18	$\text{RS}_0 + 1.0$	22	3.85	3.8	**4.7**	18	2.5	-0.5
19	$\text{RS}_0 + 0.4$	4	0.60	0.9	**3.8**	3	2.2	-0.2
20	$\text{RS}_0 + 0.6$	10	1.99	1.7	**4.6**	8	3.5	-0.5
21	$\text{RS}_0 + 0.0$	4	1.05	1.0	**3.0**	3	1.9	-0.2
22	$\text{RS}_0 + 1.0$	1	0.23	0.5	1.4	1	0.6	-0.2
23	$\text{RS}_0 - 0.4$	3	0.78	0.8	**2.6**	2	1.9	-0.6
24	$\text{RS}_0 + 0.4$	7	0.69	1.0	**6.6**	6	4.6	-0.1
25	$\text{RS}_0 - 0.2$	1	0.34	0.6	1.1	1	0.5	-0.2
26	$\text{RS}_0 + 0.0$	4	1.33	1.2	**2.3**	3	1.7	2.7
27	$\text{RS}_0 + 0.4$	1	0.75	1.0	0.3	0	-0.8	-0.2
28	$\text{RS}_0 - 0.2$	2	0.36	0.6	**2.9**	2	0.5	-0.2
29	$\text{RS}_0 + 1.2$	2	0.16	0.5	**4.1**	2	2.2	-0.4

increased within the smaller clump radius. Hence, these do appear to have significant red sequences. Since these clumps had a high significance even within $2R_c$, any possible clustering of galaxies is likely to be an extended structure.

- For clumps 10, 11, 17 and 23, the galaxy counts were not significant within $2R_c$, but did become $> 2\sigma$ significant within the smaller clump radius. These are also probably actual red sequences, with a more centrally concentrated distribution of galaxies.

- Clump 25 had a $S_{max} < 2$ significance in both cases; hence, this clump does not have a significant red sequence.

- For clump 15, the maximum significance was $> 2\sigma$ in the $2R_c$ case, but not within the smaller radius. It is unlikely to have a significant red sequence.

Category 2: These clumps had a maximum significance in different bands for the two cases, but the two bands are adjacent, indicating that any possible red sequence lies near the boundary of the band.

- Clumps 9, 18, 19 and 29 had $> 2\sigma$ detections in the maximum significance band in both cases, and hence, these are most likely true red sequences. Again, since the significance was high within $2R_c$, the probably correspond to extended structures.

- For clumps 1, 6, 12 and 13, the galaxy counts were not significant within $2R_c$, but were $> 2\sigma$ significant within $1R_c$. Therefore, these are also likely to have a significant red sequence and be more centrally concentrated.

- Clump 22 did not have a significant number of galaxies in either case and therefore, does not have a red sequence.

Category 3: In these clumps, the dominant CMR band was quite different in the two cases, which would indicate a different galaxy population in the outer regions. For all of these, for the dominant band selected in the $2R_c$ case, the significance decreases within the smaller radius whereas for the dominant band selected in the $1R_c$ case, the significance increases within the smaller radius. Hence, the $1R_c$ is considered here.

- Clump 4 was $> 2\sigma$ significant in its maximum significance band in both cases, higher in the smaller radius. Hence, it most likely does have a significant red sequence and an extended structure.

- For clumps 16, 21, 26 and 28, the galaxy count in the maximum significance band was not significant within $2R_c$, but was $> 2\sigma$ significant within $1R_c$. These

66

are therefore probably actual red sequences, again more centrally concentrated. Of these, clumps 21 and 26 were $> 2\sigma$ significant in the RS_0 band and are likely to be associated with the cluster.

- Clumps 8 and 27 were not significant in either case and therefore, do not have any significant red sequence.

Since these statistics were calculated for r'$\leq$ 22, the significances tended to be dominated by fainter galaxies. In order to determine if a clump is associated with the cluster, one other significance, S^*, was calculated in the RS_0 band, within a magnitude limit of $14.07 \leq$ r' ≤ 18.07; a Schechter function fit to the galaxy luminosity function in the r' band has $M^* = -20.83 \pm 0.03$; hence, the magnitude limits corresponds to $m^* \pm 2.0$. In the $2R_c$ case, clumps 12, 15 and 17 had $S^* > 2$ and apart from clumps 4, 8 and 26, all other clumps had negative significances. In the $1R_c$ case, only clumps 15 and 26 still had $S^* > 2$, which means along with clumps 26, clump 15 may also be associated with the cluster.

All of the significances measured above are subject to a trials factor, i.e. the actual significance of a detection will be lower than that calculated within the band, since it is the result of searching through 10 different colour bands. Therefore, this effect should be taken into account when interpreting these results. Assuming a Poisson distribution for the galaxy counts in each band, the probability of finding $\geq N_{max}$ galaxies in the maximum significance band which has a mean galaxy count of $\overline{N}_{max}$ is measured as follows.

$$P = 1 - \sum_{i=0}^{N_{max}} \frac{e^{-\overline{N}_{max}} \overline{N}_{max}^i}{i!} \tag{4.4}$$

The probability of detecting a galaxy count of the same significance in any one or more of the 10 CMR bands is then given by

$$P^* = 1 - (1 - P)^{10} \tag{4.5}$$

These probabilities for each of the clumps are given in Table 4.5. For rough comparison, a 2σ and 3σ detection implies a probability of 2.3×10^{-2} and 1.3×10^{-3} respectively. As seen from the table, in general the actual probability of the detection is $\sim 10\times$ that measured within the single band. This effect is not as important for clumps 3, 4, 5, 6, 7, 9, 12, 13, 14, 18, 19, 20, 24 and 29, where the detections are still quite significant. However, for clumps 1, 2, 10, 11, 16, 17, 21, 23, 26, 28 which were $> 2\sigma$ detections in Table 4.4, the results are actually less significant.

Table 4.5: Effect of the trials factor on the measured significances within $1R_c$ for each clump. P is the probability of detecting N_{max} galaxies within the maximum significance band for each clump when the mean count in that band is $\overline{N}_{max}$. P^* is the probability of detecting a galaxy count of the same significance in any one or more of the 10 CMR bands.

Clump	P	P^*	Clump	P	P^*
1	9.6×10^{-3}	9.2×10^{-2}	16	5.5×10^{-3}	5.4×10^{-2}
2	1.2×10^{-2}	1.2×10^{-1}	17	2.3×10^{-3}	2.3×10^{-2}
3	1.3×10^{-5}	1.3×10^{-4}	18	2.9×10^{-11}	2.9×10^{-10}
4	0	2.1×10^{-14}	19	3.9×10^{-4}	3.9×10^{-3}
5	2.0×10^{-4}	2.0×10^{-3}	20	7.9×10^{-6}	7.9×10^{-5}
6	1.5×10^{-4}	1.5×10^{-3}	21	4.5×10^{-3}	4.4×10^{-2}
7	1.2×10^{-4}	1.2×10^{-3}	22	2.3×10^{-2}	2.1×10^{-1}
8	1.9×10^{-2}	1.8×10^{-1}	23	8.3×10^{-3}	8.0×10^{-2}
9	5.3×10^{-7}	5.3×10^{-6}	24	6.9×10^{-7}	6.9×10^{-6}
10	4.0×10^{-3}	3.9×10^{-2}	25	4.6×10^{-2}	3.8×10^{-1}
11	1.4×10^{-3}	1.4×10^{-2}	26	1.2×10^{-2}	1.1×10^{-1}
12	7.1×10^{-5}	7.1×10^{-4}	27	1.7×10^{-1}	8.5×10^{-1}
13	7.8×10^{-4}	7.7×10^{-3}	28	6.0×10^{-3}	5.8×10^{-2}
14	7.8×10^{-4}	7.8×10^{-3}	29	6.1×10^{-4}	6.0×10^{-3}
15	2.5×10^{-2}	2.2×10^{-1}			

4.2.2 Final results for individual clumps

Figure 4.6 shows the colour magnitude diagrams for each of the individual clumps, where the galaxies that have secure spectra as well as those spectroscopically identified as cluster members, are highlighted. Combining these with the statistics calculated above allows us to determine which clumps in the X-ray image correlate to a clustering of galaxies. The final results for the clumps are summarized here, along with any important details from the optical image.

Clumps 8, 15, 22, 25 and 27 These clumps did not have a $> 2\sigma$ significance in any CMR band and therefore, are not correlated with any stellar structure based on these statistics.

- Magnifying the optical image, a possible clustering is seen in clump 8, but only ~ 3 galaxies belong to its maximum significance band. (Note: there is also a fairly bright star present here, which may affect the results).
- Clump 15 has one bright galaxy offset from the centre, but this is not within its dominant CMR band.
- 2-3 galaxies are seen at the centre of clump 25.

Clumps 1, 2, 5, 14, 16, 28 and 29 These clumps did have a significance of $> 2\sigma$ in a CMR band, at least in the $1R_c$ case. For these clumps, the significance is a result of 1-2 galaxies in that band; these are not likely to be actual clusters.

- Clumps 28 and 29 are close to one of the bright stars in the north-west region of the image and hence, their results are more uncertain.

Clumps 6, 7, 9, 10, 11, 13, 19, 21, 23, 24 and 26 For these clumps, there was a dominant CMR band in which their significance is $> 2\sigma$ resulting from 3-9 galaxies. These are likely to be small groups.

- For clumps 6, 9 and 10, the galaxies within the dominant CMR band are not centrally concentrated on the image. (Note: clump 9 is part of clump 4).
- A centrally concentrated group of galaxies is evident on the optical image in clumps 11 and 24.
- Clump 26 is dominated by a single bright galaxy, which may be contributing to the X-ray luminosity, although it is not within the dominant CMR band.

Clumps 3, 4, 12, 17, 18 and 20 These clumps had maximum significance CMR bands with $> 2\sigma$ detections and these consisted of ≥ 10 galaxies in the band. These are most likely true clusters.

- Clumps 4, 12 and 18 had centrally concentrated distributions of the galaxies within their red sequence bands.

- For clumps 3, 17 and 20, several galaxies are detected in the dominant band, although they are not centrally concentrated.

As examples of the possible clusters or groups detected, images for clumps 4, 6, 9, 12, 18 and 20 are shown in Figure 4.7. Based on all the statistics, only 3 clumps are possibly associated with the cluster - clumps 15, 21, 26 - all in the south-eastern region of the image. As shown in the initial photometry analysis, there was significant overdensity in the Gaussian smoothed intensity map in the south-west region. Therefore these clumps may be contributing to this overdensity, although they may not account for all the excess luminosity in that region. The galaxies within $2R_c$ and within the RS_0 band for clumps 15, 21 and 26 yield luminosities of $2.4 \times 10^{10} M_{\odot}$, $0.2 \times 10^{10} M_{\odot}$ and $4.2 \times 10^{10} M_{\odot}$ respectively. The average intensity within $2R_c$ for these clumps from the galaxies within the RS_0 band can be used as a rough estimate of their contribution to the intensity map. The average intensity is 0.029, 0.002 and 0.051 Jy/deg^2; in comparison, the intensity in the region as seen in Fig. 2.5 is ~ 0.6 Jy/deg^2, although this is a very rough calculation. Hence, further studies are needed to explain the overdensities in both the optical and X-ray images that do not correlate with each other.

Figure 4.6: Colour-magnitude plots of galaxies within $1\times$ (blue), $2\times$ (red) and $4\times$ (green) the area of the clump. The black circles indicate galaxies with secure redshifts and the black squares represent secure cluster members. The dashed lines are 2σ limits on the cluster red-sequence.
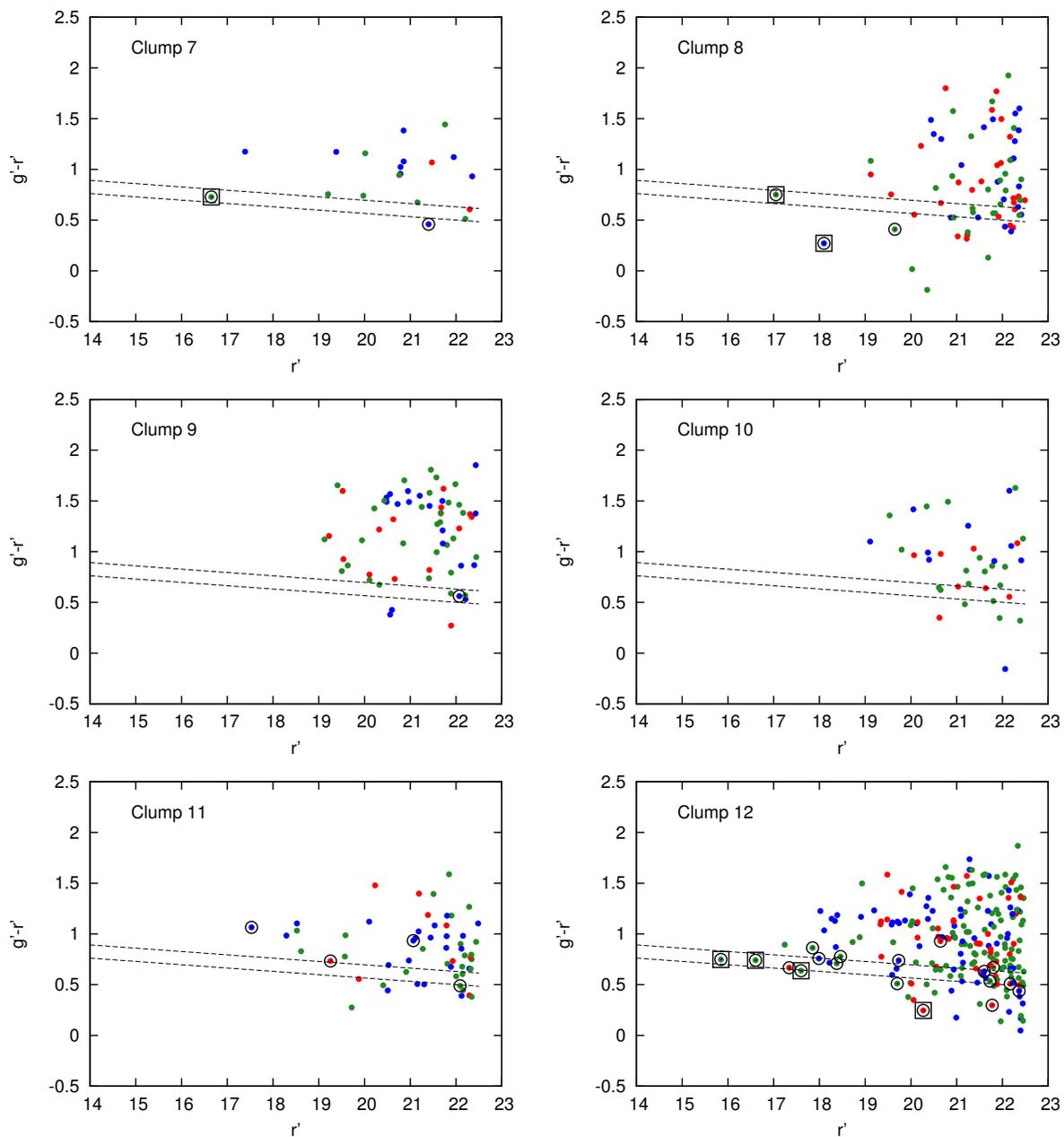
Figure 4.6: Colour-magnitude plots of galaxies within 1× (blue), 2× (red) and 4× (green) the area of the clump. The black circles indicate galaxies with secure redshifts and the black squares represent secure cluster members. The dashed lines are 2σ limits on the cluster red-sequence.
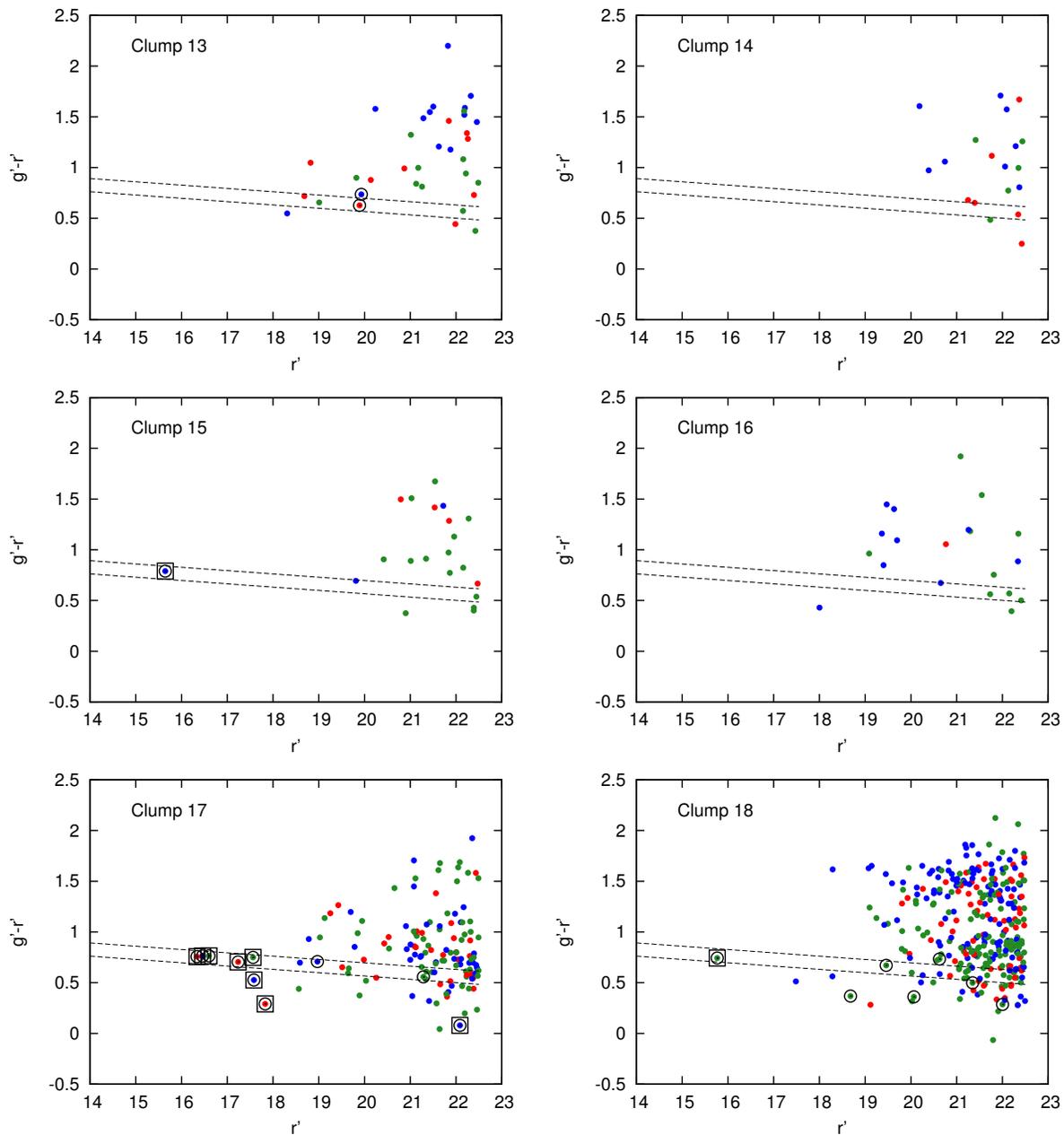
Figure 4.6: Colour-magnitude plots of galaxies within 1× (blue), 2× (red) and 3× (green) the area of the clump. The black circles indicate galaxies with secure redshifts and the black squares represent secure cluster members. The dashed lines are 2σ limits on the cluster red-sequence.

Figure 4.6: Colour-magnitude plots of galaxies within $1\times$ (blue), $2\times$ (red) and $4\times$ (green) the area of the clump. The black circles indicate galaxies with secure redshifts and the black squares represent secure cluster members. The dashed lines are 2σ limits on the cluster red-sequence.

Figure 4.6: Colour-magnitude plots of galaxies within 1× (blue), 2× (red) and 4× (green) the area of the clump. The black circles indicate galaxies with secure redshifts and the black squares represent secure cluster members. The dashed lines are 2σ limits on the cluster red-sequence.

Figure 4.7: Optical images of clumps 4, 18, 12, 20, 6 and 9, showing distribution of galaxies within $1\times$, $2\times$ and $4\times$ the area of the X-ray emission. (Note: clump 9 lies within clump 4, shown separately for clarity). The galaxies within the most significant CMR band in the $1R_c$ case are identified in black and galaxies within the Abell 133 red sequence are identified in purple.

Chapter 5

Conclusions

Recent studies in the outskirts of galaxy clusters have found flattened gas entropy profiles and values of f_{gas} that are higher than the baryon fraction derived from CMB data [e.g. Simionescu et al., 2011, Urban et al., 2011, Walker et al., 2012a, Ichikawa et al., 2013]. One explanation proposed for this effect is gas clumping at and beyond the virial radius of the cluster resulting in overestimates of the cluster density. Abell 133 was recently observed using a wide *Chandra* mosaic (of radius $\approx 30'$) with a $\sim$ 2Ms exposure time, thereby enabling the direct detection of any possible gas clumping. This also made it the perfect candidate for a parallel optical study to determine if the gas clumping is associated with substructure in the cluster. Here, we summarize our results of the optical analysis of Abell 133.

- The photometric analysis utilized the prominent red sequence in the cluster to select probable cluster members up to a depth of r'= 22.5, resulting in about 3200 galaxies selected within a colour magnitude band of width 0.2. The projected intensity profile was fit with the NFW model, along with three other double-power law models parametrized by $\eta = (1, 2, 3)$ the first two of which correspond to the Jaffe and Hernquist models respectively. The cluster intensity profile is fit well by the NFW and Hernquist profiles in the outer regions, although the inner region is better fit by the Jaffe profile.

- The red sequence galaxies were used to create a Gaussian smoothed intensity map of the cluster in $0.01° \times 0.01°$ bins; the Gaussian smoothing was done on $0.05°$ scales, corresponding to $\sim$ 200 kpc. Comparing this to the CFHTLS-W1 data, about 6 major overdensities in the cluster were detected, with significances ranging from $5 - 20\sigma$,

indicating that there is some substructure present in the cluster outskirts. However, these overdensities did not entirely match up with the X-ray image overdensities. The g'-r' red sequence selection did contain a large amount of background galaxies, which required either photometry in additional filters or spectroscopy in order to determine redshifts.

- Spectroscopy was obtained for 13 masks covering most of the optical image area, each with a radius of $13.5'$ and having $\sim 120-175$ slits. Data reduction was done using the COSMOS software package from the Carnegie Observatories Software Repository for IMACS, along with additional scripts in the CosmosPipeline. Redshifts were obtained from the reduced spectra both by using a cross-correlation fit to template spectra and searching for emission lines; the final redshift was selected by visual confirmation. External redshifts from the NFPS and 6dFGS were added to the sample of secure redshifts, resulting in about 690 galaxies with secure redshifts.

- The mean redshift and velocity dispersion in the cluster reference frame were measured, weighted by completeness in 0.5 dex magnitude bins; the cluster redshift was measured to be $\overline{z} = 0.0561 \pm 0.0002$ and the velocity dispersion was $\sigma = 743 \pm 43$ km/s. Cluster members were defined as those galaxies with velocities in the cluster reference frame within $\pm 3\sigma$. The cluster red sequence was also calculated using these confirmed cluster members, and candidate cluster members were selected within $\pm 2\sigma_{RS}$ of the red sequence, where σ_{RS} is the RMS scatter around the red sequence.

- The dynamical analysis of the cluster gave a 3D virial radius $r_v = 1.44 \pm 0.03$ Mpc and a virial mass $M_v = (5.9 \pm 0.8) \times 10^{14} M_\odot$. Based on an overdensity relative to the critical density of the Universe, the values measured were: $R_{500} = 1.21 \pm 0.07$ Mpc and $M_{500} = (5.3 \pm 0.9) \times 10^{14} M_\odot$ when using $\gamma = 1/3$ and $R_{500} = 0.99 \pm 0.05$ Mpc and $M_{500} = (2.9 \pm 0.5) \times 10^{14} M_\odot$ when using $\gamma = 1/2$. Several studies use $\gamma = 1/3$ [e.g. Smith et al., 2004, Valentinuzzi et al., 2011] which corresponds to an isotropic velocity distribution; however, the mass calculated using this value of γ is larger by a factor of ~ 2 than previous values measured using X-ray data. For galaxy clusters, the velocity distribution is more radial, which indicates $\gamma \sim 1/2$ is the more accurate value to use [e.g. Lokas and Mamon, 2001].

- Candidate gas clumps were detected as overdensities in the X-ray image. Of the clumps detected, those with an equivalent radius of $R_c \geq 30$" were considered for comparison with the optical data. Galaxies were selected within $1\times$, $2\times$ and $4\times$ the area of the X-ray emission. The signal from all the clumps was stacked to obtain

a net clumping signal. A probability analysis was then carried out within parallel colour-magnitude bands. It showed that the stacked signal did have significant colour-magnitude relations redder than the cluster red sequence. An analysis of the concentration of the stacked signal showed that these significant colour-magnitude relations were also centrally concentrated. The two sets of statistics indicated that there are possible background clusters associated with at least some of the X-ray clumps.

- Each individual clump was examined using the same procedure, measuring the significance of its galaxy counts within parallel colour-magnitude bands. The statistics were done within $2R_c$ and $1R_c$ and the most significant band in each case was taken to be the possible red sequence for the clump. Several clumps had a clear peak in their significance profiles across the colour-magnitude bands, indicating they had a narrow redshift range and were possibly clusters. Of the 29 clumps analyzed, 5 did not have any CMR bands with a $> 2\sigma$ significance and hence, are not associated with any stellar structure. Of the clumps that did have $> 2\sigma$ detections in their maximum significance bands, 7 clumps had only 1-2 galaxies in the band and are not likely to be groups or clusters; 11 clumps had 3-9 galaxies and may be small groups, and 6 clumps had ≥ 10 galaxies and are likely to be clusters. In particular, 3 large clumps had centrally concentrated distributions of galaxies in their red sequence band, indicating that they are true clusters.

- Finally, most of the clumps that did have a significant red sequence associated with them appeared to be background systems as their maximum significance CMR band was redder than the cluster red sequence. Only 2-3 of the clumps appeared to be associated with Abell 133. These three candidate clumps were all in the south-west region of the image where there was a large overdensity in the Gaussian smoothed intensity map of the cluster, and had radii ranging from 38.3" to 56.4".

These results show that most of the overdensities in the X-ray image appear to be background systems, whether they consist of 1-2 galaxies, small groups or clusters. This indicates that the stellar structure of the cluster is actually quite smooth. Once the background clusters are accounted for, the clumping factor is expected to be quite low (although this analysis is yet to be done). However, this result may not be consistent with the results found by Nagai and Lau [2011], who used numerical simulations including cooling and star formation, and found significant clumping factors around r_{200}. The most important issue is the physical scale of the clumps in both the X-ray observations as well as the simulations, which requires additional studies. Further quantitative analysis is required

to measure the scale of this effect and if it is significant, why the cluster has a smoother density distribution than predicted.

Also, a large number of the clumps did have a significant associated red sequence. Therefore, further studies are needed to determine if their abundance is consistent with what is observed in the field. The X-ray analysis is currently in progress and in the future, will provide X-ray fluxes for the clumps; these can then be compared with published $\mathrm{d}\log N/\mathrm{d}\log S$ profiles. Further investigations are required to examine if there is any correlation between the X-ray fluxes and the clustering found here. Finally, the luminosities and stellar masses of the clumps based on the optical imaging need to be compared with the X-ray observations to obtain the mass and other properties of both the background systems as well as the few clumps associated with the cluster.

References

N. Afshordi, Y.-T. Lin, D. Nagai, and A. J. R. Sanderson. Missing thermal energy of the intracluster medium. MNRAS, 378:293–300, June 2007. doi: 10.1111/j.1365-2966.2007. 11776.x.

S. W. Allen, D. A. Rapetti, R. W. Schmidt, H. Ebeling, R. G. Morris, and A. C. Fabian. Improved constraints on dark energy from Chandra X-ray observations of the largest relaxed galaxy clusters. MNRAS, 383:879–896, January 2008. doi: 10.1111/j.1365-2966. 2007.12610.x.

S. Andreon. The stellar mass fraction and baryon content of galaxy clusters and groups. MNRAS, 407:263–276, September 2010. doi: 10.1111/j.1365-2966.2010.16856.x.

R. A. Battye and J. Weller. Constraining cosmological parameters using Sunyaev-Zel'dovich cluster surveys. Phys. Rev. D, 68(8):083506, October 2003. doi: 10.1103/ PhysRevD.68.083506.

M. W. Bautz, E. D. Miller, J. S. Sanders, K. A. Arnaud, R. F. Mushotzky, F. S. Porter, K. Hayashida, J. P. Henry, J. P. Hughes, M. Kawaharada, K. Makashima, M. Sato, and T. Tamura. Suzaku Observations of Abell 1795: Cluster Emission to r_{200}. PASJ, 61: 1117–, October 2009.

M. R. Becker and A. V. Kravtsov. On the Accuracy of Weak-lensing Cluster Mass Reconstructions. ApJ, 740:25, October 2011. doi: 10.1088/0004-637X/740/1/25.

B. A. Benson, T. de Haan, J. P. Dudley, C. L. Reichardt, K. A. Aird, K. Andersson, R. Armstrong, M. L. N. Ashby, M. Bautz, M. Bayliss, G. Bazin, L. E. Bleem, M. Brodwin, J. E. Carlstrom, C. L. Chang, H. M. Cho, A. Clocchiatti, T. M. Crawford, A. T. Crites, S. Desai, M. A. Dobbs, R. J. Foley, W. R. Forman, E. M. George, M. D. Gladders, A. H. Gonzalez, N. W. Halverson, N. Harrington, F. W. High, G. P. Holder, W. L. Holzapfel, S. Hoover, J. D. Hrubes, C. Jones, M. Joy, R. Keisler, L. Knox, A. T. Lee,

E. M. Leitch, J. Liu, M. Lueker, D. Luong-Van, A. Mantz, D. P. Marrone, M. McDonald, J. J. McMahon, J. Mehl, S. S. Meyer, L. Mocanu, J. J. Mohr, T. E. Montroy, S. S. Murray, T. Natoli, S. Padin, T. Plagge, C. Pryke, A. Rest, J. Ruel, J. E. Ruhl, B. R. Saliwanchik, A. Saro, J. T. Sayre, K. K. Schaffer, L. Shaw, E. Shirokoff, J. Song, H. G. Spieler, B. Stalder, Z. Staniszewski, A. A. Stark, K. Story, C. W. Stubbs, R. Suhada, A. van Engelen, K. Vanderlinde, J. D. Vieira, A. Vikhlinin, R. Williamson, O. Zahn, and A. Zenteno. Cosmological Constraints from Sunyaev-Zel'dovich-selected Clusters with X-Ray Observations in the First 178deg^2 of the South Pole Telescope Survey. ApJ, 763: 147, February 2013. doi: 10.1088/0004-637X/763/2/147.

E. Bertin and S. Arnouts. SExtractor: Software for source extraction. A&AS, 117:393–404, June 1996.

S. Bhattacharya, S. Habib, K. Heitmann, and A. Vikhlinin. Dark Matter Halo Profiles of Massive Clusters: Theory versus Observations. ApJ, 766:32, March 2013. doi: 10.1088/0004-637X/766/1/32.

M. Bonamente, D. Landry, B. Maughan, P. Giles, M. Joy, and J. Nevalainen. Chandra X-ray observations of Abell 1835 to the virial radius. MNRAS, 428:2812–2823, February 2013. doi: 10.1093/mnras/sts202.

A. Cavaliere and R. Fusco-Femiano. The Distribution of Hot Gas in Clusters of Galaxies. A&A, 70:677, November 1978.

X. Dai, J. N. Bregman, C. S. Kochanek, and E. Rasia. On the Baryon Fractions in Clusters and Groups of Galaxies. ApJ, 719:119–125, August 2010. doi: 10.1088/0004-637X/719/1/119.

S. F. Daniel, E. V. Linder, T. L. Smith, R. R. Caldwell, A. Cooray, A. Leauthaud, and L. Lombriser. Testing general relativity with current cosmological data. Phys. Rev. D, 81(12):123508, June 2010. doi: 10.1103/PhysRevD.81.123508.

J. Einasto. On the Construction of a Composite Model for the Galaxy and on the Determination of the System of Galactic Parameters. *Trudy Astrofizicheskogo Instituta Alma-Ata*, 5:87–100, 1965.

D. J. Eisenstein, I. Zehavi, D. W. Hogg, R. Scoccimarro, M. R. Blanton, R. C. Nichol, R. Scranton, H.-J. Seo, M. Tegmark, Z. Zheng, S. F. Anderson, J. Annis, N. Bahcall, J. Brinkmann, S. Burles, F. J. Castander, A. Connolly, I. Csabai, M. Doi, M. Fukugita, J. A. Frieman, K. Glazebrook, J. E. Gunn, J. S. Hendry, G. Hennessy, Z. Ivezić, S. Kent,

G. R. Knapp, H. Lin, Y.-S. Loh, R. H. Lupton, B. Margon, T. A. McKay, A. Meiksin, J. A. Munn, A. Pope, M. W. Richmond, D. Schlegel, D. P. Schneider, K. Shimasaku, C. Stoughton, M. A. Strauss, M. SubbaRao, A. S. Szalay, I. Szapudi, D. L. Tucker, B. Yanny, and D. G. York. Detection of the Baryon Acoustic Peak in the Large-Scale Correlation Function of SDSS Luminous Red Galaxies. ApJ, 633:560–574, November 2005. doi: 10.1086/466512.

V. R. Eke, S. Cole, and C. S. Frenk. Cluster evolution as a diagnostic for Omega. MNRAS, 282:263–280, September 1996.

S. Ettori. Are we missing baryons in galaxy clusters? MNRAS, 344:L13–L16, September 2003. doi: 10.1046/j.1365-8711.2003.06810.x.

S. Ettori, S. Borgani, L. Moscardini, G. Murante, P. Tozzi, A. Diaferio, K. Dolag, V. Springel, G. Tormen, and L. Tornatore. Evolution at $z_¿= 0.5$ of the X-ray properties of simulated galaxy clusters: comparison with observational constraints. MNRAS, 354:111–122, October 2004. doi: 10.1111/j.1365-2966.2004.08170.x.

A. C. Fabian, P. E. J. Nulsen, and C. R. Canizares. Cooling flows in clusters of galaxies. A&A Rev., 2:191–226, April 1991. doi: 10.1007/BF00872767.

A. C. Fabian, C. S. Crawford, A. C. Edge, and R. F. Mushotzky. Cooling flows and the X-ray luminosity-temperature relation for clusters. MNRAS, 267:779, April 1994.

M. R. George, A. C. Fabian, J. S. Sanders, A. J. Young, and H. R. Russell. X-ray observations of the galaxy cluster PKS0745-191: to the virial radius, and beyond. MNRAS, 395:657–666, May 2009. doi: 10.1111/j.1365-2966.2009.14547.x.

M. Girardi, G. Giuricin, F. Mardirossian, M. Mezzetti, and W. Boschin. Optical Mass Estimates of Galaxy Clusters. ApJ, 505:74–95, September 1998. doi: 10.1086/306157.

M. D. Gladders and H. K. C. Yee. A New Method For Galaxy Cluster Detection. I. The Algorithm. AJ, 120:2148–2162, October 2000. doi: 10.1086/301557.

G. Golse and J.-P. Kneib. Pseudo elliptical lensing mass model: Application to the NFW mass distribution. A&A, 390:821–827, August 2002. doi: 10.1051/0004-6361:20020639.

A. H. Gonzalez, A. I. Zabludoff, and D. Zaritsky. Intracluster Light in Nearby Galaxy Clusters: Relationship to the Halos of Brightest Cluster Galaxies. ApJ, 618:195–213, January 2005. doi: 10.1086/425896.

A. H. Gonzalez, D. Zaritsky, and A. I. Zabludoff. A Census of Baryons in Galaxy Clusters and Groups. ApJ, 666:147–155, September 2007. doi: 10.1086/519729.

S. D. J. Gwyn. MegaPipe: The MegaCam Image Stacking Pipeline at the Canadian Astronomical Data Centre. PASP, 120:212–223, February 2008. doi: 10.1086/526794.

S. D. J. Gwyn. The Canada-France-Hawaii Telescope Legacy Survey: Stacked Images and Catalogs. AJ, 143:38, February 2012. doi: 10.1088/0004-6256/143/2/38.

Z. Haiman, J. J. Mohr, and G. P. Holder. Constraints on Cosmological Parameters from Future Galaxy Cluster Surveys. ApJ, 553:545–561, June 2001. doi: 10.1086/320939.

J. Hao, T. A. McKay, B. P. Koester, E. S. Rykoff, E. Rozo, J. Annis, R. H. Wechsler, A. Evrard, S. R. Siegel, M. Becker, M. Busha, D. Gerdes, D. E. Johnston, and E. Sheldon. A GMBCG Galaxy Cluster Catalog of 55,424 Rich Clusters from SDSS DR7. ApJS, 191: 254–274, December 2010. doi: 10.1088/0067-0049/191/2/254.

L. Hernquist. An analytical model for spherical galaxies and bulges. ApJ, 356:359–364, June 1990. doi: 10.1086/168845.

H. Hoekstra, J. Hartlap, S. Hilbert, and E. van Uitert. Effects of distant large-scale structure on the precision of weak lensing mass measurements. MNRAS, 412:2095–2103, April 2011. doi: 10.1111/j.1365-2966.2010.18053.x.

G. Holder, Z. Haiman, and J. J. Mohr. Constraints on Ω_m, Ω, and σ_8 from Galaxy Cluster Redshift Distributions. ApJ, 560:L111–L114, October 2001. doi: 10.1086/324309.

A. Hoshino, J. P. Henry, K. Sato, H. Akamatsu, W. Yokota, S. Sasaki, Y. Ishisaki, T. Ohashi, M. Bautz, Y. Fukazawa, N. Kawano, A. Furuzawa, K. Hayashida, N. Tawa, J. P. Hughes, M. Kokubun, and T. Tamura. X-Ray Temperature and Mass Measurements to the Virial Radius of Abell 1413 with Suzaku. PASJ, 62:371–389, April 2010.

K. Ichikawa, K. Matsushita, N. Okabe, K. Sato, Y.-Y. Zhang, A. Finoguenov, Y. Fujita, Y. Fukazawa, M. Kawaharada, K. Nakazawa, T. Ohashi, N. Ota, M. Takizawa, T. Tamura, and K. Umetsu. Suzaku Observations of the Outskirts of A1835: Deviation from Hydrostatic Equilibrium. ApJ, 766:90, April 2013. doi: 10.1088/0004-637X/766/2/90.

W. Jaffe. A simple model for the distribution of light in spherical galaxies. MNRAS, 202: 995–999, March 1983.

D. H. Jones, M. A. Read, W. Saunders, M. Colless, T. Jarrett, Q. A. Parker, A. P. Fairall, T. Mauch, E. M. Sadler, F. G. Watson, D. Burton, L. A. Campbell, P. Cass, S. M. Croom, J. Dawe, K. Fiegert, L. Frankcombe, M. Hartley, J. Huchra, D. James, E. Kirby, O. Lahav, J. Lucey, G. A. Mamon, L. Moore, B. A. Peterson, S. Prior, D. Proust, K. Russell, V. Safouris, K.-I. Wakamatsu, E. Westra, and M. Williams. The 6dF Galaxy Survey: final redshift release (DR3) and southern large-scale structures. MNRAS, 399: 683–698, October 2009. doi: 10.1111/j.1365-2966.2009.15338.x.

E. Komatsu, K. M. Smith, J. Dunkley, C. L. Bennett, B. Gold, G. Hinshaw, N. Jarosik, D. Larson, M. R. Nolta, L. Page, D. N. Spergel, M. Halpern, R. S. Hill, A. Kogut, M. Limon, S. S. Meyer, N. Odegard, G. S. Tucker, J. L. Weiland, E. Wollack, and E. L. Wright. Seven-year Wilkinson Microwave Anisotropy Probe (WMAP) Observations: Cosmological Interpretation. ApJS, 192:18, February 2011. doi: 10.1088/0067-0049/ 192/2/18.

A. V. Kravtsov, D. Nagai, and A. A. Vikhlinin. Effects of Cooling and Star Formation on the Baryon Fractions in Clusters. ApJ, 625:588–598, June 2005. doi: 10.1086/429796.

A. V. Kravtsov, A. Vikhlinin, and D. Nagai. A New Robust Low-Scatter X-Ray Mass Indicator for Clusters of Galaxies. ApJ, 650:128–136, October 2006. doi: 10.1086/506319.

M. Lima and W. Hu. Self-calibration of cluster dark energy studies: Observable-mass distribution. Phys. Rev. D, 72(4):043006, August 2005. doi: 10.1103/PhysRevD.72. 043006.

Y.-T. Lin and J. J. Mohr. K-band Properties of Galaxy Clusters and Groups: Brightest Cluster Galaxies and Intracluster Light. ApJ, 617:879–895, December 2004. doi: 10. 1086/425412.

E. L. Łokas and G. A. Mamon. Properties of spherical galaxies and clusters with an NFW density profile. MNRAS, 321:155–166, February 2001. doi: 10.1046/j.1365-8711.2001. 04007.x.

A. Mantz, S. W. Allen, and D. Rapetti. The observed growth of massive galaxy clusters - IV. Robust constraints on neutrino properties. MNRAS, 406:1805–1814, August 2010a. doi: 10.1111/j.1365-2966.2010.16794.x.

A. Mantz, S. W. Allen, D. Rapetti, and H. Ebeling. The observed growth of massive galaxy clusters - I. Statistical methods and cosmological constraints. MNRAS, 406:1759–1772, August 2010b. doi: 10.1111/j.1365-2966.2010.16992.x.

I. G. McCarthy, M. L. Balogh, A. Babul, G. B. Poole, and D. J. Horner. Models of the Intracluster Medium with Heating and Cooling: Explaining the Global and Structural X-Ray Properties of Clusters. ApJ, 613:811–830, October 2004. doi: 10.1086/423267.

S. S. McGaugh, J. M. Schombert, W. J. G. de Blok, and M. J. Zagursky. The Baryon Content of Cosmic Structures. ApJ, 708:L14–L17, January 2010. doi: 10.1088/2041-8205/708/1/L14.

B. R. McNamara and P. E. J. Nulsen. Mechanical feedback from active galactic nuclei in galaxies, groups and clusters. New Journal of Physics, 14(5):055023, May 2012. doi: 10.1088/1367-2630/14/5/055023.

H. Mo, F. C. van den Bosch, and S. White. Galaxy Formation and Evolution. May 2010.

D. Nagai and A. V. Kravtsov. The Radial Distribution of Galaxies in Λ Cold Dark Matter Clusters. ApJ, 618:557–568, January 2005. doi: 10.1086/426016.

D. Nagai and E. T. Lau. Gas Clumping in the Outskirts of ΛCDM Clusters. ApJ, 731:L10, April 2011. doi: 10.1088/2041-8205/731/1/L10.

J. F. Navarro, C. S. Frenk, and S. D. M. White. A Universal Density Profile from Hierarchical Clustering. ApJ, 490:493, December 1997. doi: 10.1086/304888.

I. J. Parrish, E. Quataert, and P. Sharma. Anisotropic Thermal Conduction and the Cooling Flow Problem in Galaxy Clusters. ApJ, 703:96–108, September 2009. doi: 10.1088/0004-637X/703/1/96.

S. Perlmutter, G. Aldering, M. della Valle, S. Deustua, R. S. Ellis, S. Fabbro, A. Fruchter, G. Goldhaber, D. E. Groom, I. M. Hook, A. G. Kim, M. Y. Kim, R. A. Knop, C. Lidman, R. G. McMahon, P. Nugent, R. Pain, N. Panagia, C. R. Pennypacker, P. Ruiz-Lapuente, B. Schaefer, and N. Walton. Discovery of a supernova explosion at half the age of the universe. Nature, 391:51, January 1998. doi: 10.1038/34124.

S. Perlmutter, G. Aldering, G. Goldhaber, R. A. Knop, P. Nugent, P. G. Castro, S. Deustua, S. Fabbro, A. Goobar, D. E. Groom, I. M. Hook, A. G. Kim, M. Y. Kim, J. C. Lee, N. J. Nunes, R. Pain, C. R. Pennypacker, R. Quimby, C. Lidman, R. S. Ellis, M. Irwin, R. G. McMahon, P. Ruiz-Lapuente, N. Walton, B. Schaefer, B. J. Boyle, A. V. Filippenko, T. Matheson, A. S. Fruchter, N. Panagia, H. J. M. Newberg, W. J. Couch, and Supernova Cosmology Project. Measurements of Omega and Lambda from 42 High-Redshift Supernovae. ApJ, 517:565–586, June 1999. doi: 10.1086/307221.

D. Rapetti, S. W. Allen, A. Mantz, and H. Ebeling. The observed growth of massive galaxy clusters - III. Testing general relativity on cosmological scales. MNRAS, 406:1796–1804, August 2010. doi: 10.1111/j.1365-2966.2010.16799.x.

T. H. Reiprich and H. Böhringer. The Mass Function of an X-Ray Flux-limited Sample of Galaxy Clusters. ApJ, 567:716–740, March 2002. doi: 10.1086/338753.

J. Richard, G. P. Smith, J.-P. Kneib, R. S. Ellis, A. J. R. Sanderson, L. Pei, T. A. Targett, D. J. Sand, A. M. Swinbank, H. Dannerbauer, P. Mazzotta, M. Limousin, E. Egami, E. Jullo, V. Hamilton-Morris, and S. M. Moran. LoCuSS: first results from strong-lensing analysis of 20 massive galaxy clusters at z = 0.2. MNRAS, 404:325–349, May 2010. doi: 10.1111/j.1365-2966.2009.16274.x.

A. G. Riess, A. V. Filippenko, P. Challis, A. Clocchiatti, A. Diercks, P. M. Garnavich, R. L. Gilliland, C. J. Hogan, S. Jha, R. P. Kirshner, B. Leibundgut, M. M. Phillips, D. Reiss, B. P. Schmidt, R. A. Schommer, R. C. Smith, J. Spyromilio, C. Stubbs, N. B. Suntzeff, and J. Tonry. Observational Evidence from Supernovae for an Accelerating Universe and a Cosmological Constant. AJ, 116:1009–1038, September 1998. doi: 10.1086/300499.

M. Roncarelli, S. Ettori, K. Dolag, L. Moscardini, S. Borgani, and G. Murante. Simulated X-ray galaxy clusters at the virial radius: Slopes of the gas density, temperature and surface brightness profiles. MNRAS, 373:1339–1350, December 2006. doi: 10.1111/j. 1365-2966.2006.11143.x.

E. Rozo, R. H. Wechsler, E. S. Rykoff, J. T. Annis, M. R. Becker, A. E. Evrard, J. A. Frieman, S. M. Hansen, J. Hao, D. E. Johnston, B. P. Koester, T. A. McKay, E. S. Sheldon, and D. H. Weinberg. Cosmological Constraints from the Sloan Digital Sky Survey maxBCG Cluster Catalog. ApJ, 708:645–660, January 2010. doi: 10.1088/ 0004-637X/708/1/645.

T. Sato, T. Sasaki, K. Matsushita, E. Sakuma, K. Sato, Y. Fujita, N. Okabe, Y. Fukazawa, K. Ichikawa, M. Kawaharada, K. Nakazawa, T. Ohashi, N. Ota, M. Takizawa, and T. Tamura. Suzaku Observations of the Hydra A Cluster out to the Virial Radius. PASJ, 64:95, October 2012.

N. Sehgal, P. Bode, S. Das, C. Hernandez-Monteagudo, K. Huffenberger, Y.-T. Lin, J. P. Ostriker, and H. Trac. Simulations of the Microwave Sky. ApJ, 709:920–936, February 2010. doi: 10.1088/0004-637X/709/2/920.

H. Y. Shan, B. Qin, and H. S. Zhao. Mass discrepancy in galaxy clusters as a result of the offset between dark matter and baryon distributions. MNRAS, 408:1277–1282, October 2010. doi: 10.1111/j.1365-2966.2010.17209.x.

J. M. Shull, B. D. Smith, and C. W. Danforth. The Baryon Census in a Multiphase Intergalactic Medium: 30% of the Baryons May Still be Missing. ApJ, 759:23, November 2012. doi: 10.1088/0004-637X/759/1/23.

A. Simionescu, S. W. Allen, A. Mantz, N. Werner, Y. Takei, R. G. Morris, A. C. Fabian, J. S. Sanders, P. E. J. Nulsen, M. R. George, and G. B. Taylor. Baryons at the Edge of the X-ray-Brightest Galaxy Cluster. *Science*, 331:1576–, March 2011. doi: 10.1126/ science.1200331.

R. J. Smith, M. J. Hudson, J. E. Nelan, S. A. W. Moore, S. J. Quinney, G. A. Wegner, J. R. Lucey, R. L. Davies, J. J. Malecki, D. Schade, and N. B. Suntzeff. NOAO Fundamental Plane Survey. I. Survey Design, Redshifts, and Velocity Dispersion Data. AJ, 128:1558–1569, October 2004. doi: 10.1086/423915.

D. N. Spergel, L. Verde, H. V. Peiris, E. Komatsu, M. R. Nolta, C. L. Bennett, M. Halpern, G. Hinshaw, N. Jarosik, A. Kogut, M. Limon, S. S. Meyer, L. Page, G. S. Tucker, J. L. Weiland, E. Wollack, and E. L. Wright. First-Year Wilkinson Microwave Anisotropy Probe (WMAP) Observations: Determination of Cosmological Parameters. ApJS, 148: 175–194, September 2003. doi: 10.1086/377226.

D. N. Spergel, R. Bean, O. Doré, M. R. Nolta, C. L. Bennett, J. Dunkley, G. Hinshaw, N. Jarosik, E. Komatsu, L. Page, H. V. Peiris, L. Verde, M. Halpern, R. S. Hill, A. Kogut, M. Limon, S. S. Meyer, N. Odegard, G. S. Tucker, J. L. Weiland, E. Wollack, and E. L. Wright. Three-Year Wilkinson Microwave Anisotropy Probe (WMAP) Observations: Implications for Cosmology. ApJS, 170:377–408, June 2007. doi: 10.1086/513700.

R. A. Sunyaev and Y. B. Zeldovich. The Observations of Relic Radiation as a Test of the Nature of X-Ray Radiation from the Clusters of Galaxies. *Comments on Astrophysics and Space Physics*, 4:173, November 1972.

M. Tegmark, M. A. Strauss, M. R. Blanton, K. Abazajian, S. Dodelson, H. Sandvik, X. Wang, D. H. Weinberg, I. Zehavi, N. A. Bahcall, F. Hoyle, D. Schlegel, R. Scoccimarro, M. S. Vogeley, A. Berlind, T. Budavari, A. Connolly, D. J. Eisenstein, D. Finkbeiner, J. A. Frieman, J. E. Gunn, L. Hui, B. Jain, D. Johnston, S. Kent, H. Lin, R. Nakajima, R. C. Nichol, J. P. Ostriker, A. Pope, R. Scranton, U. Seljak, R. K. Sheth, A. Stebbins, A. S. Szalay, I. Szapudi, Y. Xu, J. Annis, J. Brinkmann, S. Burles, F. J. Castander,

I. Csabai, J. Loveday, M. Doi, M. Fukugita, B. Gillespie, G. Hennessy, D. W. Hogg, Ž. Ivezić, G. R. Knapp, D. Q. Lamb, B. C. Lee, R. H. Lupton, T. A. McKay, P. Kunszt, J. A. Munn, L. O'Connell, J. Peoples, J. R. Pier, M. Richmond, C. Rockosi, D. P. Schneider, C. Stoughton, D. L. Tucker, D. E. vanden Berk, B. Yanny, and D. G. York. Cosmological parameters from SDSS and WMAP. Phys. Rev. D, 69(10):103501, May 2004. doi: 10.1103/PhysRevD.69.103501.

S. Tremaine, D. O. Richstone, Y.-I. Byun, A. Dressler, S. M. Faber, C. Grillmair, J. Kormendy, and T. R. Lauer. A family of models for spherical stellar systems. AJ, 107: 634–644, February 1994. doi: 10.1086/116883.

O. Urban, N. Werner, A. Simionescu, S. W. Allen, and H. Böhringer. X-ray spectroscopy of the Virgo Cluster out to the virial radius. MNRAS, 414:2101–2111, July 2011. doi: 10.1111/j.1365-2966.2011.18526.x.

T. Valentinuzzi, B. M. Poggianti, G. Fasano, M. D'Onofrio, A. Moretti, M. Ramella, A. Biviano, J. Fritz, J. Varela, D. Bettoni, B. Vulcani, M. Moles, W. J. Couch, A. Dressler, P. Kjærgaard, A. Omizzolo, and A. Cava. The red-sequence of 72 WINGS local galaxy clusters. A&A, 536:A34, December 2011. doi: 10.1051/0004-6361/201117522.

K. Vanderlinde, T. M. Crawford, T. de Haan, J. P. Dudley, L. Shaw, P. A. R. Ade, K. A. Aird, B. A. Benson, L. E. Bleem, M. Brodwin, J. E. Carlstrom, C. L. Chang, A. T. Crites, S. Desai, M. A. Dobbs, R. J. Foley, E. M. George, M. D. Gladders, N. R. Hall, N. W. Halverson, F. W. High, G. P. Holder, W. L. Holzapfel, J. D. Hrubes, M. Joy, R. Keisler, L. Knox, A. T. Lee, E. M. Leitch, A. Loehr, M. Lueker, D. P. Marrone, J. J. McMahon, J. Mehl, S. S. Meyer, J. J. Mohr, T. E. Montroy, C.-C. Ngeow, S. Padin, T. Plagge, C. Pryke, C. L. Reichardt, A. Rest, J. Ruel, J. E. Ruhl, K. K. Schaffer, E. Shirokoff, J. Song, H. G. Spieler, B. Stalder, Z. Staniszewski, A. A. Stark, C. W. Stubbs, A. van Engelen, J. D. Vieira, R. Williamson, Y. Yang, O. Zahn, and A. Zenteno. Galaxy Clusters Selected with the Sunyaev-Zel'dovich Effect from 2008 South Pole Telescope Observations. ApJ, 722:1180–1196, October 2010. doi: 10.1088/0004-637X/722/2/1180.

J. Varela, M. D'Onofrio, C. Marmo, G. Fasano, D. Bettoni, A. Cava, W. J. Couch, A. Dressler, P. Kjærgaard, M. Moles, E. Pignatelli, B. M. Poggianti, and T. Valentinuzzi. WINGS: A WIde-field Nearby Galaxy-cluster Survey. II. Deep optical photometry of 77 nearby clusters. A&A, 497:667–676, April 2009. doi: 10.1051/0004-6361/200809876.

A. Vikhlinin, A. Kravtsov, W. Forman, C. Jones, M. Markevitch, S. S. Murray, and L. Van Speybroeck. Chandra Sample of Nearby Relaxed Galaxy Clusters: Mass, Gas Fraction, and Mass-Temperature Relation. ApJ, 640:691–709, April 2006. doi: 10.1086/500288.

A. Vikhlinin, R. A. Burenin, H. Ebeling, W. R. Forman, A. Hornstrup, C. Jones, A. V. Kravtsov, S. S. Murray, D. Nagai, H. Quintana, and A. Voevodkin. Chandra Cluster Cosmology Project. II. Samples and X-Ray Data Reduction. ApJ, 692:1033–1059, February 2009a. doi: 10.1088/0004-637X/692/2/1033.

A. Vikhlinin, A. V. Kravtsov, R. A. Burenin, H. Ebeling, W. R. Forman, A. Hornstrup, C. Jones, S. S. Murray, D. Nagai, H. Quintana, and A. Voevodkin. Chandra Cluster Cosmology Project III: Cosmological Parameter Constraints. ApJ, 692:1060–1074, February 2009b. doi: 10.1088/0004-637X/692/2/1060.

G. M. Voit. Tracing cosmic evolution with clusters of galaxies. *Reviews of Modern Physics*, 77:207–258, April 2005. doi: 10.1103/RevModPhys.77.207.

G. M. Voit, S. T. Kay, and G. L. Bryan. The baseline intracluster entropy profile from gravitational structure formation. MNRAS, 364:909–916, December 2005. doi: 10.1111/j.1365-2966.2005.09621.x.

S. A. Walker, A. C. Fabian, J. S. Sanders, and M. R. George. Further X-ray observations of the galaxy cluster PKS 0745-191 to the virial radius and beyond. MNRAS, 424: 1826–1840, August 2012a. doi: 10.1111/j.1365-2966.2012.21282.x.

S. A. Walker, A. C. Fabian, J. S. Sanders, M. R. George, and Y. Tawara. X-ray observations of the galaxy cluster Abell 2029 to the virial radius. MNRAS, 422:3503–3515, June 2012b. doi: 10.1111/j.1365-2966.2012.20860.x.

L. Wang and P. J. Steinhardt. Cluster Abundance Constraints for Cosmological Models with a Time-varying, Spatially Inhomogeneous Energy Component with Negative Pressure. ApJ, 508:483–490, December 1998. doi: 10.1086/306436.

S. Wang, J. Khoury, Z. Haiman, and M. May. Constraining the evolution of dark energy with a combination of galaxy cluster observables. Phys. Rev. D, 70(12):123008, December 2004. doi: 10.1103/PhysRevD.70.123008.

S. D. M. White, G. Efstathiou, and C. S. Frenk. The amplitude of mass fluctuations in the universe. MNRAS, 262:1023–1028, June 1993.

X.-P. Wu and L.-Z. Fang. A Statistical Comparison of Cluster Mass Estimates from Optical/X-Ray Observations and Gravitational Lensing. ApJ, 483:62, July 1997. doi: 10.1086/304235.

O. E. Young, P. A. Thomas, C. J. Short, and Pearce F. Baryon fractions in clusters of galaxies: evidence against a preheating model for entropy generation, 2010.

Y.-Y. Zhang, N. Okabe, A. Finoguenov, G. P. Smith, R. Piffaretti, R. Valdarnini, A. Babul, A. E. Evrard, P. Mazzotta, A. J. R. Sanderson, and D. P. Marrone. LoCuSS: A Comparison of Cluster Mass Measurements from XMM-Newton and Subaru − Testing Deviation from Hydrostatic Equilibrium and Non-thermal Pressure Support. ApJ, 711:1033–1043, March 2010. doi: 10.1088/0004-637X/711/2/1033.

Y.-Y. Zhang, H. Andernach, C. A. Caretta, T. H. Reiprich, H. Böhringer, E. Puchwein, D. Sijacki, and M. Girardi. HIFLUGCS: Galaxy cluster scaling relations between X-ray luminosity, gas mass, cluster radius, and velocity dispersion. A&A, 526:A105, February 2011. doi: 10.1051/0004-6361/201015830.